

UC San Diego

UC San Diego Electronic Theses and Dissertations

Title

Mesoscale to large-scale variability in the California Current System from high-resolution observations

Permalink

<https://escholarship.org/uc/item/2rz092nr>

Author

Ren, Alice Sonya

Publication Date

2022

Peer reviewed|Thesis/dissertation

UNIVERSITY OF CALIFORNIA SAN DIEGO

Mesoscale to large-scale variability in the California Current System from high-resolution observations

A dissertation submitted in partial satisfaction
of the requirements for the Doctor of Philosophy

in

Oceanography

by

Alice Sonya Ren

Committee in charge:

Professor Daniel L. Rudnick, Chair
Professor Bruce Cornuelle
Professor Sarah Gille
Professor Todd Martz
Professor Sutanu Sarkar

2022

Copyright

Alice Sonya Ren, 2022

All Rights Reserved

The dissertation of Alice Sonya Ren is approved, and it is acceptable in quality and form for publication on microfilm and electronically.

University of California San Diego

2022

DEDICATION

I would like to dedicate this work to my family. My grandparents Liumei Chu and Xiangbin Ren. My mother Wenjia Qin and my dad Biao Ren. Finally, my brother Michael.

EPIGRAPH

“Souvenez-vous que dans les champs de l’observation le hasard ne favorise que les esprits préparés.”

“Remember that in the fields of observation luck favors the prepared.”

Louis Pasteur, 1854

TABLE OF CONTENTS

Dissertation Approval Page	iii
Dedication.....	iv
Epigraph.....	v
Table of Contents.....	vi
List of Figures.....	vii
Acknowledgments	ix
Vita	xi
Abstract of the Dissertation	xii
Introduction.....	1
Chapter 1 Temperature and salinity extremes from 2014-2019 in the California Current System and its source waters	9
Chapter 2 Across-shore propagation of subthermocline eddies in the California Current System	29
Chapter 3 The annual cycle of dissolved oxygen from high-resolution glider observations in the California Current System	56
Chapter 4 Drift characteristics of Sea-Bird dissolved oxygen optode sensors	100
Conclusion	123

LIST OF FIGURES

Figure 1.1 Historical offshore temperature and salinity observations in the California Current	12
Figure 1.2 Hovmoller diagrams of salinity anomaly from CUGN gliders on Lines 66.7, 80.0, and 90.0 ..	13
Figure 1.3 The profile of mean practical salinity and depth and the gradient of mean practical salinity over depth in the offshore region between stations 70-100 on Lines 66.7, 80.0, and 90.0	14
Figure 1.4 Hovmoller diagrams of temperature anomaly from CUGN gliders on Lines 66.7, 80.0, and 90.0	15
Figure 1.5 Plots of salinity anomaly at 10 db from the R-G Argo climatology	17
Figure 1.6 Salt flux in the North Pacific and CCS	18
Figure 1.7 T-S diagrams of 2018 compared to the mean	20
Figure 2.1 The domain of CUGN gliders and the coverage of gliders on Lines 66.7, 80.0, and 90.0	33
Figure 2.2 Two glider transects in March and April 2017 that crossed a STE.....	39
Figure 2.3 Hovmoller diagrams of CUGN climatology salinity anomaly on σ_{θ} 26.5 kg m ⁻³	40
Figure 2.4 Hovmoller diagrams from the CUGN climatology of geostrophic velocity anomaly, salinity anomaly, and potential temperature anomaly	41
Figure 2.5 Spatial and temporal autocorrelation maps of salinity anomaly	42
Figure 2.6 The mean profiles of potential density and buoyancy frequency across Lines 66.7, 80.0, and 90.0	43
Figure 2.7 Joint PDFs of mean salinity and layer thickness for the potential density layer defined between σ_{θ} 25.7-26.8 kg m ⁻³	44
Figure 2.8 Joint PDFs of mean dissolved oxygen and layer thickness and mean dissolved oxygen and salinity for the potential density layer defined between σ_{θ} 25.7-26.8 kg m ⁻³	45
Figure 2.9 Joint PDFs of sea level anomaly compared to characteristics of the potential density layer defined between σ_{θ} 25.7-26.8 kg m ⁻³	46
Figure 2.10 Hovmoller diagrams of sea level anomaly on Lines 66.7, 80.0, and 90.0	47
Figure 3.1 Coastal domain and coverage of CUGN 2017-2020.....	58
Figure 3.2 Mean section plots of dissolved oxygen	64
Figure 3.3 Seasonal plots of dissolved oxygen on Line 66.7	65
Figure 3.4 Seasonal plots of dissolved oxygen on Line 80.0	66
Figure 3.5 Seasonal plots of dissolved oxygen on Line 90.0	67

Figure 3.6 The annual cycle at 30 m depth on Line 66.7	69
Figure 3.7 The annual cycle at 30 m depth on Line 80.0	70
Figure 3.8 The annual cycle at 30 m depth on Line 90.0	71
Figure 3.9 The annual cycle of properties on potential density 25.4 kg m^{-3} on Line 66.7	72
Figure 3.10 The annual cycle of properties on potential density 25.4 kg m^{-3} on Line 80.0	73
Figure 3.11 The annual cycle of properties on potential density 24.8 kg m^{-3} on Line 90.0	74
Figure 3.12 Anomalies of dissolved oxygen and depth on potential density	76
Figure 3.13 Annual cycle and anomalies of chl- <i>a</i>	78
Figure 3.14 The annual cycle of surface oxygen saturation	79
Figure 3.15 The evolution of the summer subsurface dissolved oxygen maximum	80
Figure 3.16 The evolution of seasonal coastal upwelling.....	81
Figure 3.17 Modeled evolution of temperature and dissolved oxygen	83
Figure 3.18 Summer dissolved oxygen increases within the subsurface oxygen maximum.....	84
Figure 3.19 Annual cycle of properties in isopycnal coordinates from 0-50 km on Line 66.7	86
Figure 3.20 Annual cycle of properties in isopycnal coordinates from 0-50 km on Line 80.0	88
Figure 3.21 Annual cycle of properties in isopycnal coordinates from 150-200 km on Line 90.0	90
Figure 3.22 Dissolved oxygen annual cycle at 10 m.....	94
Figure 3.23 Dissolved oxygen annual cycle at 10 m from World Ocean Atlas 2018	95
Figure 4.1 SBE63 gain over time using the in-water full saturation method	110
Figure 4.2 SBE63 gain over time using the in-air full saturation method.....	111
Figure 4.3 Rates of change of the gain coefficient during storage and deployment	112
Figure 4.4 Measured dissolved oxygen concentration in the zero-oxygen environment	114
Figure 4.5 SBE63 gain over time from comparison with hydrographic bottle samples.....	115
Figure 4.6 Modeled gain evolution with time	116

ACKNOWLEDGEMENTS

I would like to acknowledge my advisor Dan for his support over the past 5 years. Our chats, weekly or semiweekly, during a global coronavirus pandemic provided me a sense of stability and normalcy. I am lucky to have been able to learn from Dan, and I always felt that Dan was invested in my development and success. Second, I would like to acknowledge my physical oceanography cohort, entering in fall 2017, Emma Beer, Robert Sanchez, Channing Prend, Noel Brizuela, Lauren Kim, and Annie Adelson. Each of you is brilliant, smarter than me in one way or another. I was lucky enough to learn with you in the classroom and to be your friend. Third, I thank the instrument development group. As a PhD student, I am a temporary member of this group of engineers and scientists who build, maintain, fix, deploy, recover, and design oceanographic instruments. Thank you to Evan Goodwin, Jeff Sherman, Alistair Twombly, and Derek Vana, and Gui Castelao.

I would like to thank my committee members for helping me throughout my time at Scripps: Bruce Cornuelle, Sarah Gille, Sutanu Sarkar, and Todd Martz. I appreciate your feedback and support during my PhD.

I would like to thank all the climate and physical oceanography faculty at Scripps. I took many classes while I was here and my list of professors includes Sarah Giddings, Sarah Gille, Sarah Purkey, Stefan Lewllyn-Smith, Dan Rudnick, Falk Fedderson, Jennifer MacKinnon, Paola Cessi, Bill Young, Fiamma Straneo, Matthew Alford, Sutanu Sarkar, Laurence Armi, Myrl Hendershott, and Ian Eisenman. Thank you to Dan and Mark Merrifield for giving me the experience of being a teaching assistant.

I would like to thank the climate, atmospheric sciences, and physical oceanography (CASPO) department for letting me in and giving me the opportunity to study here. I have tried to take advantage of the opportunity, and I have really enjoyed it. I would like to thank Bia Villas Boas and Gui Castelao for being my hosts at Open House. I would like to thank my peer mentor Kristin Zeiden and my officemate Devon Northcott. There are also many other students who have made my experience at Scripps better, and I cannot name you all but thank you. There are so many people in San Diego who

have also made my time here so much better and thank you as well. Hopefully I will see you all at a party at Surfside.

I would like to acknowledge generous funding from the Department of Defense National Graduate Science and Engineering Fellowship (2019-2022) and the Scripps Institution of Oceanography department in the form of first-year support, grants, and a teaching assistantship.

Chapter 1, in full, is a reprint of the material as it appears in: Ren, A.S. and Rudnick, D.L. (2021) Temperature and salinity extremes from 2014-2019 in the California Current System and its source waters. *Communications Earth & Environment*, 2(62). The dissertation author was the primary investigator and author of this paper.

Chapter 2, in full, is a reprint of the material as it appears in: Ren, A.S. and Rudnick, D.L. (2022) Across-shore propagation of subthermocline eddies in the California Current System. *Journal of Physical Oceanography*, 52(1) 39-51. The dissertation author was the primary investigator and author of this paper.

Chapter 3, in part is currently being prepared for submission for publication of the material. Ren, A.S. and Rudnick, D.L. (2022). The dissertation author was the primary investigator and author of this paper.

Chapter 4, in part is currently being prepared for submission for publication of the material. Ren, A.S. and Rudnick, D.L. (2022). The dissertation author was the primary investigator and author of this paper.

VITA

- 2010 Bachelor of Science, Duke University
- 2016 Master of Science, University of Maine, Orono
- 2022 Doctor of Philosophy, University of California San Diego

PUBLICATIONS

Chavez, F. P., Pennington, J. T., Michisaki, R. P., Blum, M., Chavez, G. M., Friederich, J., Jones, B., Herlien, R., Kieft, B., Hobson, B., Ren, A. S., Ryan, J., Sevadjian, J. C., Wahl, C., Walz, K. R., Yamahara, K., Friederich, G.E., Messié, M. (2017) Climate Variability and Change: Response of a Coastal Ocean Ecosystem. *Oceanography*, 30(4), 128-145. <https://doi.org/10.5670/oceanog.2017.429>

Ren, A. S., Chai, F., Xue, H., Anderson, D. M., & Chavez, F. P. (2018). A Sixteen-year Decline in Dissolved Oxygen in the Central California Current. *Scientific reports*, 8(1), 7290. <https://doi.org/10.1038/s41598-018-25341-8>

Ren, A.S., Rudnick, D.L. (2021). Temperature and salinity extremes from 2014-2019 in the California Current System and its source waters. *Communications Earth & Environment*, 2(62). <https://doi.org/10.1038/s43247-021-00131-9>

Ren, A.S., Rudnick, D.L. (2022) Across-shore propagation of subthermocline eddies in the California Current System. *Journal of Physical Oceanography*, 52(1), 39-51. <https://doi.org/10.1175/JPO-D-21-0137.1>

ABSTRACT OF THE DISSERTATION

Mesoscale to large-scale variability in the California Current System from high-resolution observations

by

Alice Sonya Ren

Doctor of Philosophy in Oceanography

University of California San Diego, 2022

Professor Daniel L. Rudnick, Chair

Our understanding of the ocean historically has moved forward in parallel with our ability to make observations. In the thesis, high-resolution observations of the California Current System made by Spray underwater gliders are used to discuss extreme events, eddy across-shore transport, and the annual cycle of dissolved oxygen in the upper ocean. The time scales covered in the thesis include annual to interannual changes while the spatial scales are mesoscale and larger. The availability of high-resolution ocean glider data for over 13 years provides the backbone to conduct analyses over these time and spatial scales. The thesis starts by examining temperature and salinity extremes from 2014-2019 in the California Current System and its source waters. The 2014-2019 period was anomalously warm. In addition, a salinity anomaly from 2017-2019 in the California Current System was found to have formed in the North Pacific Subtropical Gyre in 2015 and subsequently advected into the source waters of the California Current. Next, the thesis examines the offshore propagation of subthermocline eddies from the

coast. Subthermocline eddies are observed to propagate at near the local first baroclinic Rossby wave speed. It is estimated that the subthermocline eddies are important to the salt budget in the California Current System and are difficult to track with surface observations alone. The thesis next discusses dissolved oxygen observations collected from 2017 to 2020. First, the thesis considers the procedure to correct for drift in the optical sensors used to make dissolved oxygen observations. A model is fit to changes in the gain correction coefficient over time and predicts the drift for 5 years after sensor calibration. Second, the thesis describes the annual cycle of dissolved oxygen in the upper 500 m of the central and southern California Current System. A subsurface dissolved oxygen maximum is described in the oligotrophic region on the offshore edge of the California Current System. During seasonal coastal upwelling, heave of isopycnals is the primary mechanism that deoxygenates the water column, while mixing and biological sources and sinks also cause changes. Evidence of ventilation is found along sloping isopycnals which oxygenates the ocean above 300 m. The collection of work in the thesis is relevant to extreme climate events and climate change in the oceans, including impacts to the biological environment. The thesis also touches on basic research questions related to geostrophic turbulence. The discoveries in the thesis are made possible by the high-resolution ocean data collected by autonomous Spray gliders used together in a network to create sustained observations of a regional ocean.

INTRODUCTION

In the thesis, a network of autonomous underwater vehicles called gliders is used to study the coastal ocean in the California Current System (CCS). The California Underwater Glider Network (CUGN) is used to study ocean extreme events, eddy across-shore propagation, and the annual cycle of dissolved oxygen in the upper ocean. In addition, a method to correct drift in oxygen optode sensors deployed on gliders is presented. In the following sections, the CCS and subsequently each thesis chapter will be introduced.

The use of observational technology is extremely important to the scientific discoveries presented. One factor in observing the ocean is the ability to make measurements over large spatial scales and for long times. Consider the spatial extent of the global ocean whose surface area is around 360 million square kilometers. A length-scale for processes in the large-scale, balanced ocean is the Rossby radius which ranges from on the order of 10 to 100 km. To cover the surface area of the ocean with one observational station at every 100 km by 100 km grid box, one would need over 36,000 stations. In each of these stations, an observational platform would need to make depth profiles to understand dynamics below the ocean surface. The challenge of observing the global ocean has been tackled with satellite observations of the ocean surface (Fu & Ferrari, 2008; Fu & Smith, 1996) and with a collection of global drifting scientific profiling floats, Argo, at 3-degree spatial resolution (Roemmich et al., 2009), where 1 degree latitude is approximately 100 km in length. A challenge remains however, to observe processes on scales less than 300 km through the water column persistently in the nearest 500 km to the coast, excluding nearshore dynamics like surf zone or shelf dynamics. The capability of underwater gliders fits the mission.

Underwater gliders are buoyancy-driven machines that can collect profile data while also navigating through the ocean on a set path (Rudnick, 2016). They can sample for the timescale of months and take profiles with horizontal resolution of a few kilometers. They provide information in the depth dimension and have been used to collect profiles to 1000 m. Glider propulsion is driven by a pump on board that pushes oil into and out of an external bladder, therefore changing the density or buoyancy of

the vehicle. Changes in buoyancy cause vertical movement in the water column and wings allow for horizontal motion. An advantage of gliders is that they can sample for a long time, mainly because they move slowly thus limiting the loss of energy to drag. The study area of the thesis is the California Current System (CCS). In the CCS, gliders are programmed to profile to 500 m depth, and the saw-tooth or “v” pattern the glider makes through the water sets the horizontal speed of the glider which is 0.25 m s^{-1} . The displacement of the glider includes the glider’s motion and the velocity of the current around the glider. As the CCS is an eastern boundary current system which has relatively weak mean currents, the gliders there do well to sample along transects. The gliders generate profiles to 500 m depth at 3-km spatial and 3-hour temporal resolution (Rudnick et al., 2017). With a network of gliders, transect lines can be monitored continuously. When used to repeatedly sample along one transect, gliders can be used to monitor for ocean changes in the section over time.

The resolution in time and space of observations from a network of gliders like CUGN allows a scientist to examine questions from the mesoscale, or the Rossby radius, to the large scale, such as an eastern boundary current like the California Current. In addition, CUGN has over a decade of continuous observation at 3-km and 3-hour resolution, which means that longest timescale approaches a decade, allowing for study of climate variability. The collection of investigations in the thesis uses a network of gliders to answer questions spanning the active mesoscale eddy field in the CCS to the annual cycle in the CCS to interannual variability in the CCS and greater Pacific Basin.

The California Current System (CCS)

There are four major current systems on the eastern boundaries of ocean basins, and the CCS is the current system on the eastern side of the north Pacific Ocean. All eastern boundary current systems have upwelling caused by equatorward winds which cause offshore Ekman transport and divergence at the coast (Robinson & Brink, 2006). An equatorward current is often accompanied by a poleward undercurrent that hugs the continental slope. In the CCS, the California Current flows equatorward as a surface intensified current generally offshore of 150 km from the coast while the California Undercurrent flows poleward and is the mean flow within 150 km of the coast (Rudnick et al., 2017). In the central

CCS, spring upwelling is caused by the strong equatorward winds in that season (García-Reyes & Largier, 2012). In the southern CCS or the Southern California Bight, weaker winds cause a modest seasonal cycle in the inshore regions while the strongest alongshore wind stress is found around 200 km from shore (Bograd et al., 2001).

Like in other eastern boundary current systems, the mean currents in the CCS are relatively weak with magnitude of the mean flows less than 0.20 m s^{-1} (Rudnick et al., 2017). In addition to the mean flow, the eddy field is significant in the CCS (Kurian et al., 2011). Studies of the sea surface from satellite data show a rich eddy field with vortices and coastal filaments (Strub & James, 2000). Studies of the subsurface CCS using floats, gliders, and ship hydrography have identified subsurface vortices called ceddies or subthermocline eddies (Garfield et al., 1999; Pelland et al., 2013). An open research question is how the eddy field contributes to the distribution of energy in the ocean and oceanographic tracers.

The CCS, like other eastern boundary current systems, is a biologically productive region (Chavez & Messié, 2009). Upwelling connects the surface ocean with nutrients found at depth that are necessary for phytoplankton growth (Ryther, 1969). Phytoplankton form the base of the food web and support an ecosystem including fish and large marine mammals. Spring upwelling has long been studied in the CCS and recognized for its importance to fisheries and ecosystem health (McClatchie, 2014). Another aspect of the CCS and eastern boundary currents is the presence of low dissolved oxygen concentrations at depth. Low oxygen concentrations are found when the amount of oxygen respiration that occurs is greater than the replenishment of oxygen from physical or biological mechanisms (Wyrki, 1962). At depth in the ocean, especially beneath productive regions, there is a high rate of respiration and a low rate of advection and mixing of high-dissolved oxygen water, which results in a steady state concentration of dissolved oxygen near or approaching zero. Low dissolved oxygen concentration impacts the species distribution of marine life (Breitburg et al., 2018).

In addition to the mean state, climate variability and change has long been a focus of work in the CCS, especially with historical and current marine fisheries operations as a concern. El Niño-Southern Oscillation historically has been the greatest driver of natural climate variability in the CCS (Bograd &

Lynn, 2001). The Pacific Decadal Oscillation (PDO) and North Pacific Gyre Oscillation (NPGO) are two additional widely used natural climate variability indices that come from patterns in the fields of sea surface temperature and pressure found within the last 50 to 100 years (Di Lorenzo et al., 2008; Mantua & Hare, 2002; Mantua et al., 1997). In 2014, a large marine heatwave affected the CCS that was not an El Nino event (Cavole et al., 2016), and there is evidence that the years since 2014 are abnormal. Changes could be related to global warming, and it is important to understand the mean state of the CCS and document changes into the future.

Temperature and Salinity Extremes from 2014-2019 in the California Current System and its Source Waters

The first chapter of the thesis looks at CUGN glider data and documents the extremes in ocean temperature and salinity from 2014-2019 as compared to 2007-2013, the first half of the glider record, and as compared to historical measurements from the California Cooperative Oceanic Fisheries Investigations (CalCOFI) hydrographic survey. Anomalies in both temperature and salinity are found in the 2014-2019 period. A marine heatwave that originated in the northeast Pacific Ocean (Bond et al., 2015) affected the CCS beginning in 2014 (Zaba & Rudnick, 2016). Another marine heatwave in the North Pacific was identified in 2019 (Amaya et al., 2020). The CUGN observations suggest that the CCS has been warmer since the 2014 heat wave and not returned to pre-2014 levels. The CUGN glider observations identified a high salinity anomaly that occurred from 2017-2019. Using Argo observations of the North Pacific, the high salinity anomaly was found to have advected eastward in the North Pacific Current before feeding into the source water of the California Current. The anomalous heat and salt from 2017-2019 are not related to El Nino and the NPGO, though an El Nino did occur in 2015-2016. The changing marine environment could have impacts to fisheries and the marine ecosystem.

Across-shore Propagation of Subthermocline Eddies in the California Current System

The second chapter of the thesis discusses subthermocline eddies in the CCS that are observed to propagate offshore and move tracers such as salinity in the across-shore direction. Hovmoller diagrams show salinity anomalies propagating offshore along the transect lines of CUGN. Particularly good

examples of propagation were found on one transect line off Monterey Bay, California. While subthermocline eddies are often observed by many different platforms, characteristics of subthermocline eddies such as patterns of generation and propagation are less understood. The chapter estimates an across-shore propagation speed of the subthermocline eddies and discusses the anomaly of tracers like salt found in anticyclonic subthermocline eddies. Further, a comparison of subsurface data from gliders and satellite sea surface height (SSH) suggests that subthermocline eddies are not easily detected by a surface expression. Subthermocline eddies are important for the distribution of ocean tracers, so understanding preferences in direction of propagation or speed of propagation will help in understanding how to account for their influence on the large scale.

The Annual Cycle of Dissolved Oxygen from High-resolution Glider Observations in the California Current System

The third chapter of the thesis looks at observations from gliders of dissolved oxygen taken for four years on three transect lines. Dissolved oxygen can describe the productivity of the oceans and is also a tracer for physical mechanisms. The use of gliders provides enough profiles to calculate the annual cycle in a coastal region with 5-km horizontal resolution and over the top 500 m of the ocean. Across-shore variation in the dissolved oxygen annual cycle is found related to the transition between a seasonal upwelling dominated regime and a more open-ocean, oligotrophic regime. Specific mechanisms governing the changing distributions of the annual cycle of dissolved oxygen are investigated. The annual cycle of dissolved oxygen in the CCS forms the base from which future research on climate variability and climate change can build.

Drift Characteristics of Sea-Bird Dissolved Oxygen Optode Sensors

The fourth chapter of the thesis describes a technical area of research that is important for the success of long-term dissolved oxygen measurements, especially by autonomous platforms with long missions. Dissolved oxygen optode sensors drift over time and have been found to read on the order of 10% lower than expected on the timescale of years since calibration. The exact cause of measured drift is unknown but could be related to the membrane on the sensor and environmental conditions. The optode

sensor works by measuring the fluorescence of a luminophore in the presence of dissolved oxygen. The difference in the fluorescence in the presence and absence of oxygen is used to calculate an oxygen concentration. The fourth chapter of the thesis evaluates drift as found on 14 Sea-Bird 63 optode sensors over 5 years as they perform 100-day long missions and spend months in storage on land. The objective is to provide measurements of drift over many sensors over many years and to identify a protocol that corrects the dissolved oxygen observations for drift due to the sensor. Given concern about deoxygenation of the oceans due to climate change, it is important to measure dissolved oxygen with accuracy.

Conclusions

The thesis uses high-resolution glider observations to better understand the CCS. The observations are used to study the annual cycle, interannual variability, and track changes in mesoscale phenomena from months to years. The spatial scales span the mesoscale to large-scale and include fundamental processes such as upwelling, mesoscale eddies, and the advection of ocean tracers. The thesis demonstrates the range of study that can be accomplished observationally with a network of gliders.

The first and second chapters of the thesis have been published. The third and fourth chapters are in preparation for submission.

References

- Amaya, D. J., Miller, A. J., Xie, S.-P., & Kosaka, Y. (2020). Physical drivers of the summer 2019 North Pacific marine heatwave. *Nature Communications*, *11*(1), 1903. <https://doi.org/10.1038/s41467-020-15820-w>
- Bograd, S. J., Chereskin, T. K., & Roemmich, D. (2001). Transport of mass, heat, salt, and nutrients in the southern California Current System: Annual cycle and interannual variability. *Journal of Geophysical Research: Oceans*, *106*(C5), 9255-9275. <https://doi.org/https://doi.org/10.1029/1999JC000165>
- Bograd, S. J., & Lynn, R. J. (2001). Physical-biological coupling in the California Current during the 1997–99 El Niño–La Niña Cycle. *Geophysical Research Letters*, *28*(2), 275-278. <https://doi.org/10.1029/2000gl012047>
- Bond, N. A., Cronin, M. F., Freeland, H., & Mantua, N. (2015). Causes and impacts of the 2014 warm anomaly in the NE Pacific. *Geophysical Research Letters*, *42*(9), 3414-3420. <https://doi.org/10.1002/2015gl063306>

- Breitburg, D., Levin, L. A., Oschlies, A., Grégoire, M., Chavez, F. P., Conley, D. J., Garçon, V., Gilbert, D., Gutiérrez, D., Isensee, K., Jacinto, G. S., Limburg, K. E., Montes, I., Naqvi, S. W. A., Pitcher, G. C., Rabalais, N. N., Roman, M. R., Rose, K. A., Seibel, B. A., Telszewski, M., Yasuhara, M., & Zhang, J. (2018). Declining oxygen in the global ocean and coastal waters. *Science*, *359*(6371), eaam7240. <https://doi.org/doi:10.1126/science.aam7240>
- Cavole, L. M., Demko, A. M., Diner, R. E., Giddings, A., Koester, I., Pagniello, C. M. L. S., Paulsen, M.-L., Ramirez-Valdez, A., Schwenck, S. M., Yen, N. K., Zill, M. E., & Franks, P. J. S. (2016). Biological impacts of the 2013–2015 warm-water anomaly in the Northeast Pacific: Winners, losers, and the future. *Oceanography*, *29*(2), 273–285. <http://www.jstor.org/stable/24862690>
- Chavez, F. P., & Messié, M. (2009). A comparison of Eastern Boundary Upwelling Ecosystems. *Progress in Oceanography*, *83*(1), 80–96. <https://doi.org/10.1016/j.pocean.2009.07.032>
- Di Lorenzo, E., Schneider, N., Cobb, K. M., Franks, P. J. S., Chhak, K., Miller, A. J., McWilliams, J. C., Bograd, S. J., Arango, H., Curchitser, E., Powell, T. M., & Rivière, P. (2008). North Pacific Gyre Oscillation links ocean climate and ecosystem change. *Geophysical Research Letters*, *35*(8). <https://doi.org/10.1029/2007gl032838>
- Fu, L.-L., & Ferrari, R. (2008). Observing oceanic submesoscale processes from space. *Eos, Transactions American Geophysical Union*, *89*(48), 488–488. <https://doi.org/https://doi.org/10.1029/2008EO480003>
- Fu, L.-L., & Smith, R. D. (1996). Global ocean circulation from satellite altimetry and high-resolution computer simulation. *Bulletin of the American Meteorological Society*, *77*(11), 2625–2636. [https://doi.org/10.1175/1520-0477\(1996\)077<2625:Gocfsa>2.0.Co;2](https://doi.org/10.1175/1520-0477(1996)077<2625:Gocfsa>2.0.Co;2)
- García-Reyes, M., & Largier, J. L. (2012). Seasonality of coastal upwelling off central and northern California: New insights, including temporal and spatial variability. *Journal of Geophysical Research: Oceans*, *117*(C3). <https://doi.org/https://doi.org/10.1029/2011JC007629>
- Garfield, N., Collins, C. A., Paquette, R. G., & Carter, E. (1999). Lagrangian Exploration of the California Undercurrent, 1992–95. *Journal of Physical Oceanography*, *29*(4), 560–583. [https://doi.org/10.1175/1520-0485\(1999\)029<0560:leotcu>2.0.co;2](https://doi.org/10.1175/1520-0485(1999)029<0560:leotcu>2.0.co;2)
- Kurian, J., Colas, F., Capet, X., McWilliams, J. C., & Chelton, D. B. (2011). Eddy properties in the California Current System. *Journal of Geophysical Research: Oceans*, *116*(C8). <https://doi.org/https://doi.org/10.1029/2010JC006895>
- Mantua, N. J., & Hare, S. R. (2002). The Pacific Decadal Oscillation. *Journal of Oceanography*, *58*(1), 35–44. <https://doi.org/10.1023/A:1015820616384>
- Mantua, N. J., Hare, S. R., Zhang, Y., Wallace, J. M., & Francis, R. C. (1997). A Pacific Interdecadal Climate Oscillation with Impacts on Salmon Production. *Bulletin of the American Meteorological Society*, *78*(6), 1069–1080. [https://doi.org/10.1175/1520-0477\(1997\)078<1069:apicow>2.0.co;2](https://doi.org/10.1175/1520-0477(1997)078<1069:apicow>2.0.co;2)
- McClatchie, S. (2014). *Regional fisheries oceanography of the California Current System*. Springer.
- Pelland, N. A., Eriksen, C. C., & Lee, C. M. (2013). Subthermocline Eddies over the Washington Continental Slope as Observed by Seagliders, 2003–09. *Journal of Physical Oceanography*, *43*(10), 2025–2053. <https://doi.org/10.1175/jpo-d-12-086.1>

- Robinson, A. R., & Brink, K. H. (2006). *The global coastal ocean: interdisciplinary regional studies and syntheses* (Vol. 14A). Harvard University Press.
- Roemmich, D., Johnson, G. C., Riser, S., Davis, R., Gilson, J., Owens, W. B., Garzoli, S. L., Schmid, C., & Ignaszewski, M. (2009). The Argo Program: Observing the global ocean with profiling floats. *Oceanography*, 22(2), 34-43. <http://www.jstor.org/stable/24860957>
- Rudnick, D. L. (2016). Ocean Research Enabled by Underwater Gliders. *Annual Review of Marine Science*, 8(1), 519-541. <https://doi.org/10.1146/annurev-marine-122414-033913>
- Rudnick, D. L., Zaba, K. D., Todd, R. E., & Davis, R. E. (2017). A climatology of the California Current System from a network of underwater gliders. *Progress in Oceanography*, 154, 64-106. <https://doi.org/10.1016/j.pocean.2017.03.002>
- Ryther, J. H. (1969). Photosynthesis and Fish Production in the Sea. *Science*, 166(3901), 72-76. <https://doi.org/doi:10.1126/science.166.3901.72>
- Strub, P. T., & James, C. (2000). Altimeter-derived variability of surface velocities in the California Current System: 2. Seasonal circulation and eddy statistics. *Deep Sea Research Part II: Topical Studies in Oceanography*, 47(5), 831-870. [https://doi.org/https://doi.org/10.1016/S0967-0645\(99\)00129-0](https://doi.org/https://doi.org/10.1016/S0967-0645(99)00129-0)
- Wyrki, K. (1962). The oxygen minima in relation to ocean circulation. *Deep Sea Research and Oceanographic Abstracts*, 9(1), 11-23. [https://doi.org/https://doi.org/10.1016/0011-7471\(62\)90243-7](https://doi.org/https://doi.org/10.1016/0011-7471(62)90243-7)
- Zaba, K. D., & Rudnick, D. L. (2016). The 2014–2015 warming anomaly in the Southern California Current System observed by underwater gliders. *Geophysical Research Letters*, 43(3), 1241-1248. <https://doi.org/10.1002/2015gl067550>

CHAPTER 1: Temperature and salinity extremes from 2014-2019 in the California Current System and its source waters

Abstract

The California Current System in the eastern North Pacific Ocean has experienced record high temperatures since the marine heatwave of 2014-2016. Here we show, through a compilation of data from shipboard hydrography, ocean gliders, and the Argo floats, that a high-salinity anomaly affected the California Current System from 2017-2019 in addition to the anomalously high temperatures. The salinity anomaly formed in 2015 in the North Pacific Subtropical Gyre and was subsequently advected into the California Current System, in a generation mechanism different from the events leading to the marine heatwaves of 2013/2014 and 2019 in the North Pacific. The salinity anomaly was unique in at least 16 years with an annual mean deviation from the long-term average greater than 0.2 and anomalies greater than 0.7 observed offshore. Our results imply that different source waters were found in the California Current from 2017-2019, with the near-surface California Current salinity rivaling that of the California Undercurrent.

Introduction

The California Current System (CCS) is the eastern boundary current system in the North Pacific. The CCS consists of an equatorward-flowing, surface-intensified current, the California Current, and a subsurface-intensified, poleward-flowing current, the California Undercurrent. These mean currents are accompanied by numerous eddying features and an annual cycle including wind-driven upwelling. The coastal environment of the central and southern CCS has experienced anomalously high temperature conditions since 2014 (Rudnick et al., 2017a; Thompson et al., 2019; Zaba et al., 2020; Zaba et al., 2018). The high temperature anomaly began in 2014 with the marine heatwave (MHW) that affected the central and southern CCS (Zaba & Rudnick, 2016). Positive temperature anomalies in the surface 50 m of the CCS during 2014-2015 were above 4 °C (Zaba & Rudnick, 2016). We document changes in temperature and salinity that are unique to the time period 2014-2019, expanding on previous studies that have focused on temperature alone. In particular, we document a salinity anomaly that affected the CCS from

2017-2019 but formed offshore in 2015. The salinity anomaly was noted in the annual report describing the physical and biological condition of the CCS organized and published by the California Cooperative Oceanic Fisheries Investigations (CalCOFI) (Thompson et al., 2019; Thompson et al., 2018). The relevance of regional salinity changes is that they often indicate changes of source water which may have a large impact on the marine ecosystem.

During the time period from 2014-2019, some established relationships between sea surface temperature (SST) or SST indices and biological indicators reversed, diverging from patterns established up to 2010. Before the onset of the 2014-2016 MHW, fluctuations in sardine and anchovy were largely believed to be related to SST (Chavez et al., 2003; Larry D. Jacobson & A. D. MacCall, 1995; Larry D. Jacobson & Alec D. MacCall, 1995; Lindegren & Checkley, 2012) with higher sardine populations under warm conditions and higher anchovy populations under cool conditions, though there were alternate hypotheses (Baumgartner et al., 1992; McClatchie, 2012; McClatchie et al., 2017). The abundance of salmon was similarly correlated with a large-scale index of SST, the Pacific Decadal Oscillation (PDO) (Mantua et al., 1997). In 2016-2017 northern anchovy was found in high abundance during high SST off central and southern California while Pacific sardine abundance was relatively low (Zwolinski et al., 2017; Zwolinski et al., 2019), opposite to the relationship established from 1950-2002 (Chavez et al., 2003). Subsequently, in 2019, northern anchovy were abundant throughout the CCS while Pacific sardine were locally abundant off central California (Thompson et al., 2019). This is similar to findings in the Gulf of Alaska from 2014-2019, a period of rapid ocean warming, where the relationship between the PDO and salmon abundance switched from a positive or neutral correlation to a negative correlation (Litzow, Malick, et al., 2020). The implication is that previously established correlations of biological abundance with large-scale SST indices did not have predictive power during the MHW of 2014-2016 and its aftermath (Muhling et al., 2020). In contrast, from 1983-2016 young of the year (YOY) rockfish abundance was found to be related to salinity on the isopycnal 26.0 kg m^{-3} , interpreted to be an indicator of changes in the water mass composition of the CCS (Schroeder et al., 2019). Here, we examine the temperature and salinity record to identify changes in the physical environment.

Results and Discussion

The temperature record from the southern California Current at 10 m (Fig. 1.1a) from the California Cooperative Oceanic Fisheries Investigations (CalCOFI) and California Underwater Glider Network (CUGN) demonstrates the unusually high temperature event in 2014-2016 (Fig. 1.1b). The temperature in 2015 was the highest in the California Current based on the time series of almost 70 years. The 1997/1998 El Niño event does not show up strongly in the time series at 10 m because larger anomalies in temperature were observed at depth and inshore due to the influence of the California Undercurrent and thermocline displacement (Bograd & Lynn, 2001; Lynn & Bograd, 2002). The extreme in temperature in 2015 is followed by cooler conditions, but from 2016-2019, the California Current was still warmer than the baseline, here taken as the mean of years 2007-2013 (see Methods for details). The 2007-2013 baseline is chosen for all three datasets used in this manuscript: CalCOFI, CUGN, and Argo. The CalCOFI 2007-2013 time period is 0.55 °C cooler and 0.010 fresher than the often-reported CalCOFI baseline of 1984-2012 and 0.33 °C cooler and 0.037 fresher than the full time series from 1950-2019 here. There is discussion in the literature of two separate MHWs with different generation mechanisms in the Northeast Pacific, one beginning in the winter of 2013/2014 (Bond et al., 2015) and one beginning in the summer of 2019 (Amaya et al., 2020); however, the southern CCS has had one extended period of elevated temperatures. The CUGN and CalCOFI temperature anomaly time series agree well during the MHW from 2014-2016, while they agree within the 99% confidence interval of the CalCOFI time series in the times before and after.

From 2017-2019, in addition to a warm temperature anomaly, the CCS experienced a high salinity anomaly. The salinity anomaly, identified offshore at 10 m from CUGN and CalCOFI observations on Lines 80.0 and 90.0, had an annual anomaly approaching 0.3 in 2018 (Fig. 1.1c). The 2017-2019 salinity anomaly was the strongest on record in this region since 2001. The period since 2003 was one of relative low salinity, gradually increasing with small interannual fluctuations. The 2017-2019 salinity anomaly was the culmination of this 15-year period of increasing salinity. The CUGN and CalCOFI salinity anomaly time series match remarkably well.

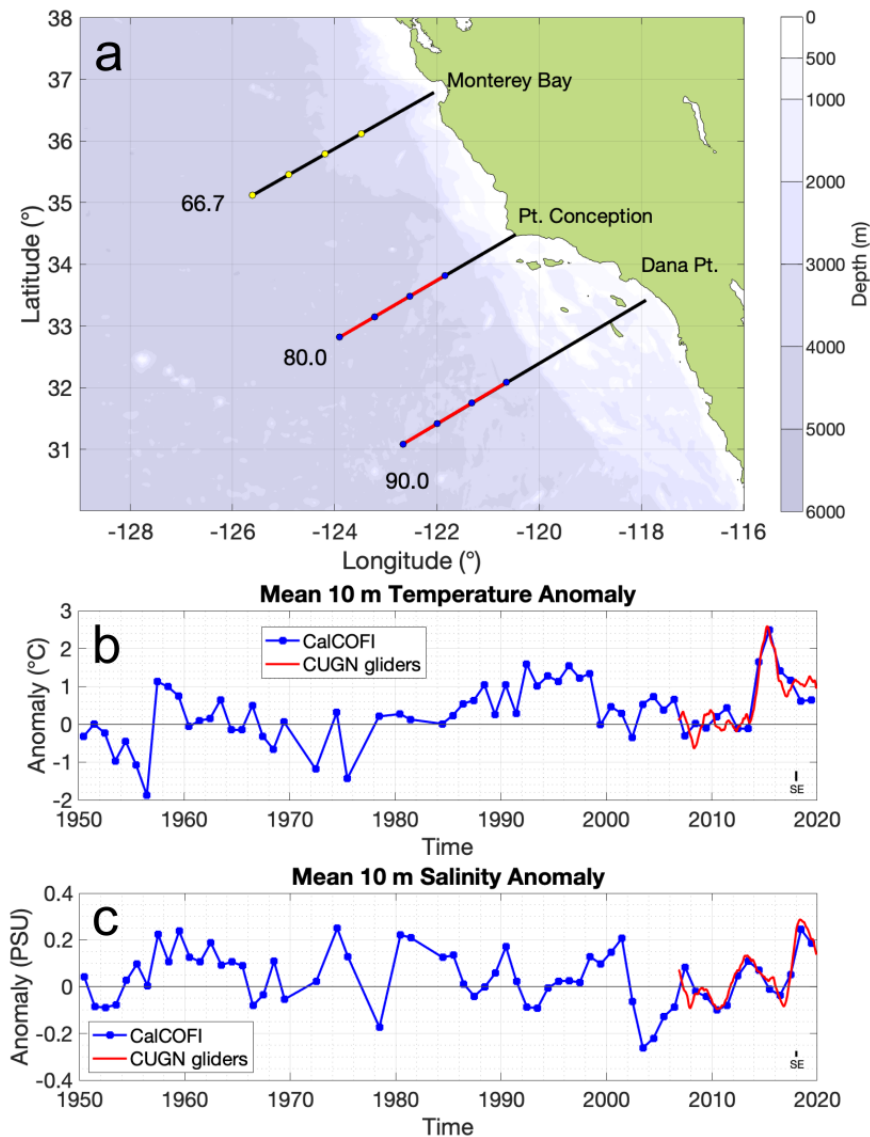


Figure 1.1 Historical offshore temperature and salinity observations in the California Current (a) Location of the CUGN glider Lines 66.7, 80.0, and 90.0 (black). The location of the portions of Line 80.0 and Line 90.0 of the CUGN glider lines used in the time series are overplotted in red while CalCOFI stations 70, 80, 90, and 100 along Lines 80.0 and Lines 90.0 used in the time series are plotted in blue dots. Stations 70, 80, 90, and 100 of Line 66.7 are plotted in yellow dots. (b) The 10 m annual mean temperature anomaly ($^{\circ}\text{C}$) from CalCOFI (blue) and 365-day lowpass filtered temperature anomaly ($^{\circ}\text{C}$) from CUGN (red). (c) The 10 m annual mean salinity anomaly from CalCOFI (blue) and 365-day lowpass filtered salinity anomaly from CUGN (red). The CalCOFI average is calculated from stations 70, 80, 90, and 100 on Lines 80.0 and 90.0 while the CUGN average is from the distance between stations 70-100 on Lines 80.0 and 90.0. The average annual standard error of the CalCOFI temperature anomaly (0.26°C) and salinity anomaly (0.025) is plotted as a black bar in the lower right-hand corner in (b) and (c) respectively.

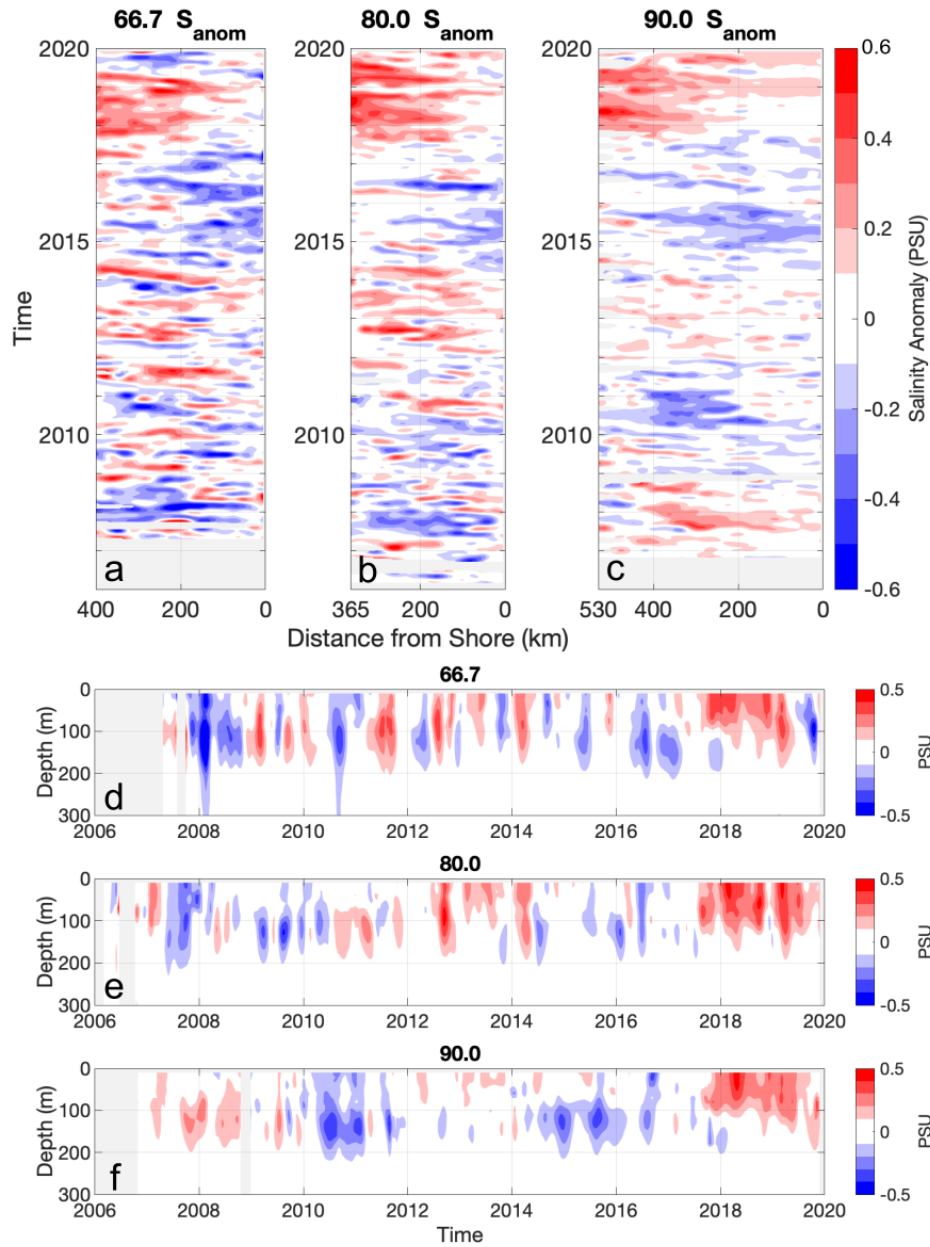


Figure 1.2 Hovmöller diagrams of salinity anomaly from CUGN gliders on Lines 66.7, 80.0, and 90.0. (a-c) 10-100 m depth-averaged salinity anomaly and (d-f) spatially averaged salinity anomaly from the distance between CalCOFI stations 70-100 on each of the respective lines.

Hovmöller diagrams of depth-averaged salinity anomaly from 10-100 m from CUGN gliders (Figs. 1.2a-c) show how the 2017-2019 salinity anomaly approached the coast. The 10-100 m depth range was chosen to focus on the surface mixed layer and to avoid the halocline which exists in the mean from 105 – 135 m depth in the offshore portions of Lines 66.7, 80.0, and 90.0 examined here (Fig. 1.3).

Salinity anomalies plotted against depth near the region of the halocline are often caused by isopycnal heave. The salinity anomaly began in early 2017 on transect Line 66.7 (for location see Figure 1.1a) and in middle and late 2017 on Lines 80.0 and 90.0 respectively. The salinity anomaly was stronger offshore and appeared to pass through the northern line, Line 66.7, before the southern lines, Line 80.0 and Line 90.0. The high salinity anomaly ended on Line 66.7 in the middle of 2019 while continuing through the end of 2019 on Lines 80.0 and 90.0. Peak salinity anomalies averaged from 10-100 m reached a maximum of 0.6 on each of the three lines. Plots of salinity anomaly over depth and time, averaged over

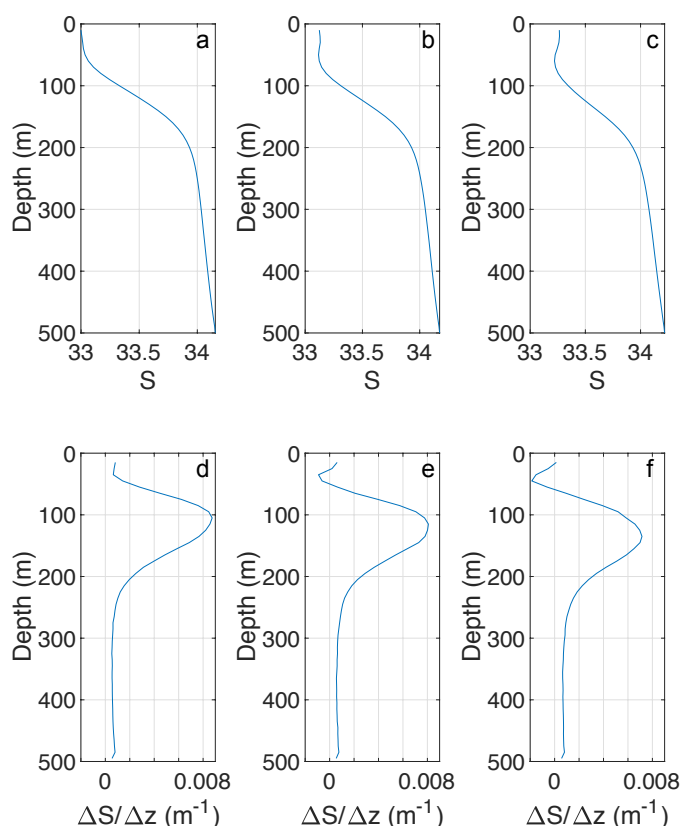


Figure 1.3 The profile of mean practical salinity and depth and the gradient of mean practical salinity over depth in the offshore region between stations 70-100 on Lines 66.7, 80.0, and 90.0. The mean is between years 2007-2013 for Lines 80.0 and 90.0 and 2008-2013 for Line 66.7.

the distance between stations 70-100 of the CalCOFI grid, demonstrate that the salinity anomaly was largest in the top 100 m (Figs. 1.2d-f). Due to high salinity anomalies that occurred first on the offshore

edge on Line 66.7 and that did not dominate the across-shore average, the salinity anomaly begins at near the same time on all three lines when viewed from the depth versus time perspective.

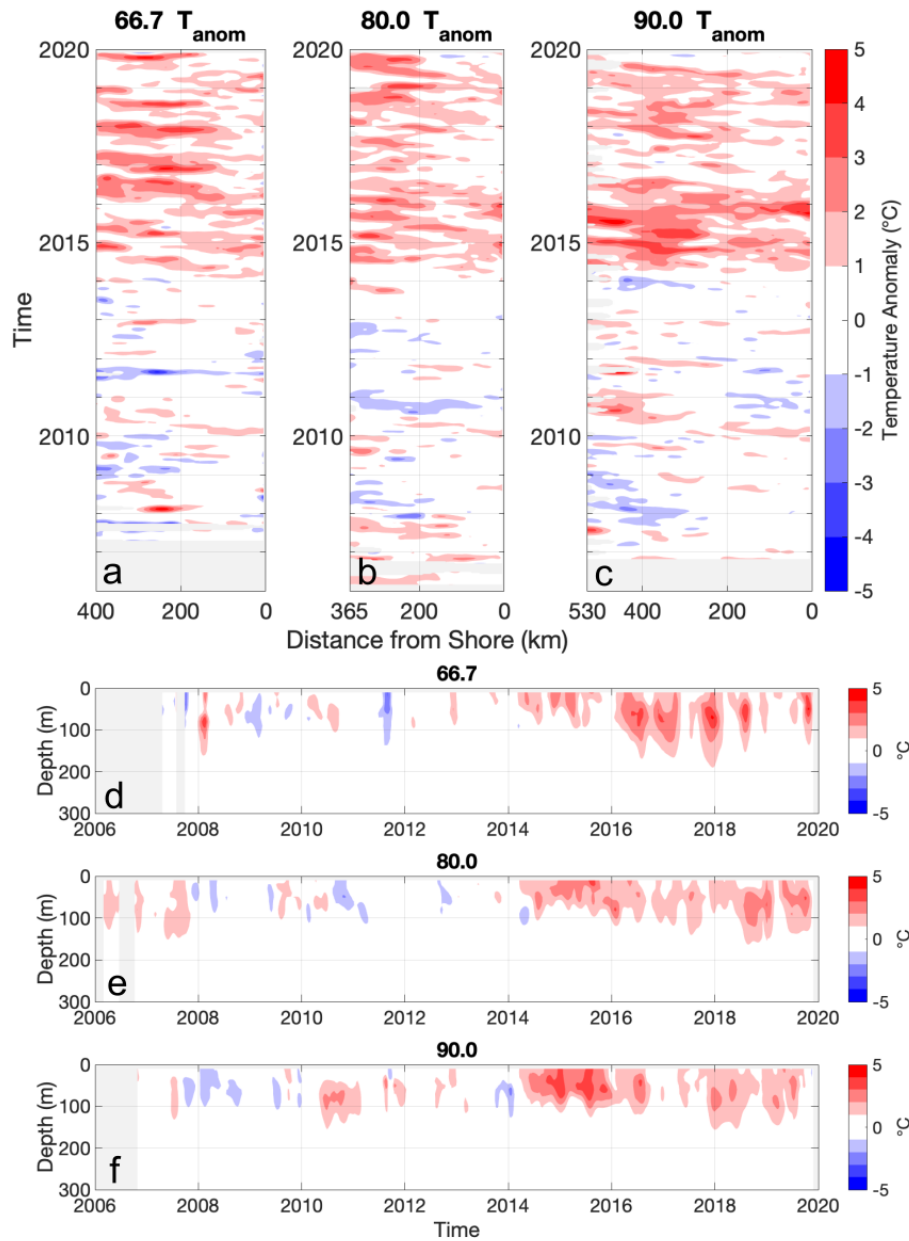


Figure 1.4 Hovmöller diagrams of temperature anomaly ($^{\circ}\text{C}$) from CUGN gliders on Lines 66.7, 80.0, and 90.0. (a-c) 10-100 m depth-averaged temperature anomaly and (d-f) spatially averaged temperature anomaly from the distance between CalCOFI stations 70-100 on each of the respective lines.

Hovmöller diagrams of depth-averaged temperature anomaly from 10-100 m show the salinity anomaly in contrast with the anomalous warmth from 2014 through the end of 2019 on all three lines (Figs. 1.4a-c). The 10-100 m depth-averaged temperature anomaly during 2014-2019 was frequently

greater than 3 °C and exceeded 4 °C on Lines 66.7 and 90.0, while it approached 4 °C on Line 80.0. The temperature anomaly was also concentrated in the top 100 m (Figs. 1.4d-f) as seen from plots of temperature anomaly over depth and time, averaged over the distance between stations 70-100 of the CalCOFI grid. The across-shore averaged plots show that the high temperature anomaly remained in the central and southern CCS after 2016 and until 2019.

The origin of the salinity anomaly is examined in the greater Pacific Ocean. Basin-wide salinity anomalies at 10 db from the Roemmich-Gilson (R-G) climatology of Argo float data (Roemmich & Gilson, 2009) demonstrate that the anomaly originated offshore in September 2015, years before its detection along the California coast (Fig. 1.5). In the 8-month interval plots, the anomaly appears in September 2015 and then follows the path of the surface geopotential height contours east towards the coast and then south towards the equator. The plotted monthly surface geopotential height contours are approximate streamlines of the ocean currents and indicate the portion of the North Pacific Current that feeds into the California Current and the southward limb of the North Pacific Subtropical Gyre. While a pattern of positive salinity anomaly between 160° and 170 °W at 40 °N also occurred in the Argo data in 2010-2011, 2017-2019 was the only instance in the Argo record (2004-2019) when an anomaly persisted, intensified, and subsequently moved equatorward along the coast. The persistence of the salinity anomaly from 2015 to at least 2019 in the eastern North Pacific is unique in the Argo record.

The salinity anomaly had a large spatial extent not measured by the coastal CUGN lines or CalCOFI hydrography but captured by Argo. The salinity anomaly was quite strong offshore; in September 2017, the positive salinity anomaly at 35.5 °N, 135.5 °W was 0.78. The edge of CUGN Line 66.7, corresponding to station 100 on the CalCOFI grid, is 35.5 °N 125.5 °W, which is usually well approximated by the location of the 1951 m geopotential height contour. Considering the plots of May 2016 and January 2017, the salinity anomaly existed offshore but did not reach the edge of the CUGN lines. This is consistent with CUGN observations which only showed a strong salinity anomaly after January 2017 on Line 66.7 and June 2017 on Lines 80.0 and 90.0. In addition, not of primary interest in this paper, but readily apparent, is an extremely strong fresh salinity anomaly that formed to the west of

the salinity anomaly and also appears to be advecting eastward in the North Pacific Current as of 2019. It is possible that this fresh anomaly will appear in the CCS in coming years.

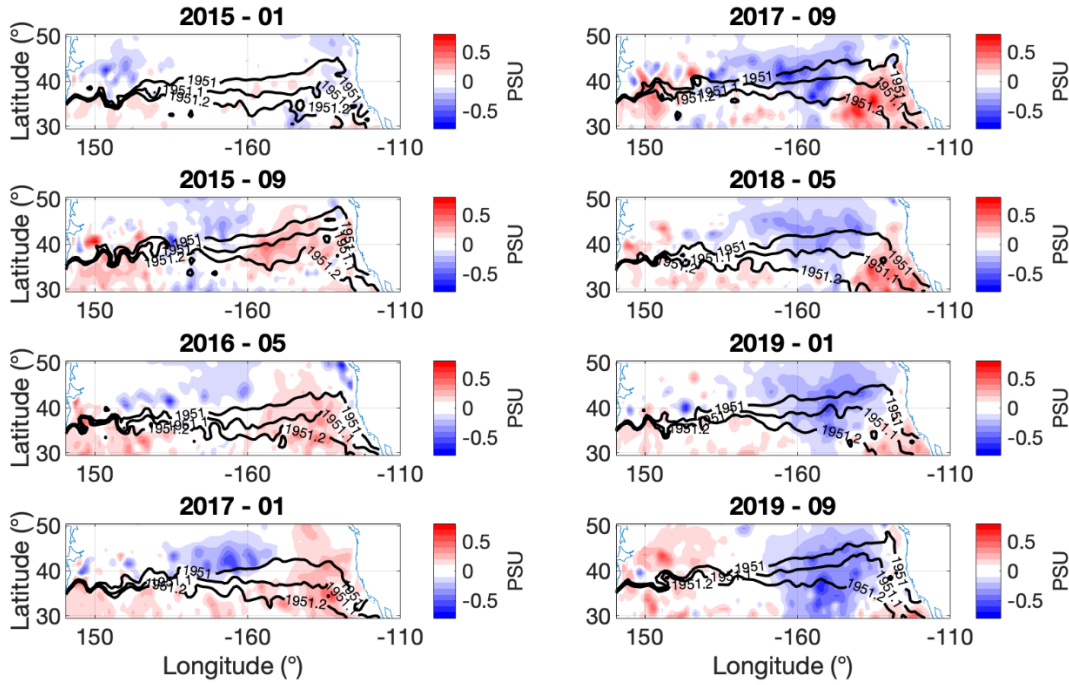


Figure 1.5 Plots of salinity anomaly at 10 db from the R-G Argo climatology. Plots are in 8-month intervals including (a) January 2015 (b) September 2015 (c) May 2016 (d) January 2017 (e) September 2017 (f) May 2018 (g) January 2019 and (h) September 2019. The geopotential height (m) of select contours of the North Pacific Current that contribute to California Current and southward limb of the North Pacific Subtropical Gyre are overplotted for each month. Notice that the aspect ratio of degrees latitude to degrees longitude has been stretched in the latitudinal direction to better show characteristics of the salinity anomaly.

Possible causes of the salinity anomaly include advection, surface fluxes by precipitation and evaporation (E-P), and vertical turbulent entrainment. From the Argo and CUGN data, we suggest that one important factor is advection. The eastward salt flux by the North Pacific Current in the surface 100 m across 135 °W from 35-44 °N (Fig. 1.6a) was calculated and shows a large positive anomaly which begins in the second half of 2016, peaks in 2017, and ends in mid-2018. This matches the timing of the positive salinity anomalies that moved through the region according to the salinity anomaly plots at 10 db (Fig. 1.5) and provides strong evidence that the salinity anomaly was advected east into the region where the California Current begins. Along CUGN lines, an increased southward advection of salt is not clear,

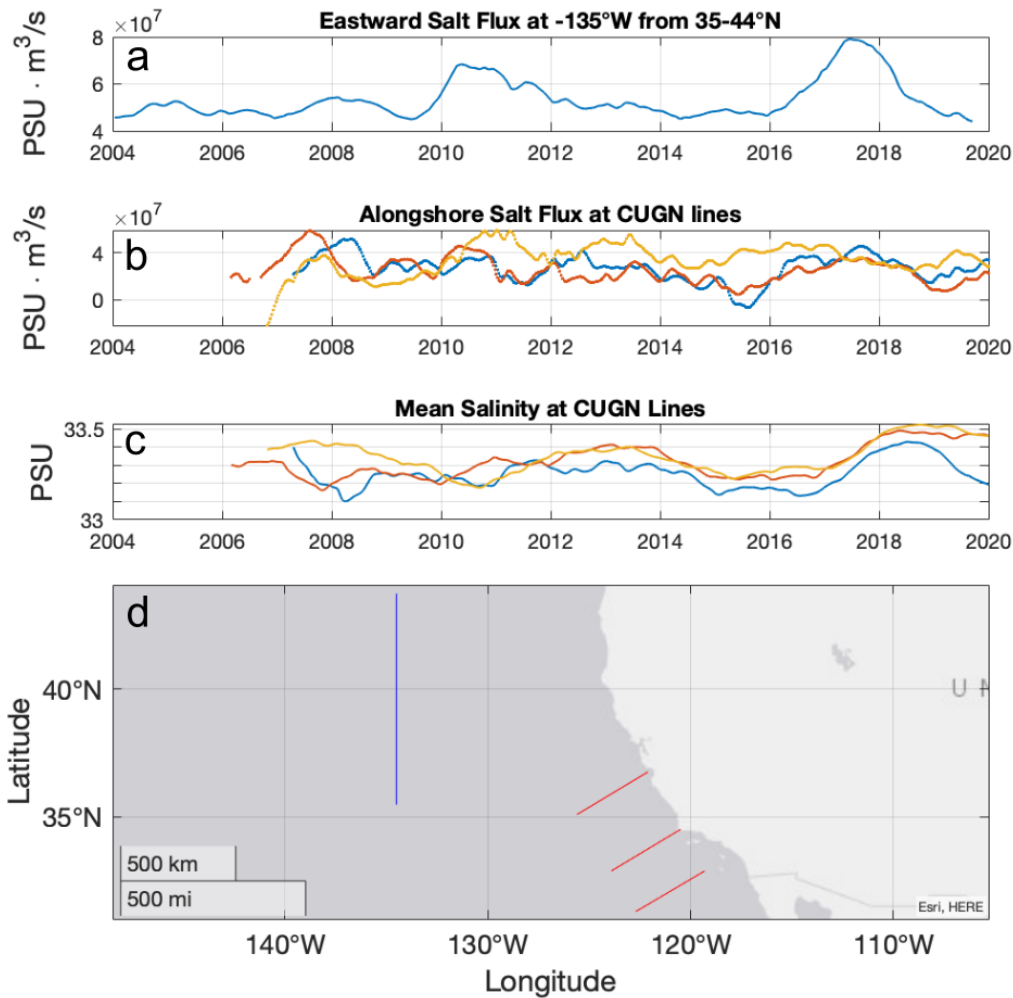


Figure 1.6 Salt flux in the North Pacific and CCS. (a) Eastward salt flux integrated over the surface 100 m at 135 °W from 35-44 °N ($\text{m}^3 \text{s}^{-1}$) (b) Alongshore salt flux integrated over the surface 100 m at CUGN lines ($\text{m}^3 \text{s}^{-1}$). (c) Mean salinity averaged over the top 100 m at CUGN lines. For both (b-c) the across-shore extent of CUGN lines is the equivalent of from CalCOFI stations 50-100, and Line 66.7 is plotted in blue, Line 80.0 in orange, and Line 90.0 in yellow. (d) Location of the North Pacific Current salt flux calculation (blue) and the three CUGN lines (red) on which salt flux and mean salinity were calculated.

however, even though the mean salinity, as averaged over the top 100 m and over the entire lines, increases in 2017-2019 (Figs. 1.6b-c). Here, southward velocities are treated as positive so consequently a positive value indicates southward advection. From 2017-2019, the salt flux is positive on all three lines indicating the mean flow was southward, consistent with the presence of the California Current. The

alongshore salt flux may be difficult to measure in an eddying environment like in the CCS. The salinity anomaly of 2017-2019 was roughly 0.2 compared to a mean of 33.3. In contrast, the standard deviation of the alongshore geostrophic velocity was 0.03 m s^{-1} compared to a mean geostrophic velocity of 0.02 m s^{-1} southward (over the entire lines 66.7, 80.0, and 90.0), emphasizing the eddying nature of the CCS. Thus, changes in salt flux were dominated by changes in volume flux in the CUGN region. There is also possibly an onshore component, as suggested from the Argo salinity anomaly plots (Fig. 1.5). A more complete analysis of the causes of the salinity anomaly may require an assimilative ocean circulation model.

From 2013-2019, it is apparent that numerous environmental forcing mechanisms were abnormal in the North Pacific. The winter 2013/2014 MHW in the North Pacific is thought to be due to changes in ocean advection and reduced heat loss from the ocean to the atmosphere (Bond et al., 2015). The extension of the MHW through 2016 and transformation into a coastal SST pattern may rely on complex interactions between the ocean and atmosphere (Di Lorenzo & Mantua, 2016) while its extension through 2019 remains to be explained. Local mechanisms in the CCS during 2014-2016 include increased heat flux from the atmosphere and increased heat flux from horizontal and vertical advection (Zaba et al., 2020). The summer 2019 MHW in the North Pacific is thought have formed due to increased short wave radiation on the surface ocean and reduced surface winds, which reduced heat loss from the ocean to the atmosphere and reduced mixing and entrainment (Amaya et al., 2020). While the salinity anomaly advected into the source waters of the California Current, the possible causes for the salinity anomaly's formation in 2015 in the central North Pacific are increased evaporation, increased entrainment from below, or advection of saltier water from further south in the subtropical gyre.

The salinity anomaly was not predicted by the North Pacific Gyre Oscillation (NPGO), a climate index thought to be relevant to salinity in the CCS. The NPGO, the 2nd EOF of sea surface height anomaly in the North Pacific, was in a strongly negative phase from October 2017 to at least June 2019 (Thompson et al., 2019), and the negative phase, or phase with reduced sea surface height anomaly difference between the Alaska Gyre and the North Pacific Subtropical Gyre, has been associated with

fresh, or negative, sea surface salinity anomalies (Di Lorenzo et al., 2008). In particular, the positive (negative) phase of the NPGO was correlated with greater (less) upwelling in the past which was the explanation for why salinity and other variables were related to the NPGO (Di Lorenzo et al., 2008). One explanation is that the causal mechanism that linked CCS salinity to the NPGO may have changed (Litzow, Hunsicker, et al., 2020; Thompson et al., 2018). Another is that the relationship between salinity and the NPGO was based on relatively short records and may not hold as longer climate records are collected.

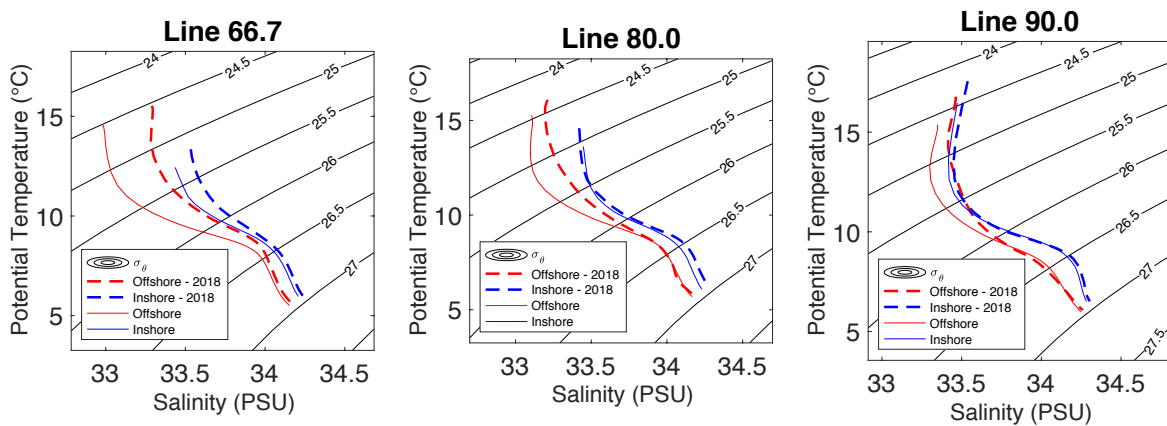


Figure 1.7 T-S diagrams of 2018 compared to the mean. (a) Line 66.7 (b) Line 80.0 and (c) Line 90.0. Inshore is defined as 0-100 km and offshore as 200-400 km from shore. The mean is from 2007-2013 on Lines 80.0 and 90.0 and from 2008-2013 on Line 66.7.

The California Current is usually the source of fresher water into the CCS, and yet in 2017-2019, it was a source of salty water that spread from offshore towards the coast. The values of salinity in the California Current in 2018 rival values in the California Undercurrent at the surface (Fig. 1.7), especially on Line 90.0. From the temperature and salinity (T-S) diagrams, it is clear that the surface temperature in 2018 was warmer than the mean both inshore (0-100 km) and offshore (200-400 km) while the surface salinity was significantly saltier offshore (200-400 km). Figure 1.7 shows the top sections of curves in 2018 (dashed red for offshore, dashed blue for inshore) are located further up (warmer) and further to the right (saltier). The high salinity of the California Current and the evidence presented that the high salinity was advected into the region point to new source waters for the California Current from 2017-2019. In

particular, the formation of the salinity anomaly in the North Pacific Gyre suggests that increased Eastern North Pacific Central Water, which is relatively warmer and saltier, may have been in the California Current from 2017-2019.

With respect to biological impacts, new source water for the California Current from 2017-2019 may be important. Unusual water masses coming into the CCS may bring different biological and biogeochemical signatures to the local environment (Bograd et al., 2019). In the CCS, zooplankton displacement volume has been found to be correlated with advection of the California Current (Bernal & McGowan, 1981; Chelton, 1981; McClatchie, 2014b), where displacement volume may be impacted by zooplankton body size and species composition. In light of recent sardine and anchovy abundance anomalies, reanalysis of fisheries models from 2005-2014 suggest that SST alone is not an adequate indicator of sardine biomass (Zwolinski & Demer, 2019). A plausible hypothesis is that different source water in 2017-2019 of the California Current brought water with different nutrient properties that supported a different plankton population. With respect to YOY rockfish, the relationship of higher abundance during cooler and fresher conditions (Schroeder et al., 2019) appears to have held up in 2017-2019 with lower abundances observed in the warmer and saltier conditions (Thompson et al., 2019). Understanding source water changes may help with a more mechanistic understanding of forage fish population dynamics, which is needed to understand population fluctuations in a changing climate (Checkley et al., 2017). Specifically, larval survival and recruitment may govern the population fluctuations of the species, and oceanic conditions may affect early life history survival. The mechanistic understanding of forage fish abundance is important as the CCS, combined with the other eastern boundary upwelling systems represent around 20% of global marine fishing take over an area of around 1% of the global ocean (Chavez & Messié, 2009).

The regional effects of climate variability may be more diverse than just increases in atmospheric or ocean temperature; here, it is shown that concomitant with anomalously high temperatures, a major regional current experienced a source water change and extreme salinity values. Experiencing both temperature anomalies and other effects such as source water changes concurrently may have a large

impact on the ocean ecosystem. Both salinity and temperature ocean observations should be sustained and further analyzed to better understand the marine physical environment as it changes.

Data and Methods

Data came from three main sources: underwater gliders, shipboard hydrography, and Argo. Observations within 500 km of the coast were taken from gliders in the CUGN (Rudnick, 2016; Rudnick et al., 2017a). CUGN gliders have been running off of the California coast since 2006 along three traditional CalCOFI hydrographic lines: Line 66.7 off of Monterey Bay, Line 80.0 off of Point Conception, and Line 90.0 from Dana Point (Fig. 1.1a). The gliders profile to 500 m completing a cycle from the surface to depth and back in 3 h and covering a horizontal distance of 3 km in that time. Gliders complete sections on the across-shore lines in roughly 2-3 weeks. A climatology of the CUGN data is available which includes the annual cycle and anomalies of measured variables temperature and salinity. Salinity in this manuscript is reported on the Practical Salinity Scale 1978, which is unitless. The annual cycle is computed from full years 2007-2013 on Lines 80.0 and 90.0 and 2008-2013 for Line 66.7 using a constant and three harmonics (Rudnick et al., 2017a, 2017b). Anomalies from this annual cycle are objectively mapped. Areas of the objective map where the ratio of error to signal variance is larger than 0.3 are masked out. The climatology is calculated in a gridded format with spacing of 10 days in time, 5 km in horizontal distance, and 10 m in depth with depth bins centered on 10 m, 20 m, and so on to 500 m. Analyses of temperature anomaly and salinity anomaly here used the CUGN climatology. The climatology also includes the alongshore geostrophic velocity calculated by referencing geostrophic shear to the glider's depth-average velocity (Rudnick et al., 2018). The calculation of alongshore salt flux used the geostrophic velocity and salinity of the CUGN climatology over the top 100 m and over the distance between CalCOFI stations 50-100 on each of the Lines 66.7, 80, and 90.

The CalCOFI hydrographic bottle-sample salinity and temperature from 1950-2019 was used to provide historical perspective. The CalCOFI program has been taking bottle samples of salinity and temperature since 1949 on Lines 80.0 and 90.0. The sampling pattern changed during the first few decades of CalCOFI, including years without cruises in the 1970s. A consistent sampling plan has been

in place on Lines 80.0 and 90.0 since the 1980s with four cruises per year (McClatchie, 2014a). CalCOFI has not maintained a consistent presence on Line 66.7. The CalCOFI program originally created a grid of offshore transects along the west coast of North America from Line 10 at the US-Canada border to Line 120 off Point Eugenia, Baja California, Mexico; however, only a core 66 station sampling survey spanning Lines 76.7-93.3 have been sampled for the entire time-series (though with a period of less regular sampling in the 1970s-mid-1980s) (McClatchie, 2014a). A CalCOFI time series was created using an annual average of data from Lines 80.0 and 90.0, stations 70, 80, 90, and 100 at 10 m depth. Data from years when both Line 80.0 and Line 90.0 had salinity data were included in the time series. CalCOFI anomalies were calculated as differences from the mean during 2007-2013, to be consistent with the mean used in the CUGN climatology. For comparison, CUGN climatology salinity and temperature anomalies at 10 m were averaged over the distance between stations 70 and 100 on Lines 80.0 and 90.0. Subsequently, a 365-day running mean was applied to the CUGN salinity and temperature anomaly time series.

The standard error of the mean was calculated for each year of the CalCOFI time series. The average standard error of all years for the salinity anomaly was 0.025, small compared to the interannual variations in the time series which were often 0.2. During a year with four cruises and data at all stations at 10 m, the CalCOFI sample size was $n=32$. The average standard error of all years of the CUGN time series was 0.0024 where the sample size was $n=3293$ climatology grid points per year. The standard error of the CUGN time series of salinity anomaly was less than that of CalCOFI, even considering autocorrelation in time and space of the CUGN profiles (reducing the effective CUGN sample size by a factor of 100 would make the standard errors comparable), so the standard error of CalCOFI was reported on the time series plot. Similarly, the standard error of the mean of the temperature anomalies was 0.26 °C for CalCOFI and 0.013 °C for CUGN, so only the CalCOFI standard error was reported on the plot. Importantly, with grid points every 5 km, the CUGN climatology is able to resolve mesoscale eddy variability, which can have a signature of 0.2 and 1 °C and greater in the CCS.

Salinity in the open ocean was from the R-G climatology of Argo data profiles (Argo, 2000; Roemmich & Gilson, 2009). The R-G climatology calculates the monthly values of temperature and practical salinity on a $1^\circ \times 1^\circ$ grid with 58 pressure levels from 2.5 to 1975 db. The gridded product is produced by a weighted least squares analysis that calculates the mean from the nearest 300 Argo observations, followed by objective analysis of the anomalies. An annual cycle for R-G salinity was calculated at every grid cell and pressure level using a constant and three harmonics for the full years 2007-2013, matching the method used to calculate the annual cycle for the CUGN climatology. Salinity anomaly was calculated as the difference from this annual cycle. Geopotential height, Z , was calculated by

$$Z = -\frac{1}{9.8} \int_{p_1}^{p_2} \frac{1}{\rho} dp \quad (1)$$

using the in-situ density, ρ , calculated from the R-G temperature and salinity and then integrating in pressure from $p_1=1975$ db to $p_2=2.5$ db (Talley et al., 2011). The geostrophic velocity was calculated using

$$f(v_2 - v_1) = -9.8 \frac{\partial Z}{\partial x}, \quad (2)$$

$$f(u_2 - u_1) = 9.8 \frac{dZ}{dy}, \quad (3)$$

where the velocities u_1 and v_1 at 1975 db were assumed to be zero. The salt flux was calculated over the top 100 m using the R-G climatology salinity and the calculated geostrophic velocity.

Chapter 1, in full, is a reprint of the material as it appears in: Ren, A.S. and Rudnick, D.L. (2021) Temperature and salinity extremes from 2014-2019 in the California Current System and its source waters. *Communications Earth & Environment*, 2(62). The dissertation author was the primary investigator and author of this paper.

References

- Amaya, D. J., Miller, A. J., Xie, S.-P., & Kosaka, Y. (2020). Physical drivers of the summer 2019 North Pacific marine heatwave. *Nature Communications*, *11*(1), 1903. <https://doi.org/10.1038/s41467-020-15820-w>
- Argo. (2000). *Argo float data and metadata from Global Data Assembly Centre (Argo GDAC)* [data set]. SEANOE [publisher]. <https://doi.org/10.17882/42182>
- Baumgartner, T. R., Soutar, A., & Ferreira-Bartrina, V. (1992). Reconstruction of the history of Pacific sardine and northern anchovy populations over the past two millennia from sediments of the Santa Barbara Basin. *CalCOFI Reports*, *33*, 24-40.
- Bernal, P. A., & McGowan, J. A. (1981). Advection and upwelling in the California Current. In *Coastal Upwelling* (Vol. 1, pp. 381-399).
- Bograd, S. J., & Lynn, R. J. (2001). Physical-biological coupling in the California Current during the 1997–99 El Niño–La Niña Cycle. *Geophysical Research Letters*, *28*(2), 275-278. <https://doi.org/10.1029/2000gl012047>
- Bograd, S. J., Schroeder, I. D., & Jacox, M. G. (2019). A water mass history of the Southern California current system. *Geophysical Research Letters*, *46*(12), 6690-6698. <https://doi.org/10.1029/2019gl082685>
- Bond, N. A., Cronin, M. F., Freeland, H., & Mantua, N. (2015). Causes and impacts of the 2014 warm anomaly in the NE Pacific. *Geophysical Research Letters*, *42*(9), 3414-3420. <https://doi.org/10.1002/2015gl063306>
- Chavez, F. P., & Messié, M. (2009). A comparison of Eastern Boundary Upwelling Ecosystems. *Progress in Oceanography*, *83*(1), 80-96. <https://doi.org/10.1016/j.pocean.2009.07.032>
- Chavez, F. P., Ryan, J., Lluch-Cota, S. E., & Niquen C., M. (2003). From Anchovies to Sardines and Back: Multidecadal Change in the Pacific Ocean. *Science*, *299*(5604), 217-221. <https://doi.org/10.1126/science.1075880>
- Checkley, D. M., Jr., Asch, R. G., & Rykaczewski, R. R. (2017). Climate, Anchovy, and Sardine. *Annual Review of Marine Science*, *9*(1), 469-493. <https://doi.org/10.1146/annurev-marine-122414-033819>
- Chelton, D. B. (1981). Interannual variability of the California Current-physical factors. *California Cooperative Oceanic Fisheries Investigations Reports*, *22*, 130-148.
- Di Lorenzo, E., & Mantua, N. (2016). Multi-year persistence of the 2014/15 North Pacific marine heatwave. *Nature Climate Change*, *6*(11), 1042-1047. <https://doi.org/10.1038/nclimate3082>
- Di Lorenzo, E., Schneider, N., Cobb, K. M., Franks, P. J. S., Chhak, K., Miller, A. J., McWilliams, J. C., Bograd, S. J., Arango, H., Curchitser, E., Powell, T. M., & Rivière, P. (2008). North Pacific Gyre Oscillation links ocean climate and ecosystem change. *Geophysical Research Letters*, *35*(8). <https://doi.org/10.1029/2007gl032838>

- Jacobson, L. D., & MacCall, A. D. (1995). Erratum: Stock-recruitment models for Pacific sardine (*Sardinops sagax*). *Canadian Journal of Fisheries and Aquatic Sciences*, 52(9), 2062-2062. <https://doi.org/10.1139/f95-799>
- Jacobson, L. D., & MacCall, A. D. (1995). Stock-recruitment models for Pacific sardine (*Sardinops sagax*). *Canadian Journal of Fisheries and Aquatic Sciences*, 52(3), 566-577. <https://doi.org/10.1139/f95-057>
- Lindegren, M., & Checkley, D. M. (2012). Temperature dependence of Pacific sardine (*Sardinops sagax*) recruitment in the California Current Ecosystem revisited and revised. *Canadian Journal of Fisheries and Aquatic Sciences*, 70(2), 245-252. <https://doi.org/10.1139/cjfas-2012-0211>
- Litzow, M. A., Hunsicker, M. E., Bond, N. A., Burke, B. J., Cunningham, C. J., Gosselin, J. L., Norton, E. L., Ward, E. J., & Zador, S. G. (2020). The changing physical and ecological meanings of North Pacific Ocean climate indices. *Proceedings of the National Academy of Sciences*, 117(14), 7665-7671. <https://doi.org/10.1073/pnas.1921266117>
- Litzow, M. A., Malick, M. J., Bond, N. A., Cunningham, C. J., Gosselin, J. L., & Ward, E. J. (2020). Quantifying a Novel Climate Through Changes in PDO-Climate and PDO-Salmon Relationships. *Geophysical Research Letters*, 47(16), e2020GL087972. <https://doi.org/10.1029/2020gl087972>
- Lynn, R. J., & Bograd, S. J. (2002). Dynamic evolution of the 1997–1999 El Niño–La Niña cycle in the southern California Current System. *Progress in Oceanography*, 54(1), 59-75. [https://doi.org/10.1016/S0079-6611\(02\)00043-5](https://doi.org/10.1016/S0079-6611(02)00043-5)
- Mantua, N. J., Hare, S. R., Zhang, Y., Wallace, J. M., & Francis, R. C. (1997). A Pacific Interdecadal Climate Oscillation with Impacts on Salmon Production. *Bulletin of the American Meteorological Society*, 78(6), 1069-1080. [https://doi.org/10.1175/1520-0477\(1997\)078<1069:apicow>2.0.co;2](https://doi.org/10.1175/1520-0477(1997)078<1069:apicow>2.0.co;2)
- McClatchie, S. (2012). Sardine biomass is poorly correlated with the Pacific Decadal Oscillation off California. *Geophysical Research Letters*, 39(13). <https://doi.org/10.1029/2012GL052140>
- McClatchie, S. (2014a). The CalCOFI Sampling Domain. In *Regional Fisheries Oceanography of the California Current System: The CalCOFI program* (pp. 8-11). Springer Netherlands.
- McClatchie, S. (2014b). Oceanography of the Southern California Current System Relevant to Fisheries. In *Regional Fisheries Oceanography of the California Current System: The CalCOFI program* (pp. 13-60). Springer Netherlands. https://doi.org/10.1007/978-94-007-7223-6_2
- McClatchie, S., Hendy, I. L., Thompson, A. R., & Watson, W. (2017). Collapse and recovery of forage fish populations prior to commercial exploitation. *Geophysical Research Letters*, 44(4), 1877-1885. <https://doi.org/10.1002/2016GL071751>
- Muhling, B. A., Brodie, S., Smith, J. A., Tommasi, D., Gaitan, C. F., Hazen, E. L., Jacox, M. G., Auth, T. D., & Brodeur, R. D. (2020). Predictability of Species Distributions Deteriorates Under Novel Environmental Conditions in the California Current System. *Frontiers in Marine Science*. <https://doi.org/10.3389/fmars.2020.00589>
- Roemmich, D., & Gilson, J. (2009). The 2004–2008 mean and annual cycle of temperature, salinity, and steric height in the global ocean from the Argo Program. *Progress in Oceanography*, 82(2), 81-100. <https://doi.org/10.1016/j.pocean.2009.03.004>

- Rudnick, D. L. (2016). *California Underwater Glider Network* [data set].
<https://doi.org/10.21238/S8SPRAY1618>
- Rudnick, D. L., Sherman, J. T., & Wu, A. P. (2018). Depth-Average Velocity from Spray Underwater Gliders. *Journal of Atmospheric and Oceanic Technology*, 35(8), 1665-1673.
<https://doi.org/10.1175/JTECH-D-17-0200.1>
- Rudnick, D. L., Zaba, K. D., Todd, R. E., & Davis, R. E. (2017a). A climatology of the California Current System from a network of underwater gliders. *Progress in Oceanography*, 154, 64-106.
<https://doi.org/10.1016/j.pocean.2017.03.002>
- Rudnick, D. L., Zaba, K. D., Todd, R. E., & Davis, R. E. (2017b). *A climatology using data from the California Underwater Glider Network*. <https://doi.org/10.21238/S8SPRAY7292>
- Schroeder, I. D., Santora, J. A., Bograd, S. J., Hazen, E. L., Sakuma, K. M., Moore, A. M., Edwards, C. A., Wells, B. K., & Field, J. C. (2019). Source water variability as a driver of rockfish recruitment in the California Current Ecosystem: implications for climate change and fisheries management. *Canadian Journal of Fisheries and Aquatic Sciences*, 76(6), 950-960.
<https://doi.org/10.1139/cjfas-2017-0480>
- Talley, L. D., Pickard, G. L., Emery, W. J., & Swift, J. H. (2011). *Descriptive Physical Oceanography: An Introduction* (6 ed.). Elsevier.
- Thompson, A. R., Schroeder, I. D., Bograd, S. J., Hazen, E. L., Jacox, M. G., Leising, A., Wells, B. K., Fisher, J., Jacobson, K., Zeman, S., Bjorkstedt, E., Robertson, R. R., Kahru, M., Goericke, R., Peabody, C. E., Baumgartner, T., Lavaniegos, B. E., Miranda, L. E., Gomez-Ocampo, E., Gomez-Valdes, J., Auth, T., Daly, E. A., Morgan, C. A., Burke, B. J., Field, J. C., Sakuma, K. M., Weber, E. D., Watson, W., Porquez, J. M., Dolliver, J., Lyons, D., Orben, R. A., Zamon, J. E., Warzybok, P., Jahncke, J., Santora, J. A., Thompson, S. A., Hoover, B., Sydeman, W., & Melin, S. R. (2019). State of the California Current 2018-19: a Novel Anchovy Regime and a New Marine Heat Wave? *CalCOFI Reports*, 60, 1-61.
- Thompson, A. R., Schroeder, I. D., Bograd, S. J., Hazen, E. L., Jacox, M. G., Leising, A., Wells, B. K., Largier, J., Fisher, J., Bjorkstedt, E., Robertson, R. R., Chavez, F. P., Kahru, M., Goericke, R., McClatchie, S., Peabody, C. E., Baumgartner, T., Lavaniegos, B. E., Gomez-Valdes, J., Brodeur, R. D., Daly, E. A., Morgan, C. A., Auth, T. D., Burke, B. J., Field, J. C., Sakuma, K. M., Weber, E. D., Watson, W., Coates, J., Schoenbaum, R., Rogers-Bennett, L., Suryan, R. M., Dolliver, J., Loreda, S., Zamon, J. E., Schneider, S. R., Golightly, R. T., Warzybok, P., Jahncke, J., Santora, J. A., Thompson, S. A., Sydeman, W., & Melin, S. R. (2018). State of the California Current 2017-18: Still not quite normal in the North and getting interesting in the South. *CalCOFI Reports*, 59, 1-66.
- Zaba, K. D., & Rudnick, D. L. (2016). The 2014–2015 warming anomaly in the Southern California Current System observed by underwater gliders. *Geophysical Research Letters*, 43(3), 1241-1248. <https://doi.org/10.1002/2015gl067550>
- Zaba, K. D., Rudnick, D. L., Cornuelle, B., Gopalakrishnan, G., & Mazloff, M. (2020). Volume and heat budgets in the coastal California Current System: Means, annual cycles and interannual anomalies of 2014-2016. *Journal of Physical Oceanography*, 50(5), 1435-1453.
<https://doi.org/10.1175/jpo-d-19-0271.1>

- Zaba, K. D., Rudnick, D. L., Cornuelle, B. D., Gopalakrishnan, G., & Mazloff, M. R. (2018). Annual and Interannual Variability in the California Current System: Comparison of an Ocean State Estimate with a Network of Underwater Gliders. *Journal of Physical Oceanography*, 48(12), 2965-2988. <https://doi.org/10.1175/jpo-d-18-0037.1>
- Zwolinski, J. P., & Demer, D. A. (2019). Re-evaluation of the environmental dependence of Pacific sardine recruitment. *Fisheries Research*, 216, 120-125. <https://doi.org/10.1016/j.fishres.2019.03.022>
- Zwolinski, J. P., Demer, D. A., Macewicz, B. J., Mau, S., Murfin, D., Palance, D., Renfree, J. S., Sessions, T. S., & Stierhoff, K. L. (2017). *Distribution, biomass and demography of the central-stock of Northern Anchovy during summer 2016, estimated from acoustic-trawl sampling* (NOAA-TM-NMFS-SWFSC-572).
- Zwolinski, J. P., Stierhoff, K. L., & Demer, D. A. (2019). *Distribution, biomass, and demography of coastal pelagic fishes in the California Current Ecosystem during summer 2017 based on acoustic-trawl sampling* (NMFS-SWFSC-610).

Abstract

Though subthermocline eddies (STEs) have often been observed in the world oceans, characteristics of STEs such as their patterns of generation and propagation are less understood. Here, the across-shore propagation of STEs in the California Current System (CCS) is observed and described using 13 years of sustained coastal glider measurements on three glider transect lines off central and southern California as part of the California Underwater Glider Network (CUGN). The across-shore propagation speed of anticyclonic STEs is estimated as $1.35\text{-}1.49 \pm 0.33 \text{ cm s}^{-1}$ over the three transects, Line 66.7, Line 80.0, and Line 90.0, close to the westward long first baroclinic Rossby wave speed in the region. Anticyclonic STEs are found with high salinity, high temperature, and low dissolved oxygen anomalies in their cores, consistent with transporting California Undercurrent water from the coast to offshore. Comparisons to satellite sea-level anomaly indicate that STEs are only weakly correlated to a sea surface height expression. The observations suggest that STEs are important for the salt balance and mixing of water masses across-shore in the CCS.

Introduction

At least as early as the 1970s with the Arctic Ice Dynamics Joint Experiment (AIDJEX) in 1975-1976 (Hunkins, 1974; Manley & Hunkins, 1985) and the POLYMODE experiment in the late 1970s (Robinson, 1983), researchers observed eddies with their strongest signature below the surface mixed layer. The features, here referred to as subthermocline eddies (STEs), are often sampled by global ocean observing systems such as Argo and regionally with ships, gliders, moorings, and floats. While these eddies have been sampled for decades, characteristics of the eddies such as their lifetimes or patterns of generation and propagation are less understood because of the difficulty in observing the subsurface ocean over large spatial scales for long periods of time. Here, the across-shore propagation of eddies below the surface mixed layer from the coast in the California Current System (CCS) is observed and described with 3-km across-shore spatial-resolution subsurface observations from gliders spanning

hundreds of kilometers and 13 years. We seek to characterize properties of STEs, with a specific focus on the across-shore propagation of eddies in the Central and Southern CCS. Evidence is presented of consistent offshore propagation based on observations, and it is suggested that the subsurface eddy flux is an important component of the across-shore salt balance.

In this paper, eddies below the surface mixed layer are called STEs, consistent with recent studies off the U.S. West Coast in Washington state (Pelland et al., 2013; Steinberg et al., 2019). Puddy (Frenger et al., 2018) and cuddy (Garfield et al., 1999) are alternative names used in the region. Historically, STEs have been described by subsurface anomalies in salinity and temperature (Dugan et al., 1982; McDowell & Rossby, 1978). McDowell and Rossby (1978) initially discovered the STE which they named a meddy for “Mediterranean eddy” through examining an extremely warm feature in the temperature field below 700 m from an XBT survey over the Hatteras abyssal plain off the Bahamas. The trajectories of SOFAR floats put into the meddy suggested a compact structure and a southwest direction of translation. Based on the temperature and salinity of the eddy core, McDowell and Rossby (1978) suggested that the eddy originated in the eastern Atlantic from Mediterranean water. Submesoscale STEs have separately been described as submesoscale, coherent vortices (SCVs) (McWilliams, 1985). It is generally accepted that STEs can be identified by a subsurface anomaly in temperature or salinity and that STEs can be long-lived, with anticyclonic STEs existing for years and carrying a water mass from their point of generation in their core (Armi et al., 1989; McWilliams, 1985).

As in other ocean regions, STEs have been observed opportunistically in the CCS (Chereskin et al., 2000; Cornuelle et al., 2000; Davis et al., 2008; Huyer et al., 1998; Koblinsky et al., 1984; Simpson et al., 1984). In addition, there have been long-term observations of STEs with floats and gliders which have begun to describe characteristics of STEs such as their patterns of generation and propagation. Glider onshore-offshore transects from 2002-2008 over the Washington continental slope in the northern CCS identified 20 distinct anticyclonic STEs and 10 distinct cyclonic STEs (Pelland et al., 2013). The available salt anomaly was estimated from averaging observed eddies in the region to create a mean anticyclonic STE, and the generation of 5 eddies a year represented 29% of the annual loss of salt by the

California Undercurrent in that region. Translational speeds of anticyclonic STEs varied from 0.002-0.062 m s⁻¹ and were found in all directions, though the mean translational speed was 0.018 m s⁻¹ in the southwest direction (Pelland et al., 2013). From 1992-2011, RAFOS floats were seeded in the California Undercurrent in the Central CCS (Collins et al., 2013) and a number of floats were observed to separate from the undercurrent and exhibit looping behavior. The anticyclonically looping floats had a median translation speed of 1.9 cm s⁻¹ and usually propagated normal to the coastline (Collins et al., 2013). Ivanov et al. (2008) studied subsurface western motion using 68 isobaric RAFOS float trajectories from 1992-2007 in the same dataset and concluded that the motion was consistent with inhomogeneous eddy diffusion. In this study, the offshore propagation of STEs in the CCS is studied along three regularly sampled glider lines from 2007-2019 in the central and southern CCS. We analyze over twice as many years of glider observations as the northern CCS study (Pelland et al., 2013) and provide temperature and salinity information in the top 500 m, complementing the Lagrangian RAFOS float studies. We aim to directly observe STEs propagating from the coast to offshore with water properties of the coastal California Undercurrent and to better approximate the STE across-shore propagation speed.

The most basic STE identification method is a water mass anomaly along an isopycnal, a method employed by McDowell and Rossby (1978). For the purposes of this paper, an eddy is defined as a salinity anomaly along an isopycnal that propagates horizontally. We make the distinction between eddies and waves by analyzing anomalies on isopycnals. For example, a linear Rossby wave will produce a salinity anomaly at constant depth by heaving of isopycnals but would not cause salinity anomalies on the isopycnal to move horizontally. This paper focuses on the observed speed of STE propagation. A proposed theoretical speed of isolated vortices is the long Rossby wave speed for the vertical mode of the feature (Flierl, 1977; McWilliams & Flierl, 1979). STEs propagate west due to the β -effect, but could also be advected by local currents, potentially important near coastal boundaries (Cushman-Roisin & Beckers, 2011). In the CCS, the main generation mechanism of STEs is the separation of the undercurrent from the coast due to flow past a topographic feature. For a poleward undercurrent in an EBUS, interaction of the poleward flow past the coastline generates anticyclonic relative vorticity which

causes eddies formed from the separation process to be anticyclonic (D'Asaro, 1988; Molemaker et al., 2015).

The CCS is an eastern boundary current system where westward is roughly equivalent to the across-shore direction. STEs in the CCS may transport tracers offshore due to a tendency for westward propagation after formation. Anticyclonic STEs have been observed to encapsulate fluid with a distinct water mass signature and carry that water thousands of miles from its source (Lukas & Santiago-Mandujano, 2001; McDowell & Rossby, 1978). In the CCS, the poleward flowing California Undercurrent has a distinct water mass which is warmer, saltier, and lower in dissolved oxygen than the water in the equatorward flowing California Current (Bograd et al., 2019). STEs may be important in the transport of tracers including heat, salt, and biogeochemical properties such as dissolved oxygen, nutrients, and pH (Frenger et al., 2018). Here we focus on salinity with some comments on dissolved oxygen.

Data and Methods

Data were collected as part of the California Underwater Glider Network (CUGN), which is a network of underwater gliders that continuously samples three lines: Line 90.0 off Dana Point, Line 80.0 off Point Conception, and Line 66.7 off Monterey Bay (Fig. 2.1). Lines are in the geometry of the California Cooperative Fisheries Investigations (CalCOFI) hydrographic survey, in operation since 1949 (McClatchie, 2014). An underwater glider is a buoyancy-driven autonomous vehicle that generates profiles of variables such as temperature and salinity as it completes a sawtooth pattern of dives (Rudnick et al., 2004). For this study, we use Spray underwater gliders diving to 500 m and traveling at about 0.25 m s^{-1} so that it takes 2-3 weeks to complete one transect along a line of 350-500 km length. Individual gliders are recovered after roughly 100 days at sea at which point a glider has completed its mission. As one glider is recovered, another glider is deployed such that there is continuous data coverage. The annual glider occupation on transects approaches 100% from 2009-2019 (Fig. 1b). The horizontal distance between each glider profile is around 3 km, and the time between successive profiles is around 3 hours. In a typical year, gliders collect around 3,000 profiles on a line.

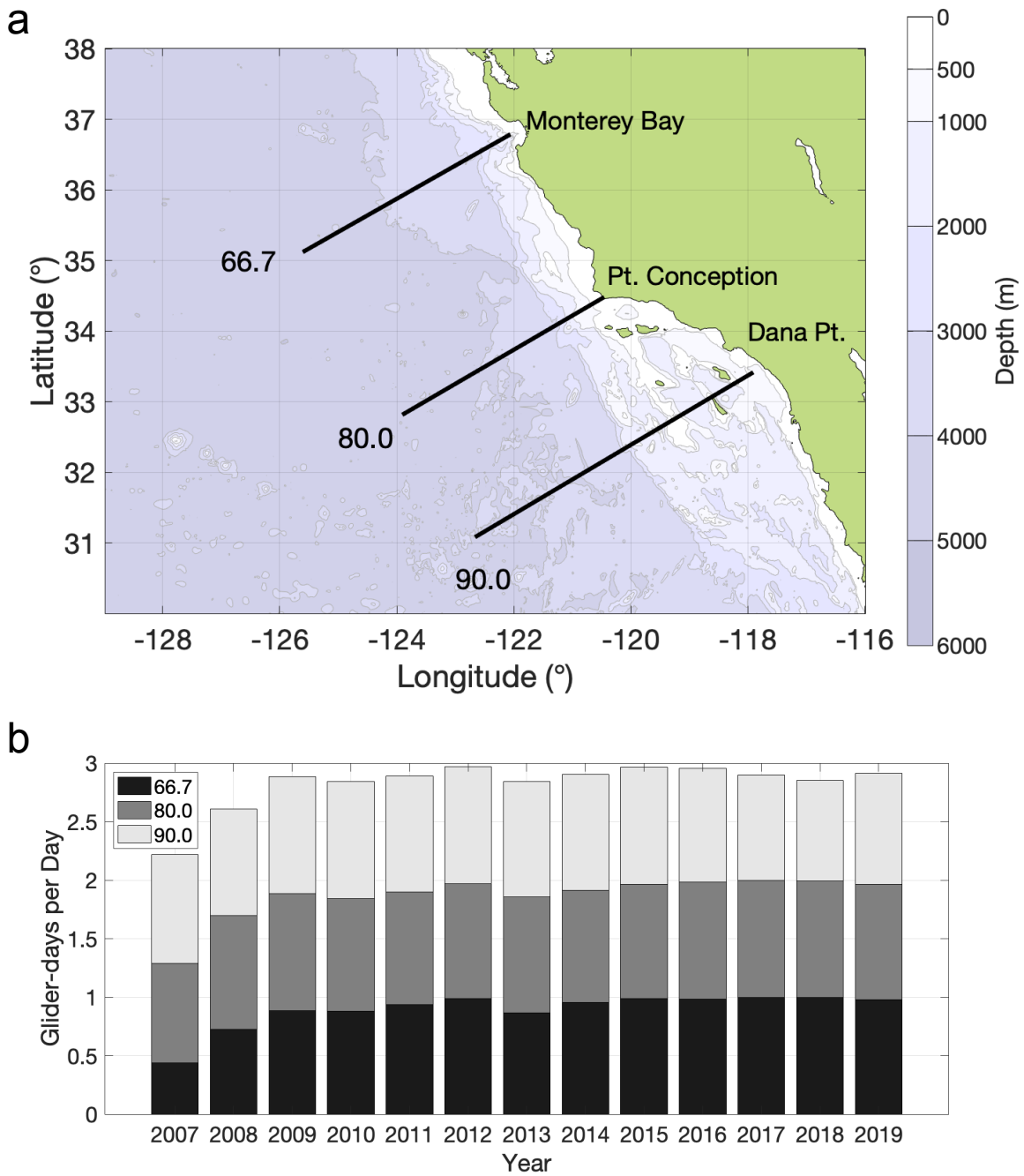


Figure 2.1 (a) The central and southern California Current System domain monitored by CUGN. Glider lines 66.7, 80.0, and 90.0 are plotted in black. The coastal bathymetry is plotted in color contours. (b) The coverage of the three glider lines 66.7, 80.0, and 90.0 plotted as the ratio of glider days per day. One glider day per day is equivalent to one line having glider observations for the full year. The maximum value for the Lines 66.7, 80.0, and 90.0 is three.

The CUGN glider data are averaged vertically into bins at 10 m intervals centered at 10 m, 20 m, and so on to 500 m depth in what will be heretofore called profile data (Rudnick, 2016). We use a published climatology of the CUGN data that includes the annual cycle and anomalies of measured variables (Rudnick et al., 2017a, 2017b). The annual cycle is calculated from full years 2007-2013 on Lines 80.0 and 90.0 and 2008-2013 for Line 66.7 using one constant and three harmonics. In calculating the annual cycle, a Gaussian weighting function is used to emphasize observations closest to the grid point on the transect. Anomalies from the annual cycle are objectively mapped using a decorrelation length scale of 30 km and time scale of 60 days. 30 km is the wavelength where the slope of the spectrum of temperature at 100 m changes, indicating contamination of data at higher wavenumbers by internal waves (Rudnick & Cole, 2011; Rudnick et al., 2017a), and 60 days is the e-folding timescale of the autocorrelation function of the temperature anomalies (Rudnick et al., 2017a). A standard way to assess the quality of an objective map is to consider the ratio of the mean square error in the map versus the mean square error of the mapped variable, a ratio of error to signal variance (Bretherton et al., 1976). Areas of the objective map where the ratio is larger than 0.3 are masked out. The choice of 0.3 is roughly when the map error's standard deviation is half the value of the standard deviation of the signal and serves to remove suspect points at the edges of the map or near areas of missing data. The climatology grid is 10 days in time, 5 km in horizontal distance, and 10 m in depth. Profile data and climatology data of salinity and temperature used here are from 2007 to the end of 2019. Calibrated dissolved oxygen profile data are from December 2016 until the end of 2019. Geostrophic velocity is calculated by obtaining the vertical shear using the thermal wind relationship and referencing the vertical shear to the depth-averaged velocity as measured by the gliders (Rudnick et al., 2018) to get the absolute geostrophic velocity. The geostrophic velocity is calculated for the full map and the for the mean annual cycle, and the geostrophic velocity anomaly is found from subtracting the two.

Satellite sea level anomaly (SLA) data were used to analyze the surface expression of STEs. Reprocessed, L4, SLA data of 0.25 x 0.25 degree spatial resolution from the global resolution Data Unification and Altimeter Combination System (DUACS) product was downloaded from the Copernicus

Marine Service. The data product was created from optimal interpolation using 10 available satellite missions since 1993 (Pujol et al., 2016). The SLA is the deviation from the mean sea level as measured from the 20-year period 1993-2012, and the zonal correlation scale of the product in the southern CCS is 125-150 km (Pujol et al., 2016). SLA was interpolated to the locations of glider profiles using trilinear interpolation. Due to issues with satellite signal contamination and errors near the coast (Saraceno et al., 2008), the inshore 56 km was not included in any calculations using the SLA.

Joint probability density function (PDF) analysis was used to examine the co-occurrence of property anomalies in variables such as salinity and stratification. The joint probability density function is defined (Bendat & Piersol, 2011) as

$$p_{X,Y}(x, y) = \lim_{\substack{\Delta x \rightarrow 0, \\ \Delta y \rightarrow 0}} \frac{\mathbf{Prob}[x < X < x + \Delta x \text{ and } y < Y < y + \Delta y]}{\Delta x \Delta y}. \quad (1)$$

Specifically, $p_{X,Y}(x, y) \Delta x \Delta y$ is the probability that the random variable X is between the values of x and $x + \Delta x$ and that the random variable Y is between the values of the y and $y + \Delta y$. The corresponding integral relation is

$$\int_{-\infty}^{\infty} \int_{-\infty}^{\infty} p_{X,Y}(x, y) dx dy = 1. \quad (2)$$

Joint PDFs can describe whether two random variables are statistically dependent or independent of each other. The two variables X and Y are independent if the joint PDF is equal to the product of the PDFs of X and Y ,

$$p_{X,Y}(x, y) = p_X(x)p_Y(y). \quad (3)$$

Graphically, dependence is demonstrated when there is tilt in the pattern of the joint PDF relative to the x - y axes.

Autocorrelation in space and time was calculated using the CUGN climatology salinity anomaly data product on isopycnal surfaces, thus filtering out the effects of the annual cycle. To isolate propagating signals, the spatial mean at every time was removed from the CUGN anomalies.

Autocorrelation lags were calculated in 5-km and 10-day increments, which correspond to the resolution

of the climatology. For each lag in space and time, the mean of the corresponding salinity anomaly pairs was calculated and normalized by the square root of the respective variances following the formula,

$$\rho = \frac{\langle X'(x, t)X'(x + n\Delta x, t + m\Delta t) \rangle}{\sqrt{\langle X'(x, t)^2 \rangle \langle X'(x + n\Delta x, t + m\Delta t)^2 \rangle}} \quad (4)$$

where primes are deviations from the mean and angle brackets denote the mean. X' here is the salinity anomaly from CUGN with spatial mean removed, x represents distance from shore, and t represents time. The lags in distance and time are defined by $\Delta x = 5$ km and $\Delta t = 10$ days and with n and m integer values for the number of lags separating the values of X' .

To estimate a speed of propagation, a fitting procedure was applied to the autocorrelation map. A Gaussian was chosen to fit the positive autocorrelation pattern found near zero lag that decays with greater lags in space and time, similar to Kuragano and Kamachi (2000). A 2-dimensional Gaussian with variable length scales in two directions, L_x and L_{ct} , and a rotation, θ , was used:

$$G(x, ct) = e^{-\left[\left(\frac{x \cos \theta - ct \sin \theta}{L_x}\right)^2 + \left(\frac{x \sin \theta + ct \cos \theta}{L_{ct}}\right)^2\right]} \quad (5)$$

The constant, c , assures unit consistency and here $c = 1$ km day⁻¹. The length scale for time is scaled by c so that

$$L_{ct} = c L_t, \quad (6)$$

where L_t is the length scale for time in days. The rotation angle of the best-fit Gaussian can be used to determine a propagation speed. The cotangent of the rotation angle is the ratio of the lags in space over the lags in scaled time preferred in the autocorrelation map. The propagation speed of the salinity anomalies offshore on the line was calculated by

$$u_L = c \cot \theta \quad (7)$$

where u_L is the across-shore speed in km day⁻¹. Following simple unit conversion, u_L is reported in m s⁻¹. The fit was performed on each 0.1 kg m⁻³ potential density layer from σ_θ 25.8 to 26.7 kg m⁻³ as well as on the average autocorrelation map of the 10 potential density levels. The fit included data from within 100-km and 100-day lags, which was the window within which the central features of the autocorrelation

maps were found. The propagation speed from the autocorrelation map of the average of the potential density layers σ_θ 25.8-26.7 kg m⁻³ was reported. The standard deviation of the propagation speeds from each of the 10 potential density layers was reported as the error. Propagation speeds and standard deviations were calculated on each Line 66.7, 80.0, and 90.0.

To compare westward salinity anomaly propagation speeds to the expected linear Rossby wave speed, the baroclinic mode Rossby wave speeds were calculated using density profiles obtained from salinity and temperature of the World Ocean Atlas (WOA) 2018. The Rossby wave dispersion relation is

$$\omega = \frac{-\beta k}{k^2 + l^2 + \frac{f_0^2}{c_n^2}}, \quad (8)$$

and the horizontal phase speed of the Rossby wave, c_p , is

$$c_p = \frac{-\beta}{k^2 + l^2 + \frac{f_0^2}{c_n^2}}. \quad (9)$$

ω is the angular frequency of the wave, β is the gradient of the Coriolis parameter with respect to latitude, k is the horizontal wavenumber in the x-direction, l is the horizontal wavenumber in the y-direction, f_0 is the local Coriolis parameter, and c_n is the nth eigenvalue solution of the Sturm-Liouville eigenvalue problem for the vertical structure $\varphi(z)$ of the vertical velocity (Gill, 1982). c_n has the dimensions of velocity, and in c_n the subscript $n=1,2,\dots$ corresponds to the nth baroclinic mode solution. The nth baroclinic Rossby radius of deformation, R_d , is $\frac{c_n}{f_0}$. Profiles of the buoyancy frequency squared, $N^2(z)$, were calculated using climatological temperature and salinity from WOA 2018. The eigenvalues c_n for the baroclinic modes were obtained by solving the Sturm-Liouville equation numerically. The Rossby waves are assumed to be of long wavelength. From observations in the CCS, Rossby waves with wavenumbers on the order of 10^{-6} m^{-1} (Todd et al., 2011) have been observed, and the inverse Rossby radius of deformation is on the order of 10^{-5} m^{-1} . The phase speed, c_p , is approximated as

$$c_p = -\beta \frac{c_n^2}{f_0^2}. \quad (10)$$

The phase speed, c_p , is defined for purely westward propagation. The transect lines on which the CUGN gliders observe propagation are at an angle, α , south of west. The measured Rossby wave propagation speed along the transects, u_R , is expected to be faster based on the secant of α ,

$$u_R = c_p \sec(\alpha). \quad (11)$$

The relationship is based on simple trigonometry arguments and the nature of wave phase propagation (Gill, 1982). The value for α is 25° for Line 66.7 and 26° for Lines 80.0 and 90.0.

Results

Individual STEs were identified in glider transects. An example of an anticyclonic STE feature is found in two glider crossings on Line 66.7 in March and April 2017 (Fig. 2.2). Within the core of the identified STE, the temperature and salinity are higher and stratification is reduced. The dome-like structure of the potential density surfaces reflects the stratification anomaly and suggests the geostrophic velocity structure around the feature: northward on the offshore side of the STE and southward on the inshore side. While the SLA is positive in the region of the anticyclonic STE, an isolated vortex feature on the surface corresponding to the subsurface feature is not readily apparent. The STE is on the order of 100 km in diameter. The large size of the feature and its apparent slow movement suggest that the same feature was sampled twice between March and April.

From examination of the CUGN maps of salinity anomaly on isopycnal σ_θ 26.5 kg m^{-3} on Lines 66.7, 80.0, and 90.0 (Fig. 2.3), there is evidence of multiple instances of propagation like that suggested by inspection of the profile data (Fig. 2.2). The Hovmoller diagrams (Fig. 2.3) show streaks of high salinity anomaly that are tilted such that the anomaly moves offshore over time. The propagation stretches from near the coast to 400 km offshore in some instances. The best examples of offshore propagation of salinity anomalies are on Line 66.7. More propagation patterns appeared on Line 66.7 after 2014 as opposed to in the first half of the record. The propagation patterns are least apparent on Line 90.0, the most southern line. One contributing factor to this result may be that the glider data

capture the STEs whose offshore propagation is in the direction of the transect. STEs with angles of propagation that differ

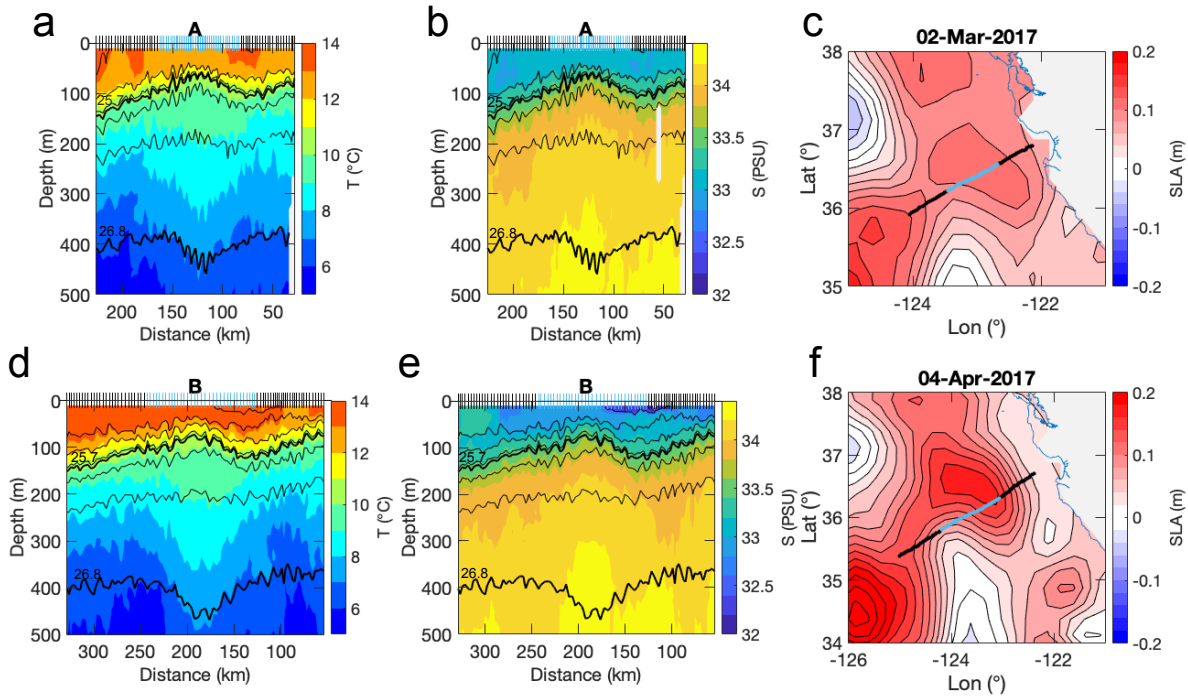


Figure 2.2 Two glider transects in March and April 2017 that crossed a STE. a) and d) the temperature of transects A and B. b) and e) the salinity of transects A and B. c) and f) the SLA of the transects A and B. In a-b and d-e, the potential density surfaces are plotted in thin black lines at increments of 0.4 kg m^{-3} until $\sigma_{\theta} 26.8 \text{ kg m}^{-3}$ while thick black lines mark $\sigma_{\theta} 25.7$ and 26.8 kg m^{-3} . The color contour levels are 1°C , 0.2 PSU , and 0.02 m . The vertical markings in a-b and d-e mark individual dives, while dives identified by inspection to be related to the STE are colored blue. In c and f, the locations of dives are plotted over the SLA, with the location of the STE marked with blue dots. The STE dives (blue dashes or dots) cover 78 km horizontal distance in A and 115 km horizontal distance in B and were sampled over 3.7 and 5.1 days respectively. The satellite SLA data of the day identified by inspection as the midpoint of the STE are plotted. The anticyclonic STE has higher temperature and salinity within its core.

will not be tracked for long and measured speeds along the transect will appear faster (Eq. 11). Another

explanation is that there are greater numbers of STEs generated from Monterey Bay (Line 66.7) than

Point Conception (Line 80.0) or the Southern California Bight (Line 90.0). The interaction of a current

with topographic features has been found to generate STEs (Gula et al., 2019; Gula et al., 2016;

Molemaker et al., 2015), and Point Sur on the Southern tip of Monterey Bay is the location of an undersea

headland which modeling has shown causes a quasi-permanent separation of the undercurrent from the coast in summer (Molemaker et al., 2015). Another factor may be that there are stronger mean coastal alongshore wind speeds in spring off of Monterey Bay and Point Conception than in the Southern California Bight (Hsu et al., 2007). Additionally, the CUGN gliders measure greater variance in alongshore geostrophic velocity throughout the water column, indicative of the eddy kinetic energy, on Line 66.7 than on Line 80.0 or Line 90.0, with Line 90.0 having the lowest variance.

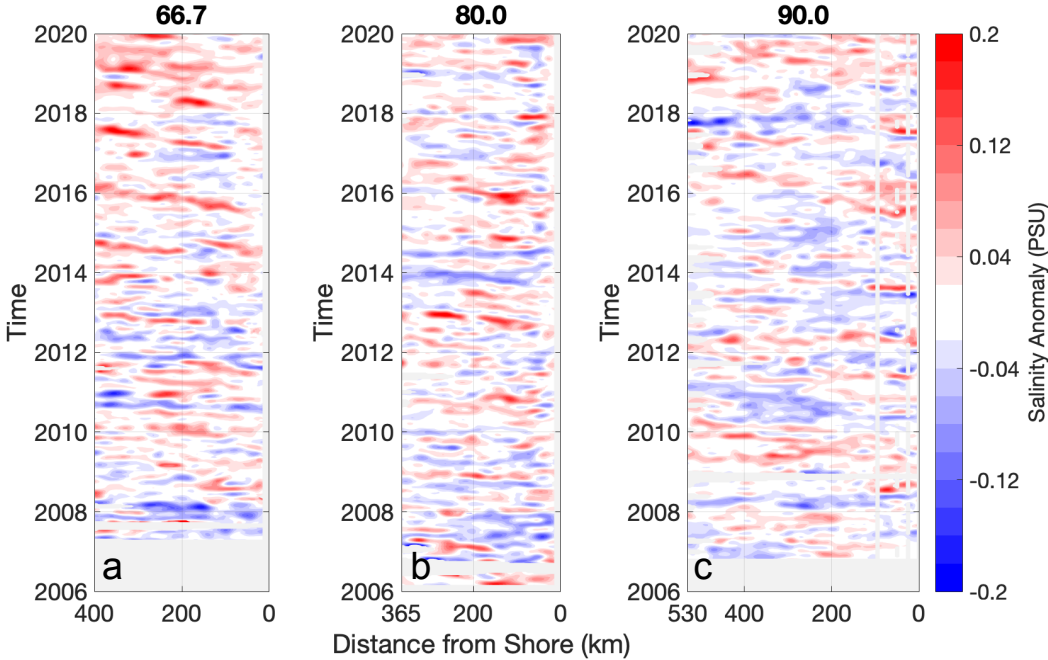


Figure 2.3 Hovmoller diagrams of CUGN climatology salinity anomaly on $\sigma_0 26.5 \text{ kg m}^{-3}$ for a) Line 66.7 b) Line 80.0 and c) Line 90.0. Areas with large map error are masked in grey. Propagation of high salinity anomalies offshore is observed.

Anomalies of geostrophic velocity and potential temperature also propagate offshore, as shown on Line 66.7 for the period between 2014 and the end of 2019 (Fig. 2.4). The potential temperature and salinity anomalies show the same spatial pattern by definition, as the features are plotted on potential density surfaces. Geostrophic velocity anomaly patterns are found which indicate anticyclonic motion around a potential density anomaly. There is a poleward or positive velocity anomaly on the offshore edge and an equatorward or negative velocity anomaly on the inshore edge that envelopes a positive

salinity anomaly. The 2017 STE in Figure 2.2 is labeled at points A and B, where the geostrophic velocity anomaly positive-negative pair pattern is observed to envelop the positive salinity anomaly. Two other examples of STE features found in the profile data are plotted in black dots in Figure 2.4, providing examples of propagation of a positive salinity anomaly offshore with an associated positive-negative pair pattern in geostrophic velocity anomaly.

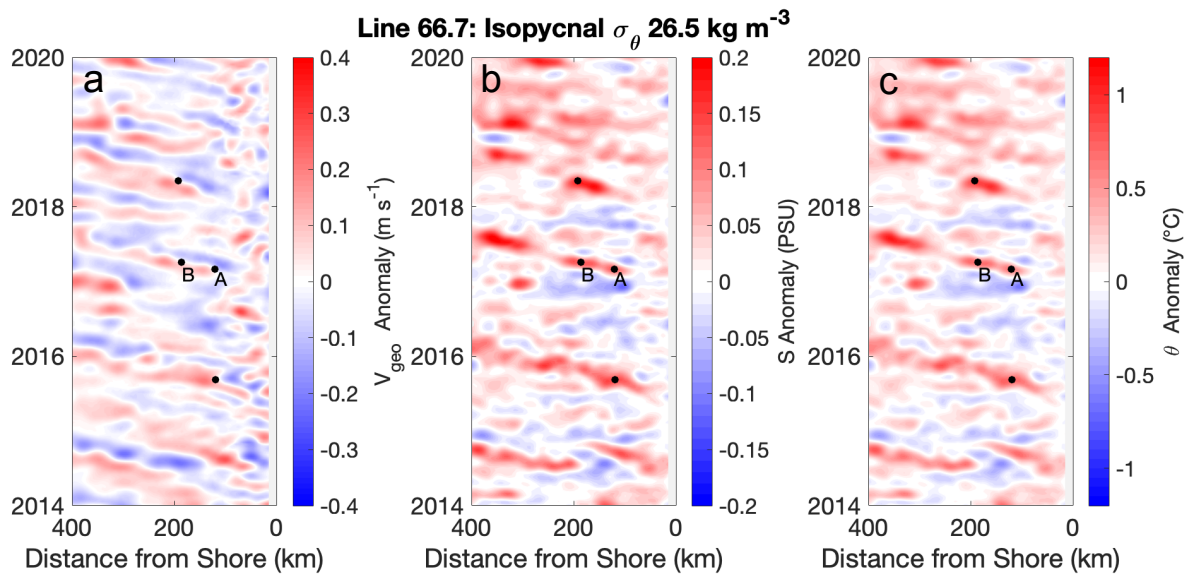


Figure 2.4 Hovmöller diagrams from the CUGN climatology of a) geostrophic velocity anomaly b) salinity anomaly and c) potential temperature anomaly on potential density surface σ_{θ} 26.5 kg m⁻³. STEs identified by inspection of the glider profile data are marked with black dots. The STE found in March and April 2017 is labeled by letters “A” and “B” respectively. Positive potential temperature anomalies and geostrophic velocity anomaly positive-negative pairs are found to propagate offshore with positive salinity anomalies.

The offshore propagation speed of the salinity anomaly along the glider transect is computed for Lines 66.7, 80.0, and 90.0. The speeds are estimated by fitting a 2D Gaussian with tilt to the 2D autocorrelation map of salinity anomaly from the mapped CUGN data, with a spatial mean removed at every time step. See “Methods” for more details. The mean 2D autocorrelation map for salinity anomaly on σ_{θ} 25.8-26.7 kg m⁻³ is plotted for each line (Fig. 2.5). The 2D autocorrelation maps for all three lines demonstrate a tilt in the central positive autocorrelation feature where there is stronger positive

autocorrelation for positive lags in space and time. The spatial variable, defined as the distance from shore, increases as an anomaly moves offshore. As time moves forward, the positive autocorrelation feature describes offshore propagation of salinity anomalies. The estimated propagation speeds with error bounds are plotted in the first quadrant overlying the 2D autocorrelation maps for each Line 66.7, 80.0, and 90.0 (Fig. 2.5). The estimated offshore propagation speed was $1.43 \pm 0.16 \text{ cm s}^{-1}$ on Line 66.7, $1.35 \pm 0.21 \text{ cm s}^{-1}$ on Line 80.0, and $1.49 \pm 0.33 \text{ cm s}^{-1}$ on Line 90.

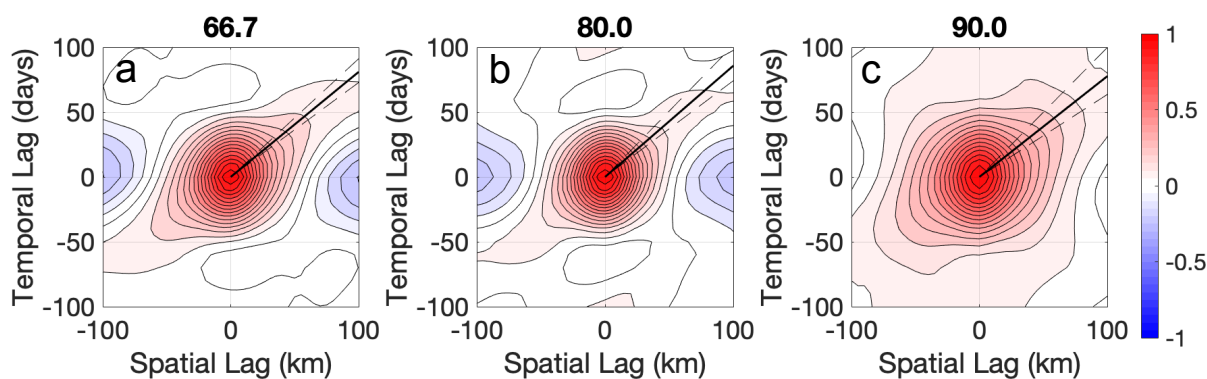


Figure 2.5 Spatial and temporal autocorrelation maps of salinity anomaly on a) Line 66.7 b) Line 80.0 and c) Line 90.0. The estimated propagation speed of salinity anomalies is plotted in solid black lines in the first quadrant. Error bounds are plotted in dashed black lines. The autocorrelation was calculated over the potential density layer $25.8\text{-}26.7 \text{ kg m}^{-3}$. The propagation speeds are $1.43 \pm 0.16 \text{ cm s}^{-1}$, $1.35 \pm 0.21 \text{ cm s}^{-1}$, and $1.49 \pm 0.33 \text{ cm s}^{-1}$ in a), b), and c) respectively.

Water Mass Description of the Anticyclonic STEs

A positive salinity anomaly and reduced stratification appear to be features of the core of the anticyclonic STEs identified in transects (Fig. 2.2). Consider an isopycnal layer below the pycnocline defined between the two isopycnals $\sigma_{\theta} 25.7\text{-}26.8 \text{ kg m}^{-3}$ (Fig. 2.6). Properties of the subthermocline layer are compared using joint PDFs. Layer thickness is used as a proxy for stratification since for a layer defined between isopycnals, changes in its thickness indicate changes in buoyancy frequency. Joint PDFs of layer thickness and salinity on all three Lines 66.7, 80.0, and 90.0 demonstrate that salinity and thickness are dependent with higher thickness (lower stratification) associated with higher salinity (Figs. 2.7a-f). The relationship between stratification and salinity is a significant feature of the subthermocline CCS. The dependence suggests that anticyclonic STEs carry saltier California Undercurrent water from

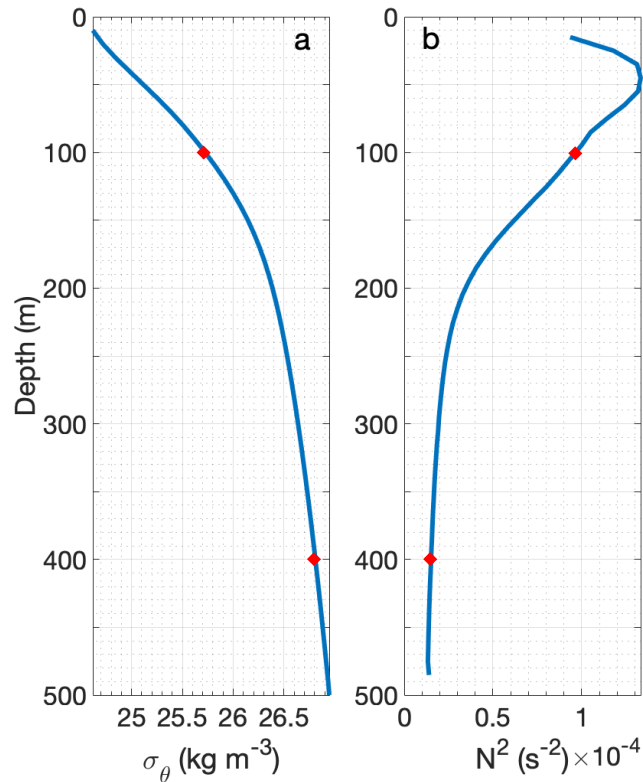


Figure 2.6 The mean profiles across Lines 66.7, 80.0, and 90.0 of a) potential density σ_θ and b) buoyancy frequency N^2 . Red diamonds denote values at 100 m and 400 m, corresponding to σ_θ 25.7 and 26.8 kg m^{-3} .

the coast to offshore. The California Undercurrent itself is present in the joint PDFs (Figs. 2.7a-c) and contributes to the pattern of high thickness associated with high salinity. However, examination of the salinity-thickness relation of profiles greater than 200 km from shore shows that higher thickness (lower stratification) is associated with higher salinity as well (Figs. 2.7d-f).

The results extend to biogeochemical tracers of the California Undercurrent such as dissolved oxygen. The joint PDF of mean layer dissolved oxygen concentration between σ_θ 25.7-26.8 kg m^{-3} and layer thickness demonstrates that dissolved oxygen and thickness are dependent (Fig. 2.8a). Lower dissolved oxygen is associated with higher layer thickness (lower stratification). The joint PDF further confirms that the source of anticyclonic STE water is the California Undercurrent, whose water mass is warmer, saltier, and lower in dissolved oxygen than the surrounding California Current water (Bograd et

al., 2019). Mean layer dissolved oxygen and mean layer salinity are dependent (Fig. 2.8b), consistent with the California Undercurrent water mass relationship between the two. On an isopycnal, high salinity is by definition associated with high potential temperature. Higher temperature and lower-dissolved oxygen have been linked in an empirical model in the CCS to lower pH (Alin et al., 2012), suggesting that the cores of anticyclonic STES are low pH regions as well.

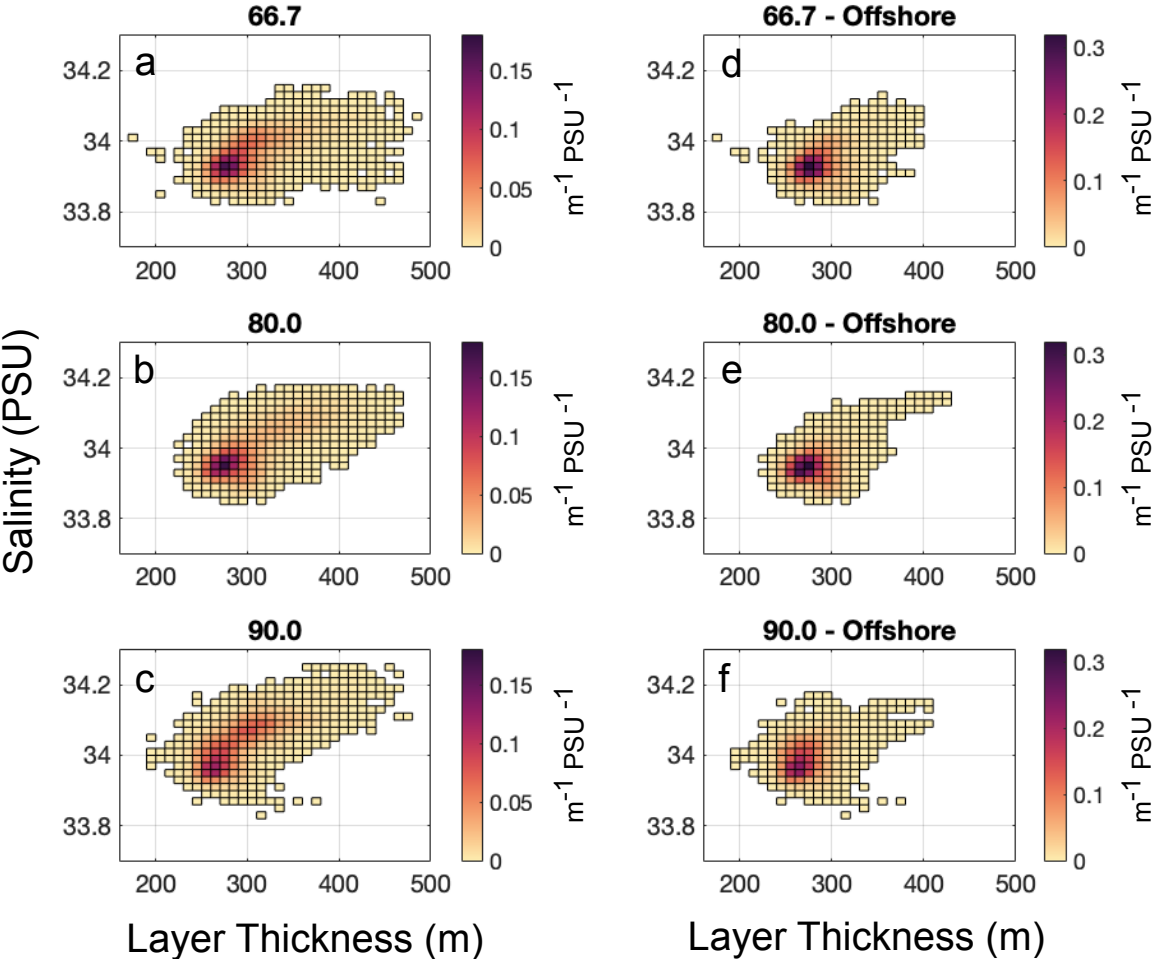


Figure 2.7 Joint PDFs of mean salinity and layer thickness for the potential density layer defined between $\sigma_{\theta} 25.7-26.8 \text{ kg m}^{-3}$. a) Joint PDF for Line 66.7 b) joint PDF for Line 80.0 and c) joint PDF for Line 90.0 using profiles over the whole domain. d) Joint PDF for Line 66.7 e) joint PDF for Line 80.0 and f) joint PDF for Line 90.0 using profiles greater than 200 km from shore. All profiles for which salinity and potential density were defined between $\sigma_{\theta} 25.7-26.8 \text{ kg m}^{-3}$ from 2007-2019 were used in the joint PDFs, with a total of 32,296, 32,359, and 33,101 profiles in a), b), and c) respectively. The shapes of the joint PDFs suggest that mean layer salinity and layer thickness are dependent.

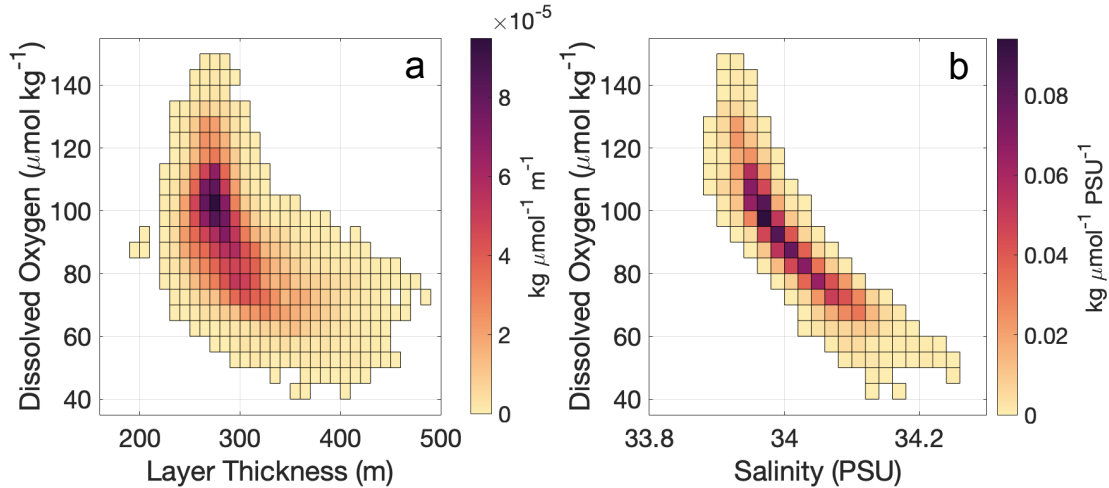


Figure 2.8 Joint PDFs of a) mean dissolved oxygen and layer thickness and b) mean dissolved oxygen and mean salinity for the potential density layer defined between σ_{θ} 25.7-26.8 kg m^{-3} . Glider profiles from all three lines 66.7, 80.0, and 90.0 and from 2016-2019 were used in each plot. The joint PDFs show that mean layer dissolved oxygen and layer thickness are dependent and that mean layer dissolved oxygen and mean layer salinity are dependent.

Surface Expression of STEs

It is an open question whether STEs can be detected via a sea surface height signature (Bashmachnikov et al., 2014; Frenger et al., 2018; Ienna et al., 2014). Here, the joint PDFs of satellite SLA and subthermocline mean salinity and layer thickness between σ_{θ} 25.7-26.8 kg m^{-3} do not suggest a strong relationship (Figs. 2.9a-f). Layer salinity is independent of SLA (Figs. 2.9a-c). Increasing layer thickness corresponding to lower SLA is evident near the areas of highest density in the joint PDFs (Figs. 2.9e-f) suggesting that the two variables are dependent. The correlation or linear relationship between the SLA and layer thickness is very weak but significant with values of -0.2 on Line 90.0 and of magnitude less than 0.1 on Lines 66.7 and 80.0 ($p < 0.05$), suggesting only a weak relationship between the two variables. Supporting the lack of dependence between SLA and subthermocline mean salinity, the satellite SLA field with the annual cycle removed shows westward propagation of SLA (Fig. 2.10), but the surface patterns are not easily matched to the subthermocline salinity anomaly propagation features (Fig. 2.3). Though not a focus of this paper, a dominant signal of the SLA Hovmollers is a climate

variability or global warming signal with higher SLA after 2014 likely related to increased surface ocean temperatures during that period (Ren & Rudnick, 2021).

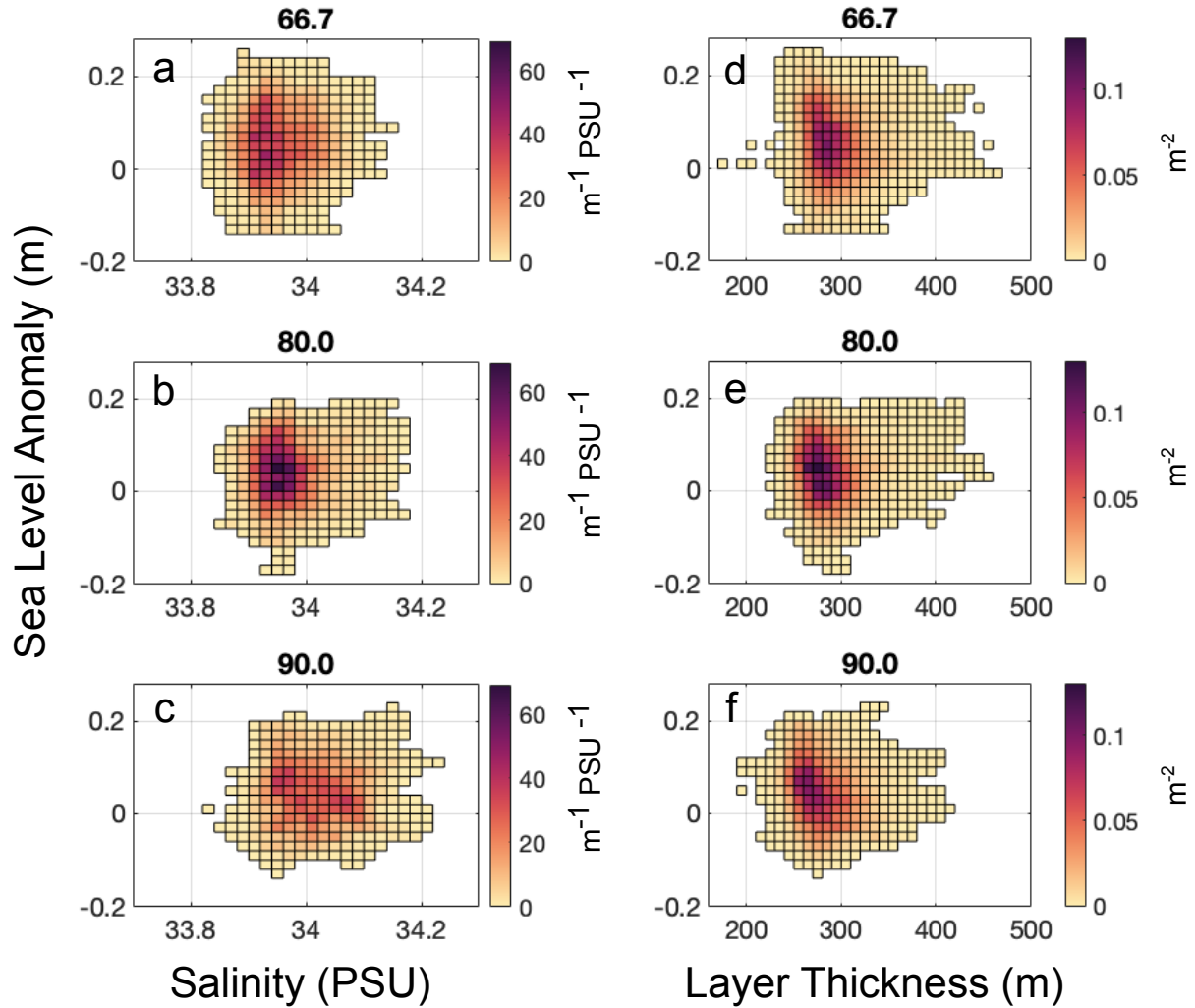


Figure 2.9 Joint PDFs of sea level anomaly compared to characteristics of the potential density layer defined between σ_{θ} 25.7-26.8 kg m^{-3} . Joint PDFs of sea level anomaly and mean layer salinity are plotted for a) Line 66.7 b) Line 80.0 and c) Line 90.0. Joint PDFs of sea level anomaly and layer thickness are plotted for d) Line 66.7 d) Line 80.0 and f) Line 90.0. Data are from 2007-2019.

Discussion and Conclusions

From 13 years of sustained glider measurements in the CCS, characteristics of the across-shore propagation of STEs were studied. Anticyclonic STEs were found to propagate from the coast to offshore. The anticyclonic STEs carried California Undercurrent water in their cores, which is warmer,

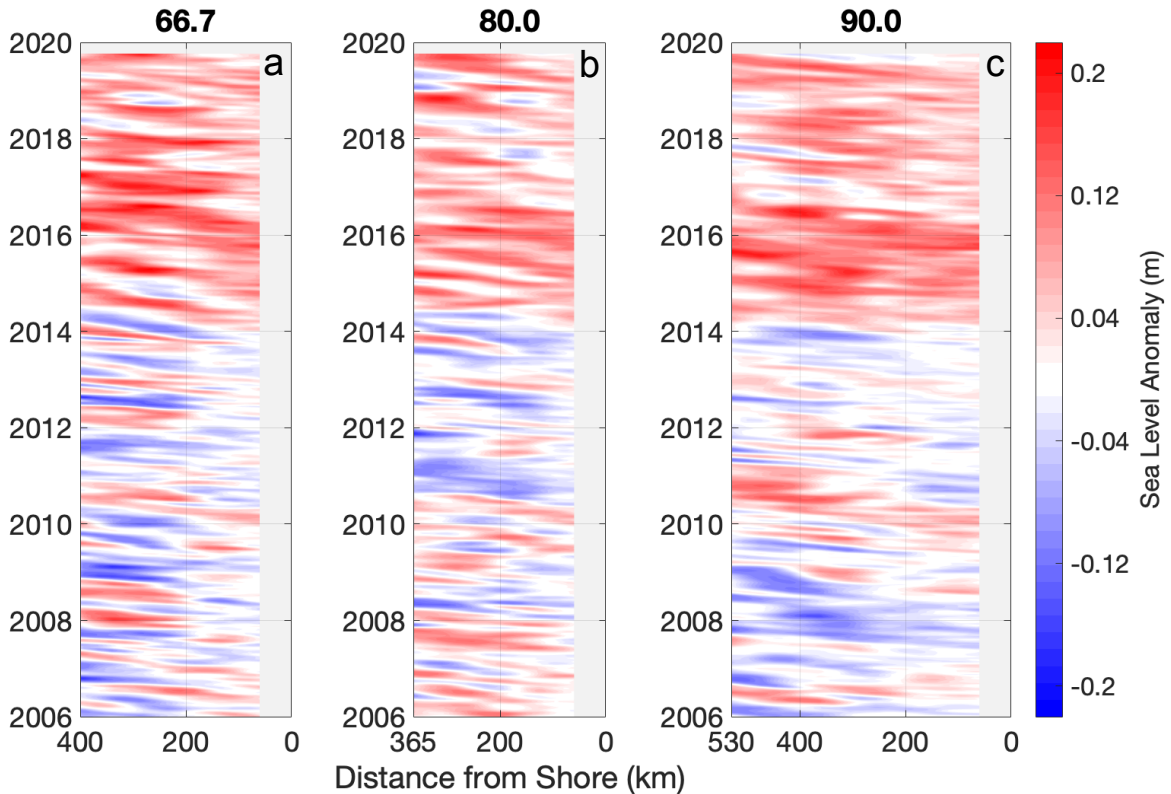


Figure 2.10 Hovmoller diagrams of sea level anomaly on a) Line 66.7 b) Line 80.0 and c) Line 90.0. The coastal inshore 56 km, where the data product is known to have greater errors, is masked in grey. Signals of westward propagation are observed in sea level anomaly.

saltier, and lower in dissolved oxygen than the water of the California Current. The anticyclonic STEs moved at approximately $1.35\text{-}1.49 \pm 0.33 \text{ cm s}^{-1}$ in the offshore direction. A weak surface expression of STEs was found. Though there are westward propagating signals in SLA, they were found to be mostly decoupled from the westward propagation of STEs below the thermocline.

The offshore propagation speed reported here is consistent with previous estimates. In studies using quasi-isobaric RAFOS floats launched at 300 m in the CCS, the median translation speed of anticyclonic eddies was 1.9 cm s^{-1} and the anticyclonic eddies usually moved normal to the coastline (Collins et al., 2013). Analysis of a global 0.1° horizontal resolution model suggested anticyclonic STEs with lifespans of 9 months or greater in the North Pacific moved westward at 2.4 cm s^{-1} (Frenger et al., 2018). The speeds from the CUGN gliders are lower than the model's mean value but agree within error

bounds with the observational value from the floats. Combined results from floats, models, and gliders in the central CCS agree on the offshore propagation of STEs at speeds of about 1-2 cm s⁻¹.

The propagation speed found from tracking salinity anomalies on an isopycnal is compared to the estimated westward speed of baroclinic Rossby waves in the region. Along the three Lines 66.7, 80.0, and 90.0, the estimated baroclinic speeds using WOA climatology temperature and salinity in water depths greater than or equal to 4,000 m were 1.4-1.8 cm s⁻¹ for the first baroclinic mode, 0.4-0.6 cm s⁻¹ for the second baroclinic mode, and 0.2-0.3 cm s⁻¹ for the third baroclinic mode. The range of speeds is a result of minor deviations in stratification or bottom depth from the profiles along each line and are consistent with previous calculations (Chelton et al., 1998). Assuming that a Rossby wave is moving due west, the wave speed along the transects for the first baroclinic mode are 1.5-2.0 cm s⁻¹ and within the reported westward speed range for the higher modes. The first node in vertical displacement for the profile data occurs around 300 m (Fig. 2.2), which matches the structure of the third baroclinic mode in the region. A combination of vertical modes including the third baroclinic mode is likely necessary to explain the westward propagation speed. The observed westward propagation speed of STEs being higher than mode 2 and mode 3 linear wave speeds may be due to the background flow, the non-linear dynamics of eddies, or interactions between the vertical modes (McWilliams & Flierl, 1979). Initial investigation into surface eddies, best represented by the barotropic and first baroclinic mode, suggested that they were Rossby waves with higher than expected westward propagation speeds (Chelton & Schlax, 1996), and subsequent analysis of higher-resolution data suggested that the eddies propagated westward at around the long first baroclinic Rossby wave speed (Chelton et al., 2011; Chelton et al., 2007), matching the theoretical prediction (McWilliams & Flierl, 1979).

This study does not capture every STE in the CCS as it misses STEs that propagate alongshore (Pelland et al., 2013; Steinberg et al., 2019). However, movement of anticyclonic STEs in the offshore direction is important for mixing of California Undercurrent water and California Current water.

Consider an order of magnitude estimate of the divergence of the across-shore eddy salt flux,

$$\langle (u's')_x \rangle \tag{12}$$

where u' is the across-shore velocity anomaly due to the eddies and s' is the eddy salinity anomaly. The angle brackets denote the mean and the subscript x denotes the derivative in the across-shore direction, or along the transect. At 400 km from shore, the across-shore eddy propagation speed is 1.4 cm s^{-1} , and a reasonable eddy salinity anomaly is 0.1 PSU (Fig. 2.2 and Fig. 2.7). Taking u' to be zero at the coast, a rough estimate of the divergence of the across-shore eddy flux is $4 \times 10^{-9} \text{ PSU s}^{-1}$. The eddy flux can be compared to an order of magnitude estimate of the divergence of the alongshore mean salt flux,

$$\langle (vs)_y \rangle \quad (13)$$

where v is the alongshore mean undercurrent velocity and s is the mean salinity. The angle brackets denote the mean and the subscript y denotes the derivative in the alongshore direction. From the climatological mean of the California Undercurrent measured by CUGN, a reasonable estimate of v is 3 cm s^{-1} on Lines 66.7 and 80.0 while between Lines 66.7 and 80.0 Δs is 0.04 PSU and Δy is 300 km. A rough estimate of the divergence of the alongshore mean salt flux, at depth and due to the undercurrent, is $4 \times 10^{-9} \text{ PSU s}^{-1}$. Thus, the order of magnitude of the divergence of the across-shore eddy salt flux is the same as that of the divergence of the alongshore mean salt flux. Due to the water mass relationship between salinity, temperature, dissolved oxygen, and pH, it is expected that STEs are important for the offshore movement of heat, dissolved oxygen, and pH as well as salinity. The salt flux scaling estimates here provide further justification for the assertion from the northern CCS glider study that STEs are important for the offshore movement of salt (Pelland et al., 2013). Without needing to track every eddy individually, observations still support the magnitude of the divergence of the across-shore eddy salt flux as being significant.

A few sources of error are discussed below. One source of error is the unknown angle of propagation between the transect and STE propagation which may have resulted in STEs not being observed or observed with higher speeds (Eq. 11). Here the deviation of the transect lines south of west is $\alpha = 25^\circ$ or $\alpha = 26^\circ$, such that the westward Rossby wave speeds were adjusted upwards around 10%. As it is unknown at what angle the eddy may have traveled with respect to the transect, the reported across-

shore eddy speed may be overestimated by an unknown value, and the across-shore propagation speed has not been adjusted. However, along Line 66.7 there were salinity anomaly streaks observed for hundreds of kilometers along the transect, suggesting that a signal from eddies mostly aligned to the glider path was measured. There are possibly errors due to the resolution of the SLA product, which is a mapped product with a long spatial decorrelation scale. However the joint PDFs of dynamic height anomaly from the profile data from 500 m to 10 m and layer salinity and layer thickness (not shown) suggested that layer salinity and dynamic height anomaly were independent and that layer thickness and dynamic height anomaly were weakly negatively correlated; these results were consistent with those from SLA. Studies using observations and theory have found that STEs can become paired with surface eddies which will modify the STE surface expression and that the surface expression can evolve by radiating Rossby waves (Bashmachnikov et al., 2014; Carton et al., 2010). These studies are consistent with our findings that STEs and their surface expressions are weakly correlated.

The propagation of STEs in the CCS suggests that there is an important pathway from the coast to the open ocean that can transport water of anomalous heat, salinity, and important biogeochemical properties. Coastal deoxygenation has been observed in the CCS, and as found here through direct observations, anticyclonic STEs transport low-oxygen water to offshore regions. As the low-oxygen California Undercurrent water also has low pH, STEs may also impact coastal pH dynamics. With respect to future observations, increasing the alongshore resolution of the CUGN glider dataset would better capture the alongshore variability in STEs and the propagation direction of STEs. The existing alongshore resolution is around 300 km, and for example, adding two glider lines between Lines 66.7 and 80.0 would increase the alongshore resolution to 100 km, roughly the size of the STEs observed. Future work may be able to quantify from observations the across-shore eddy salt flux due to STEs, improving on the scaling argument presented here. The subthermocline eddy across-shore tracer flux would be an important contribution to understanding coastal eddy dynamics, especially as subthermocline tracer fluxes may differ from fluxes from barotropic eddies or eddies in the surface mixed layer.

Chapter 2, in full, is a reprint of the material as it appears in: Ren, A.S. and Rudnick, D.L. (2022) Across-shore propagation of subthermocline eddies in the California Current System. *Journal of Physical Oceanography*, 52(1), 39-51. The dissertation author was the primary investigator and author of this paper.

References

- Alin, S. R., Feely, R. A., Dickson, A. G., Hernández-Ayón, J. M., Juranek, L. W., Ohman, M. D., & Goericke, R. (2012). Robust empirical relationships for estimating the carbonate system in the southern California Current System and application to CalCOFI hydrographic cruise data (2005–2011). *Journal of Geophysical Research: Oceans*, 117(C5).
- Armi, L., Hebert, D., Oakey, N., Price, J. F., Richardson, P. L., Rossby, H. T., & Ruddick, B. (1989). Two Years in the Life of a Mediterranean Salt Lens. *Journal of Physical Oceanography*, 19(3), 354-370. [https://doi.org/10.1175/1520-0485\(1989\)019<0354:tyitlo>2.0.co;2](https://doi.org/10.1175/1520-0485(1989)019<0354:tyitlo>2.0.co;2)
- Bashmachnikov, I., Carton, X., & Belonenko, T. V. (2014). Characteristics of surface signatures of Mediterranean water eddies. *Journal of Geophysical Research: Oceans*, 119(10), 7245-7266. <https://doi.org/https://doi.org/10.1002/2014JC010244>
- Bendat, J. S., & Piersol, A. G. (2011). *Random data: analysis and measurement procedures* (Vol. 729). John Wiley & Sons.
- Bograd, S. J., Schroeder, I. D., & Jacox, M. G. (2019). A water mass history of the Southern California current system. *Geophysical Research Letters*, 46(12), 6690-6698. <https://doi.org/10.1029/2019gl082685>
- Bretherton, F. P., Davis, R. E., & Fandry, C. B. (1976). A technique for objective analysis and design of oceanographic experiments applied to MODE-73. *Deep Sea Research and Oceanographic Abstracts*, 23(7), 559-582. [https://doi.org/https://doi.org/10.1016/0011-7471\(76\)90001-2](https://doi.org/https://doi.org/10.1016/0011-7471(76)90001-2)
- Carton, X., Daniault, N., Alves, J., Cherubin, L., & Ambar, I. (2010). Meddy dynamics and interaction with neighboring eddies southwest of Portugal: Observations and modeling. *Journal of Geophysical Research: Oceans*, 115(C6). <https://doi.org/https://doi.org/10.1029/2009JC005646>
- Chelton, D. B., deSzoeko, R. A., Schlax, M. G., Naggar, K. E., & Siwertz, N. (1998). Geographical Variability of the First Baroclinic Rossby Radius of Deformation. *Journal of Physical Oceanography*, 28(3), 433-460. [https://doi.org/10.1175/1520-0485\(1998\)028<0433:gvotfb>2.0.co;2](https://doi.org/10.1175/1520-0485(1998)028<0433:gvotfb>2.0.co;2)
- Chelton, D. B., & Schlax, M. G. (1996). Global observations of oceanic Rossby waves. *Science*, 272, 234-238.
- Chelton, D. B., Schlax, M. G., & Samelson, R. M. (2011). Global observations of nonlinear mesoscale eddies. *Progress in Oceanography*, 91(2), 167-216. <https://doi.org/https://doi.org/10.1016/j.pocean.2011.01.002>
- Chelton, D. B., Schlax, M. G., Samelson, R. M., & de Szoeko, R. A. (2007). Global observations of large oceanic eddies. *Geophysical Research Letters*, 34(15). <https://doi.org/10.1029/2007gl030812>
- Chereskin, T. K., Morris, M. Y., Niiler, P. P., Kosro, P. M., Smith, R. L., Ramp, S. R., Collins, C. A., & Musgrave, D. L. (2000). Spatial and temporal characteristics of the mesoscale circulation of the California Current from eddy-resolving moored and shipboard measurements. *Journal of Geophysical Research: Oceans*, 105(C1), 1245-1269. <https://doi.org/10.1029/1999jc900252>

- Collins, C. A., Margolina, T., Rago, T. A., & Ivanov, L. (2013). Looping RAFOS floats in the California Current System. *Deep Sea Research Part II: Topical Studies in Oceanography*, 85, 42-61. <https://doi.org/https://doi.org/10.1016/j.dsr2.2012.07.027>
- Cornuelle, B. D., Chereskin, T. K., Niiler, P. P., Morris, M. Y., & Musgrave, D. L. (2000). Observations and modeling of a California undercurrent eddy. *Journal of Geophysical Research: Oceans*, 105(C1), 1227-1243. <https://doi.org/10.1029/1999jc900284>
- Cushman-Roisin, B., & Beckers, J.-M. (2011). *Introduction to geophysical fluid dynamics: physical and numerical aspects* (Vol. 101). Academic Press.
- D'Asaro, E. A. (1988). Generation of submesoscale vortices: A new mechanism. *Journal of Geophysical Research: Oceans*, 93(C6), 6685-6693. <https://doi.org/doi:10.1029/JC093iC06p06685>
- Davis, R. E., Ohman, M. D., Rudnick, D. L., & Sherman, J. T. (2008). Glider surveillance of physics and biology in the southern California Current System. *Limnology and Oceanography*, 53(5part2), 2151-2168. https://doi.org/10.4319/lo.2008.53.5_part_2.2151
- Dugan, J. P., Mied, R. P., Mignerey, P. C., & Schuetz, A. F. (1982). Compact, intrathermocline eddies in the Sargasso Sea. *Journal of Geophysical Research: Oceans*, 87(C1), 385-393. <https://doi.org/doi:10.1029/JC087iC01p00385>
- Flierl, G. R. (1977). The Application of Linear Quasigeostrophic Dynamics to Gulf Stream Rings. *Journal of Physical Oceanography*, 7(3), 365-379.
- Frenger, I., Bianchi, D., Stührenberg, C., Oschlies, A., Dunne, J., Deutsch, C., Galbraith, E., & Schütte, F. (2018). Biogeochemical Role of Subsurface Coherent Eddies in the Ocean: Tracer Cannonballs, Hypoxic Storms, and Microbial Stewpots? *Global Biogeochemical Cycles*, 32(2), 226-249. <https://doi.org/doi:10.1002/2017GB005743>
- Garfield, N., Collins, C. A., Paquette, R. G., & Carter, E. (1999). Lagrangian Exploration of the California Undercurrent, 1992–95. *Journal of Physical Oceanography*, 29(4), 560-583. [https://doi.org/10.1175/1520-0485\(1999\)029<0560:leotcu>2.0.co;2](https://doi.org/10.1175/1520-0485(1999)029<0560:leotcu>2.0.co;2)
- Gill, A. E. (1982). *Atmosphere-Ocean Dynamics*. Academic Press.
- Gula, J., Blacic, T. M., & Todd, R. E. (2019). Submesoscale Coherent Vortices in the Gulf Stream. *Geophysical Research Letters*, 46(5), 2704-2714. <https://doi.org/https://doi.org/10.1029/2019GL081919>
- Gula, J., Molemaker, M. J., & McWilliams, J. C. (2016). Topographic generation of submesoscale centrifugal instability and energy dissipation. *Nature Communications*, 7(1), 12811. <https://doi.org/10.1038/ncomms12811>
- Hsu, H.-m., Oey, L.-Y., Johnson, W., Dorman, C., & Hodur, R. (2007). Model Wind over the Central and Southern California Coastal Ocean. *Monthly Weather Review*, 135(5), 1931-1944. <https://doi.org/10.1175/mwr3389.1>
- Hunkins, K. L. (1974). Subsurface eddies in the Arctic ocean. *Deep Sea Research and Oceanographic Abstracts*, 21(12), 1017-1033. [https://doi.org/https://doi.org/10.1016/0011-7471\(74\)90064-3](https://doi.org/https://doi.org/10.1016/0011-7471(74)90064-3)

- Huyer, A., Barth, J. A., Kosro, P. M., Shearman, R. K., & Smith, R. L. (1998). Upper-ocean water mass characteristics of the California current, Summer 1993. *Deep Sea Research Part II: Topical Studies in Oceanography*, 45(8), 1411-1442. [https://doi.org/https://doi.org/10.1016/S0967-0645\(98\)80002-7](https://doi.org/https://doi.org/10.1016/S0967-0645(98)80002-7)
- Ienna, F., Jo, Y.-H., & Yan, X.-H. (2014). A New Method for Tracking Meddies by Satellite Altimetry. *Journal of Atmospheric and Oceanic Technology*, 31(6), 1434-1445. <https://doi.org/10.1175/jtech-d-13-00080.1>
- Ivanov, L. M., Collins, C. A., Margolina, T. M., Piterbarg, L. I., & Eremeev, V. N. (2008). On westward transport processes off central California revealed by RAFOS floats. *Geophysical Research Letters*, 35(18). <https://doi.org/https://doi.org/10.1029/2008GL034689>
- Koblinsky, C. J., Simpson, J. J., & Dickey, T. D. (1984). An offshore eddy in the California current system part II: Surface manifestation. *Progress in Oceanography*, 13(1), 51-69. [https://doi.org/https://doi.org/10.1016/0079-6611\(84\)90005-3](https://doi.org/https://doi.org/10.1016/0079-6611(84)90005-3)
- Kuragano, T., & Kamachi, M. (2000). Global statistical space-time scales of oceanic variability estimated from the TOPEX/POSEIDON altimeter data. *Journal of Geophysical Research: Oceans*, 105(C1), 955-974. <https://doi.org/https://doi.org/10.1029/1999JC900247>
- Lukas, R., & Santiago-Mandujano, F. (2001). Extreme water mass anomaly observed in the Hawaii ocean time-series. *Geophysical Research Letters*, 28(15), 2931-2934. <https://doi.org/doi:10.1029/2001GL013099>
- Manley, T. O., & Hunkins, K. (1985). Mesoscale eddies of the Arctic Ocean. *Journal of Geophysical Research: Oceans*, 90(C3), 4911-4930. <https://doi.org/10.1029/JC090iC03p04911>
- McClatchie, S. (2014). The CalCOFI Sampling Domain. In *Regional Fisheries Oceanography of the California Current System: The CalCOFI program* (pp. 8-11). Springer Netherlands.
- McDowell, S. E., & Rossby, H. T. (1978). Mediterranean Water: An Intense Mesoscale Eddy off the Bahamas. *Science*, 202(4372), 1085-1087. <https://doi.org/10.1126/science.202.4372.1085>
- McWilliams, J. C. (1985). Submesoscale, coherent vortices in the ocean. *Reviews of Geophysics*, 23(2), 165-182. <https://doi.org/doi:10.1029/RG023i002p00165>
- McWilliams, J. C., & Flierl, G. R. (1979). On the Evolution of Isolated, Nonlinear Vortices. *Journal of Physical Oceanography*, 9(6), 1155-1182. [https://doi.org/10.1175/1520-0485\(1979\)009<1155:oteoin>2.0.co;2](https://doi.org/10.1175/1520-0485(1979)009<1155:oteoin>2.0.co;2)
- Molemaker, M. J., McWilliams, J. C., & Dewar, W. K. (2015). Submesoscale Instability and Generation of Mesoscale Anticyclones near a Separation of the California Undercurrent. *Journal of Physical Oceanography*, 45(3), 613-629. <https://doi.org/10.1175/jpo-d-13-0225.1>
- Pelland, N. A., Eriksen, C. C., & Lee, C. M. (2013). Subthermocline Eddies over the Washington Continental Slope as Observed by Seagliders, 2003–09. *Journal of Physical Oceanography*, 43(10), 2025-2053. <https://doi.org/10.1175/jpo-d-12-086.1>

- Pujol, M. I., Faugère, Y., Taburet, G., Dupuy, S., Pelloquin, C., Ablain, M., & Picot, N. (2016). DUACS DT2014: the new multi-mission altimeter data set reprocessed over 20 years. *Ocean Sci.*, 12(5), 1067-1090. <https://doi.org/10.5194/os-12-1067-2016>
- Ren, A. S., & Rudnick, D. L. (2021). Temperature and salinity extremes from 2014-2019 in the California Current System and its source waters. *Communications Earth & Environment*, 2(1), 62. <https://doi.org/10.1038/s43247-021-00131-9>
- Robinson, A. R. (1983). Overview and Summary of Eddy Science. In A. R. Robinson (Ed.), *Eddies in Marine Science* (pp. 3-15). Springer-Verlag.
- Rudnick, D. L. (2016). *California Underwater Glider Network* [data set]. <https://doi.org/10.21238/S8SPRAY1618>
- Rudnick, D. L., & Cole, S. T. (2011). On sampling the ocean using underwater gliders. *Journal of Geophysical Research: Oceans*, 116(C8). <https://doi.org/https://doi.org/10.1029/2010JC006849>
- Rudnick, D. L., Davis, R. E., Eriksen, C. C., Fratantoni, D. M., & Perry, M. J. (2004). Underwater Gliders for Ocean Research. *Marine Technology Society Journal*, 38(2), 73-84. <https://doi.org/10.4031/002533204787522703>
- Rudnick, D. L., Sherman, J. T., & Wu, A. P. (2018). Depth-Average Velocity from Spray Underwater Gliders. *Journal of Atmospheric and Oceanic Technology*, 35(8), 1665-1673. <https://doi.org/10.1175/JTECH-D-17-0200.1>
- Rudnick, D. L., Zaba, K. D., Todd, R. E., & Davis, R. E. (2017a). A climatology of the California Current System from a network of underwater gliders. *Progress in Oceanography*, 154, 64-106. <https://doi.org/10.1016/j.pocean.2017.03.002>
- Rudnick, D. L., Zaba, K. D., Todd, R. E., & Davis, R. E. (2017b). *A climatology using data from the California Underwater Glider Network*. <https://doi.org/10.21238/S8SPRAY7292>
- Saraceno, M., Strub, P. T., & Kosro, P. M. (2008). Estimates of sea surface height and near-surface alongshore coastal currents from combinations of altimeters and tide gauges. *Journal of Geophysical Research: Oceans*, 113(C11). <https://doi.org/https://doi.org/10.1029/2008JC004756>
- Simpson, J. J., Dickey, T. D., & Koblinsky, C. J. (1984). An offshore eddy in the California current system Part I: Interior dynamics. *Progress in Oceanography*, 13(1), 5-49. [https://doi.org/https://doi.org/10.1016/0079-6611\(84\)90004-1](https://doi.org/https://doi.org/10.1016/0079-6611(84)90004-1)
- Steinberg, J. M., Pelland, N. A., & Eriksen, C. C. (2019). Observed Evolution of a California Undercurrent Eddy. *Journal of Physical Oceanography*, 49(3), 649-674. <https://doi.org/10.1175/JPO-D-18-0033.1>
- Todd, R. E., Rudnick, D. L., Mazloff, M. R., Davis, R. E., & Cornuelle, B. D. (2011). Poleward flows in the southern California Current System: Glider observations and numerical simulation. *Journal of Geophysical Research: Oceans*, 116(C2). <https://doi.org/10.1029/2010jc006536>

CHAPTER 3: The annual cycle of dissolved oxygen from high-resolution glider observations in the California Current System

Introduction

Dissolved oxygen is important for marine life and has been measured as an oceanographic variable since the time of the 1873-1876 H.M.S. Challenger expedition (Carpenter, 1873; Dittmar, 1884). Dissolved oxygen is not a conservative tracer. As an oceanographic tracer dissolved oxygen can indicate the productivity of the ocean by being a measure of the total photosynthesis minus respiration, or net community production. At the ocean-atmosphere boundary, dissolved oxygen likewise may be added or removed from the ocean as the boundary layer comes into equilibrium with the overlying oxygen in the atmosphere. Dissolved oxygen can also indicate physical mechanisms such as vertical mixing, vertical and horizontal advection, and gas exchange at the ocean-atmosphere boundary layer.

In the global ocean, the annual cycle of dissolved oxygen has been mapped as part of the Levitus climatology or World Ocean Atlas; the latest version is the World Ocean Atlas 2018 (WOA18). This atlas is calculated on a $1^\circ \times 1^\circ$ grid using objective analysis and provides monthly values based on observations from 1955 to the end of 2017 (Garcia, Boyer, et al., 2019; Garcia, Weathers, et al., 2019). Spray gliders, autonomous underwater vehicles, used in a regional ocean can collect sustained, high-resolution profiles in time and space over the period of multiple years, providing the observations necessary to resolve processes in the coastal ocean. Here, observations from four years between 2017-2020 of dissolved oxygen in the California Current System (CCS) taken with gliders as part of the California Underwater Glider Network (CUGN) are used to make an annual cycle of the top 500 meters of the ocean on three onshore-offshore transects, Line 66.7, Line 80.0, and Line 90.0 that span up to 500 km from the coastline (Fig. 3.1). The individual profiles of dissolved oxygen taken by CUGN gliders are roughly 3 hours and 3 km apart, and the annual cycle calculated from the CUGN dissolved oxygen observations has a resolution of 5 km in horizontal distance, 10 m in depth, and is reported on every day of a year.

The high-resolution annual cycle allows for studying mechanisms. Understanding the mechanisms driving the annual change in distribution of dissolved oxygen is a minimum requirement before addressing natural climate variability or global warming. Climate change is likely to affect the timing and magnitude of peaks and troughs of the annual cycle. Important elements in the CCS include coastal upwelling, the annual cycle of upper ocean productivity, the annual cycle of surface ocean temperature and gas exchange, and the annual cycle of mixing and stratification. In addition, the annual cycle of the major ocean currents in the CCS, the equatorward California Current and the poleward California Undercurrent, may affect dissolved oxygen concentrations due to the different water masses carried by each current.

Here, we first describe the major features of the mean and annual cycle of dissolved oxygen on three transects that are part of CUGN. Subsequently, we discuss major features of the annual cycle within regions of the CCS: the upwelling dominated region in the upper ocean and beneath the euphotic zone and the upper ocean offshore of coastal transition zone. In the CCS the offshore ecosystem is oligotrophic while the inshore region is eutrophic, highly affected by upwelling (Ohman et al., 2013). The region where coastal upwelling due to divergence by Ekman transport at the coastline occurs is the nearshore 50 km, but the region from 50-200 km has been described as the coastal transition zone (Chavez et al., 2002), and is a region affected by offshore upwelling filaments in the upper ocean (Brink & Cowles, 1991). For this paper, the upwelling-dominated region is taken to be from the coast to the offshore edge of the coastal transition zone, which is roughly 200-300 km from the coast.

Data & Methods

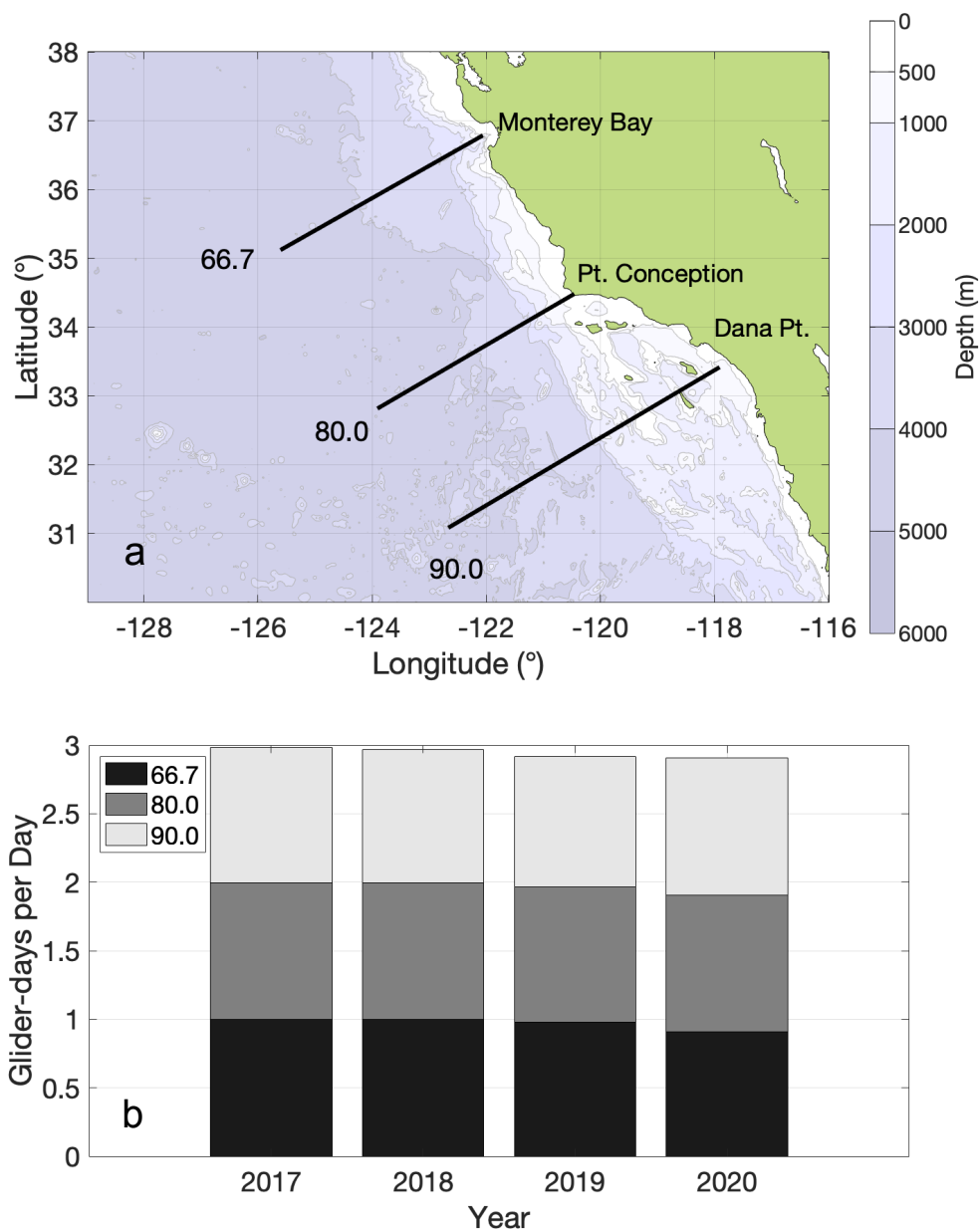


Figure 3.1 (a) The coastal domain monitored by CUGN. Glider lines 66.7, 80.0, and 90.0 are plotted in black. The coastal bathymetry is plotted in color contours. (b) The coverage of the three glider lines 66.7, 80.0, and 90.0 plotted as the ratio of glider days per day from 2017-2020. One glider day per day is equivalent to one line having glider observations for the full year. The maximum value for the Lines 66.7, 80.0, and 90.0 is three.

Dissolved oxygen, temperature, salinity, and chl-*a* fluorescence observations were collected as part of CUGN during four years between 2017-2020. The observations were located on Line 90.0 off Dana Point, Line 80.0 off Point Conception, and Line 66.7 off Monterey Bay (Fig. 3.1a). The three lines

follow the geometry of the California Cooperative Fisheries Investigations (CalCOFI) hydrographic survey, in operation since 1949 (McClatchie, 2014). An underwater glider is a buoyancy-driven autonomous vehicle that generates profiles of variables as it completes a sawtooth pattern of dives (Rudnick et al., 2004). In CUGN, the Spray underwater gliders are programmed to dive to 500 m and travel at about 0.25 m s^{-1} . One across-shore transect of 350-500 km takes 2-3 weeks to complete. Individual gliders are recovered after roughly 100 days at sea at which point new gliders are deployed. This sampling strategy allows for continuous data coverage on the lines. Over four years, the average coverage of the gliders on the three lines, 66.7, 80.0, and 90.0, on each year was above 95%. The lowest coverage, 91%, occurred on Line 66.7 in 2020 (Fig. 3.1b).

The temperature and salinity were collected by Seabird 41CP sensors on the gliders and the data acquisition and quality control has been described (Rudnick et al., 2017). Absolute geostrophic velocities were calculated from the vertical shear using the thermal wind relationship and by referencing the vertical shear to the depth-averaged velocity as measured by the gliders (Rudnick et al., 2018). *Chl-a* fluorescence was collected with a Seapoint mini-scf sensor. The fluorescence was converted to a concentration unit of mg m^{-3} *chl-a*. The concentration of *chl-a* does not directly measure phytoplankton biomass due to variability in the biomass to *chl-a* ratio, but *chl-a* concentration may indicate patterns of phytoplankton biomass. To ensure consistency between *chl-a* fluorescence sensors, all *chl-a* concentration was corrected to be consistent with satellite *chl-a* observations at the surface and to fall to zero *chl-a* at depth. Dissolved oxygen was collected using a Seabird 63 optode sensor. To account for drift over the lifetime of the sensor, the dissolved oxygen was corrected. Glider observations from 2017-2018 were corrected with a gain factor based on comparison with bottle sample dissolved oxygen from the CalCOFI hydrographic survey program where oxygen is determined by Winkler titration. Glider observations from 2018-2020 were corrected with respect to full saturation and to zero oxygen using a gain and an offset determined with a laboratory procedure. Estimates from the most recent mission were used when parameter values were unable to be found using either laboratory or CalCOFI bottle sample

comparison methods. A pumped system ensures reliable flow over the sensors collecting oceanographic observations on the CUGN gliders.

The observations are depth-binned into 10 m intervals centered on 10 m, 20 m, and so on to 500 m depth. The glider's vertical speed is roughly 0.1 m s^{-1} , and observations are collected every 8 s, so roughly 12 observations are in each bin (Rudnick et al., 2017). To calculate the annual cycle, the observations from 2017-2020 are fit to 3 harmonics of sine and cosine and a constant. The annual cycle is calculated on each 10-m depth bin for every 5 km horizontal distance interval from the coastline. A gaussian weighting function with length-scale of 15 km is used to emphasize the observations nearest to each 5 km bin. The annual cycle is reported for every day of the year. The annual cycle of derived variables including potential density and geostrophic velocity are calculated from the temperature and salinity annual cycles.

A region of low but non-zero dissolved oxygen is called a hypoxic zone. The hypoxic level is determined for individual species as the concentration at which lower dissolved oxygen begins to affect organism function (Davis, 1975; Vaquer-Sunyer & Duarte, 2008). For this paper, the oxygen contour of $60 \text{ } \mu\text{mol kg}^{-1}$ is used to indicate a hypoxic boundary and provides a visual representation of areas of low dissolved oxygen waters, although individual species may have different reactions at any given oxygen concentration. Near 500 m, the glider observations measure the top of the oxygen minimum zone in the CCS. It is expected that measurements to 800 m or below would show the oxygen minimum and then increasing dissolved oxygen concentrations (Ren et al., 2018). Since the CUGN gliders do not measure the oxygen minimum, all areas deeper than the hypoxic boundary but shallower than 500 m on section plots contain oxygen lower than $60 \text{ } \mu\text{mol kg}^{-1}$.

A 1-dimensional vertical advection-diffusion model is run to help understand processes in the upper ocean. The model equation for dissolved oxygen is,

$$\frac{\partial C}{\partial t} = -w \frac{\partial C}{\partial z} + \frac{\partial}{\partial z} \left(\kappa \frac{\partial C}{\partial z} \right), \quad (1)$$

where C is the concentration of dissolved oxygen, z is the vertical coordinate, t is time, w is the vertical advection, and κ is the vertical diffusivity. Concurrently, a model of temperature is run using the same vertical diffusivity and vertical advection values as dissolved oxygen:

$$\frac{\partial T}{\partial t} = -w \frac{\partial T}{\partial z} + \frac{\partial}{\partial z} \left(\kappa \frac{\partial T}{\partial z} \right), \quad (2)$$

where T is temperature. Vertical profiles of κ , the vertical diffusivity, and w , the vertical advection, are piecewise constant and varied between different runs to represent different ocean conditions. We choose to neglect the term $\frac{\partial \kappa}{\partial z} \frac{\partial C}{\partial z}$ which has large values at the transitions between values but is zero for when w and κ are constant. The model uses a finite difference grid and a 4th order forward Runge-Kutta time-stepping scheme. The model has vertical resolution of 5 meters and the domain is from the ocean surface to 195 m depth. Note that the steady state version of the model equations is the system of equations used by Munk (1966) to describe the deep, interior ocean, the solution of which is an exponential with a length-scale of $\frac{\kappa}{w}$.

We attempt to model the annual cycle of the surface ocean, so the boundary conditions are important and will force the solution to change in time. The model of temperature is forced at the surface using a sinusoidal representation of the annual cycle of heat flux in the CCS:

$$F_s = 60 * \sin \left(2\pi * t - \frac{3\pi}{4} \right) + 80, \quad (3)$$

where F_s is the surface heat flux (W m^{-2}) and positive values indicate the ocean gaining heat. The surface ocean in the CCS is thought to gain heat from the atmosphere year-round, and an estimated mean annual heat flux value is 86 W m^{-2} (Bograd et al., 2001). The peak in modeled heat flux (Eq. 3) occurs in late summer. The temperature boundary condition at depth is no-flux or $\frac{\partial T}{\partial z} = 0$. The dissolved oxygen surface boundary condition is the saturation value of oxygen at each timestep, determined by the modeled temperature and using atmospheric pressure of 1 atm and salinity of 33. The oxygen boundary condition

at depth is no-flux or $\frac{\partial C}{\partial z} = 0$. The error from numerical integration, ε , is estimated using Richardson extrapolation,

$$\varepsilon_{u_{2\Delta t}} = \frac{(u_{2\Delta t} - u_{\Delta t})2^m}{2^m - 1}, \quad (4)$$

where m is the truncation order of the numerical method ($m=4$), u represents any model variable, $u_{\Delta t}$ represents the model variable run at high-resolution, and $u_{2\Delta t}$ represents the model run with a two times larger timestep than in the high-resolution case (Cushman-Roisin & Beckers, 2011). The low-resolution model time-step, used to calculate $\varepsilon_{u_{2\Delta t}}$, is 1×10^{-4} years or 52 minutes. The numerical error is at most on the order of 0.001 °C for temperature and on the order of 0.0001 $\mu\text{mol kg}^{-1}$ for dissolved oxygen. As the model is an idealized representation of differences in ocean regions, we find the level of numerical error using timestep of 52 minutes acceptable.

The net community production, or total primary production minus community respiration, was computed by tracking the dissolved oxygen concentration change during the subsurface dissolved oxygen maximum in summer, following the method used by (Riser & Johnson, 2008). A modified Redfield ratio is used to convert between moles of oxygen and moles of carbon, such that every 150 moles of oxygen produced corresponds to 106 moles of carbon produced (Anderson, 1995). The carbon produced is found in marine biomass. The net community production was calculated at the ocean depth of 60 m on Line 66.7 and Line 80.0, using the annual cycle averaged over the distances 300-350 km from shore, and over 30 days from July 19 through August 18. The net community production rate represents the change in the annual cycle at 60 m from July through August and is expressed in $\text{mmol m}^{-3} \text{ year}^{-1}$ of carbon. Net community production is a biological source minus sink term for dissolved oxygen.

Results

Before investigating the annual cycle of dissolved oxygen, the mean dissolved oxygen along Lines 66.7, 80.0, and 90.0 is presented (Fig 3.2). Over 500 m depth, there is a strong vertical gradient of dissolved oxygen. The values at 500 m approach zero $\mu\text{mol kg}^{-1}$ while the values at the surface approach 300 $\mu\text{mol kg}^{-1}$. The surface values of dissolved oxygen are expected to be high due to gas exchange with

the atmosphere, with dissolved oxygen concentrations around that of full saturation as determined by the ocean temperature, ocean salinity, atmospheric pressure, and humidity. Though not as strong as the vertical gradient, there is an across-shore gradient of dissolved oxygen with lower dissolved oxygen near the coast, and the horizontal gradient exists on both depth and isopycnal surfaces. On all three lines in the mean the hypoxic boundary, defined in this paper as the $60 \mu\text{mol kg}^{-1}$ dissolved oxygen contour, is found around 300 m depth and shoals from offshore to inshore. On Line 90.0, the hypoxic boundary is shallowest around 150-190 km from shore rather than at the coast like on Line 66.7 and Line 80.0.

The section plots of the four seasons are presented for Lines 66.7, 80.0, and 90.0, beginning with Line 66.7 (Fig. 3.3). The hypoxic boundary shoals inshore in spring and is the deepest in the winter and fall. At the coastline, the hypoxic boundary shoals from 300 m to 260 m from winter to spring. Offshore, the hypoxic boundary is deepest in the fall and winter and shallower in the spring and summer, although the variation between subsequent seasons in depth is less. From winter to spring and summer, the potential density contours of $25.25\text{-}25.5 \text{ kg m}^{-3}$ tilt upwards and outcrop due to upwelling. Lower dissolved oxygen is associated with the deeper isopycnals. In summer, solar heating creates warm, less dense water at the ocean surface and increased stratification in the upper 100 m. Increased stratification in the upper ocean is observed from the summer into the fall. Extremely light waters of less than 24 kg m^{-3} are found offshore of 200 km. In the summer and fall, a pronounced subsurface dissolved oxygen maximum occurs greater than 200 km from shore in the offshore region.

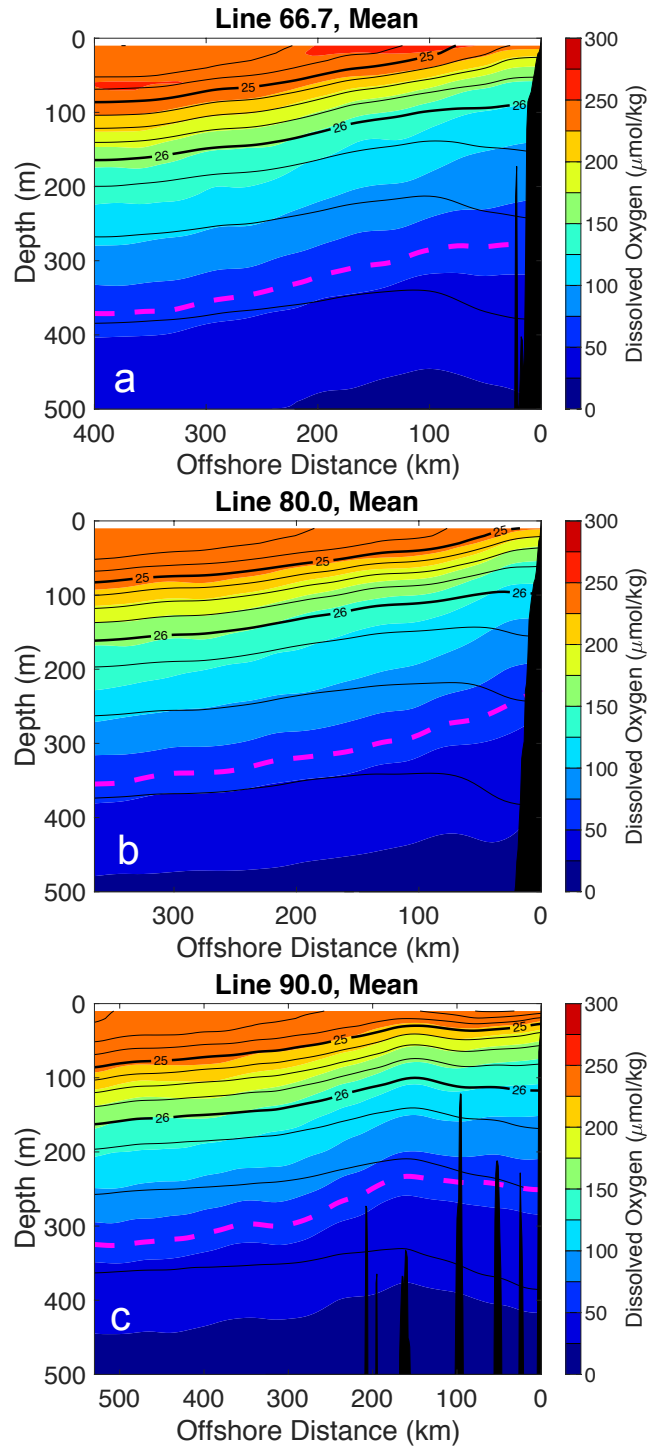


Figure 3.2 Mean section plots of dissolved oxygen on (a) Line 66.7 (b) Line 80.0, and (c) Line 90.0 using observations from 2017-2020. Potential density surfaces are plotted in black lines over the color contours. The thick black lines are $\sigma_{\theta} 25 \text{ kg m}^{-3}$ and 26 kg m^{-3} . A hypoxic boundary of $60 \mu\text{mol kg}^{-1}$ is plotted in a dashed magenta line.

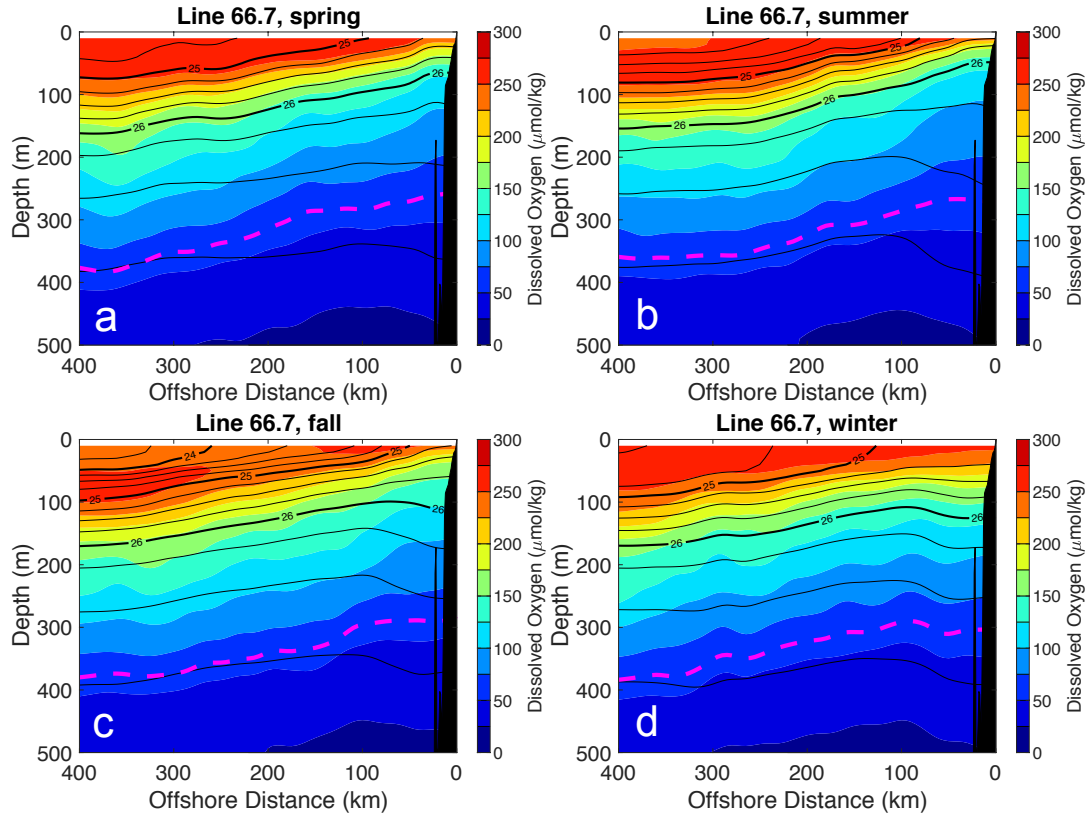


Figure 3.3 Seasonal plots of dissolved oxygen on Line 66.7. (a) Spring (b) summer (c) fall and (d) winter. The winter season is defined as December through February. Thin black lines denote potential density surfaces. Thick black lines denote σ_θ 24 kg m^{-3} , 25 kg m^{-3} , and 26 kg m^{-3} . A hypoxic boundary of $60 \mu\text{mol kg}^{-1}$ is plotted in a dashed magenta line.

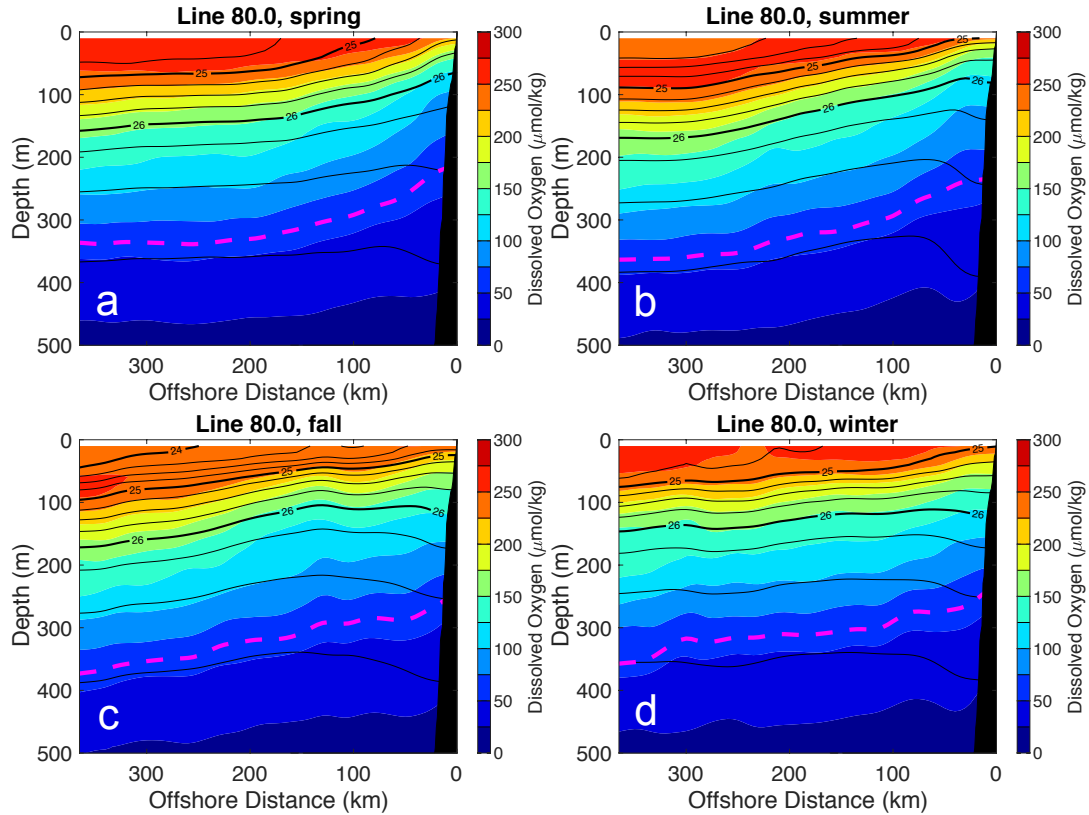


Figure 3.4 Seasonal plots of dissolved oxygen on Line 80.0. (a) Spring (b) summer (c) fall and (d) winter. The winter season is defined as December through February. Thin black lines denote potential density surfaces. Thick black lines denote σ_θ 24 kg m^{-3} , 25 kg m^{-3} , and 26 kg m^{-3} . A hypoxic boundary of $60 \text{ } \mu\text{mol kg}^{-1}$ is plotted in a dashed magenta line.

On Line 80.0, similar features to those of Line 66.7 are found, with upwelling at the surface, shoaling of the hypoxic boundary inshore in spring, and a subsurface dissolved oxygen maximum in summer and fall (Fig. 3.4). The hypoxic boundary inshore is at 240 m depth in the winter and 210 m depth in the spring, while it is at 230 m in summer and 250 m in fall. Offshore, averaged from 300-350 km, the hypoxic boundary varies between 340 and 360 m depth. The potential density surfaces of $25.0\text{-}25.5 \text{ kg m}^{-3}$ tilt upwards and outcrop in the spring, bringing lower dissolved oxygen water to the surface. Increased surface stratification in summer and fall is also a major feature on Line 80.0. A subsurface dissolved oxygen maximum is found in summer and fall greater than 200 km from shore.

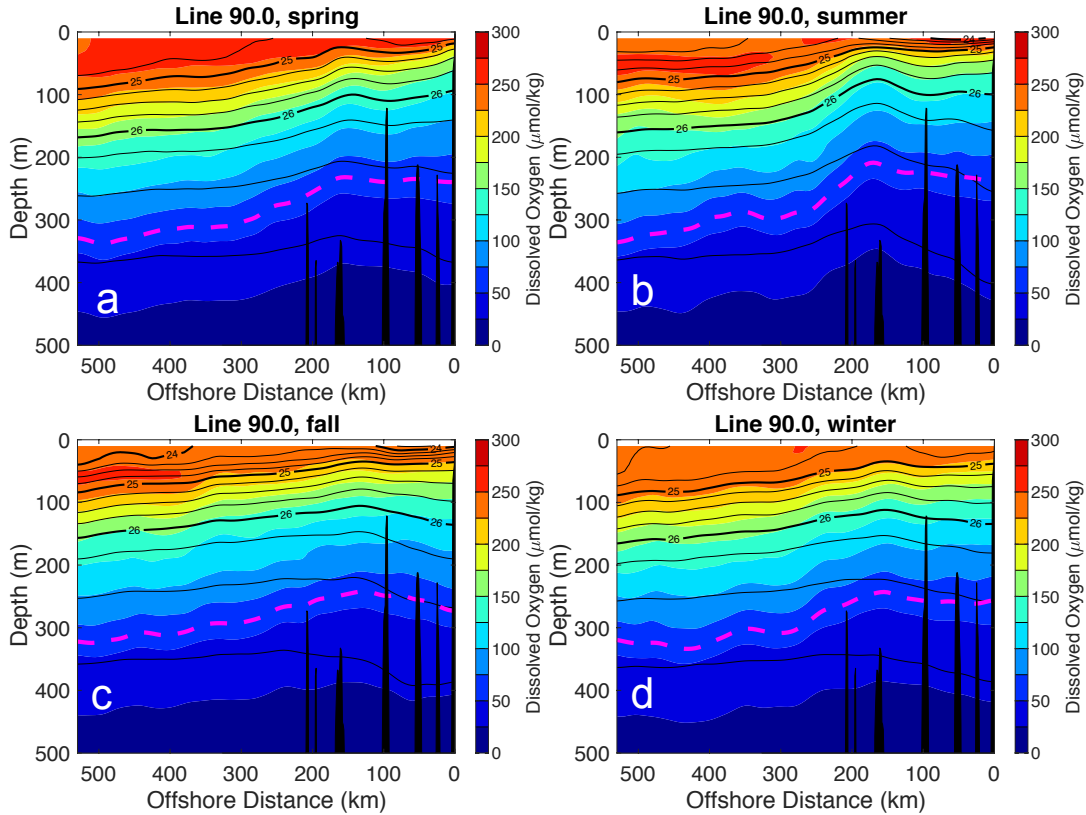


Figure 3.5 Seasonal plots of dissolved oxygen on Line 90.0. (a) Spring (b) summer (c) fall and (d) winter. The winter season is defined as December through February. Thin black lines denote potential density surfaces. Thick black lines denote σ_{θ} 24 kg m⁻³, 25 kg m⁻³, and 26 kg m⁻³. A hypoxic boundary of 60 $\mu\text{mol kg}^{-1}$ is plotted in a dashed magenta line.

The timing of upwelling and shoaling of the hypoxic boundary is different on Line 90.0 than on Lines 66.7, and 80.0, with the greatest upwelling and shoaling of the hypoxic boundary in summer (Fig. 3.5). The location of the greatest upwelling is near the Santa Rosa Ridge, a bathymetric feature that also demarcates the offshore edge of the Southern California Bight (Rudnick et al., 2017). Increased mixing from the internal tide has been found offshore of the Santa Rosa Ridge (Johnston & Rudnick, 2015), and the mechanism driving the seasonal summer upwelling along the ridge needs to be investigated. In contrast to the coastal upwelling on Lines 66.7 and 80.0, the shoaling isopycnals on Line 90.0 in the summer do not outcrop. Enhanced surface stratification in summer and fall also exists on Line 90.0 with σ_{θ} 24.0 kg m⁻³ water found both inshore and offshore. The depth of the hypoxic boundary averaged from 150-190 km is 250 m in the winter and fall, 240 m in the spring, and 210 m in the summer. Year-round,

the hypoxic boundary is generally shallowest 150-190 km from shore above the Santa Rosa Ridge and deepens in both the inshore and offshore directions. A subsurface dissolved oxygen maximum exists greater than 300 km from shore in the summer and fall.

The inshore dissolved oxygen annual cycle in the upper 200 m: Upwelling, ventilation, and phytoplankton blooms

Upwelling is a major physical process that affects the coastal region, including a nearshore 50 km that is strongly affected by divergence at the coast due to Ekman transport, and a coastal transition zone that extends to 200-300 km from shore. The seasonal upwelling affects the dissolved oxygen distribution, with lower dissolved oxygen found at higher depths due to shoaling isopycnals (Fig. 3.6-Fig. 3.8). On Line 66.7 at 30 m (Fig. 3.6), there are isopycnals denser than 25.2 kg m^{-3} found inshore from March through December, while there are isopycnals greater than 25.9 kg m^{-3} found in May and June. In the winter, 25.9 kg m^{-3} is found below 100 m depth. Low potential temperature, low dissolved oxygen saturation, and low dissolved oxygen concentration occur along with denser isopycnals. The across-shore gradient of dissolved oxygen is strong, with over $100 \mu\text{mol kg}^{-1}$ concentration change over 100 km at 30 m depth in certain months including May and June. On Line 80.0 at 30 m (Fig. 3.7) there are isopycnals denser than 25.2 kg m^{-3} found inshore from February through September, while there are isopycnals denser than 25.7 kg m^{-3} from April through June. On Line 80.0 the patterns of low potential temperature, low dissolved oxygen saturation, and low dissolved oxygen concentration match the pattern of denser isopycnals appearing. The across-shore gradient of dissolved oxygen is strongest in the months of April-July where there is a $100 \mu\text{mol kg}^{-1}$ change in dissolved oxygen concentration over 100 km at 30 m depth. On Line 90.0, the appearance of denser isopycnals at 30 m depth also coincides with colder and lower dissolved oxygen saturation and concentration waters (Fig. 3.8). Unlike on Line 66.7 and Line 80.0, there is upwelling offshore near the Santa Rosa Ridge, which affects the region between 100-200 km from shore. The shoaling of isopycnals at the coast appears earlier than near the ridge. Isopycnals denser than 25.1 kg m^{-3} appear in mid-March on the coast and late April near the ridge. The coastal potential density

returns to lighter than 25.1 kg m^{-3} in July while near the ridge, the potential density returns to lighter than 25.1 kg m^{-3} in August. The horizontal gradients of dissolved oxygen at 30 m are not as strong on Line 90.0 as on Lines 66.7 and 80.0.

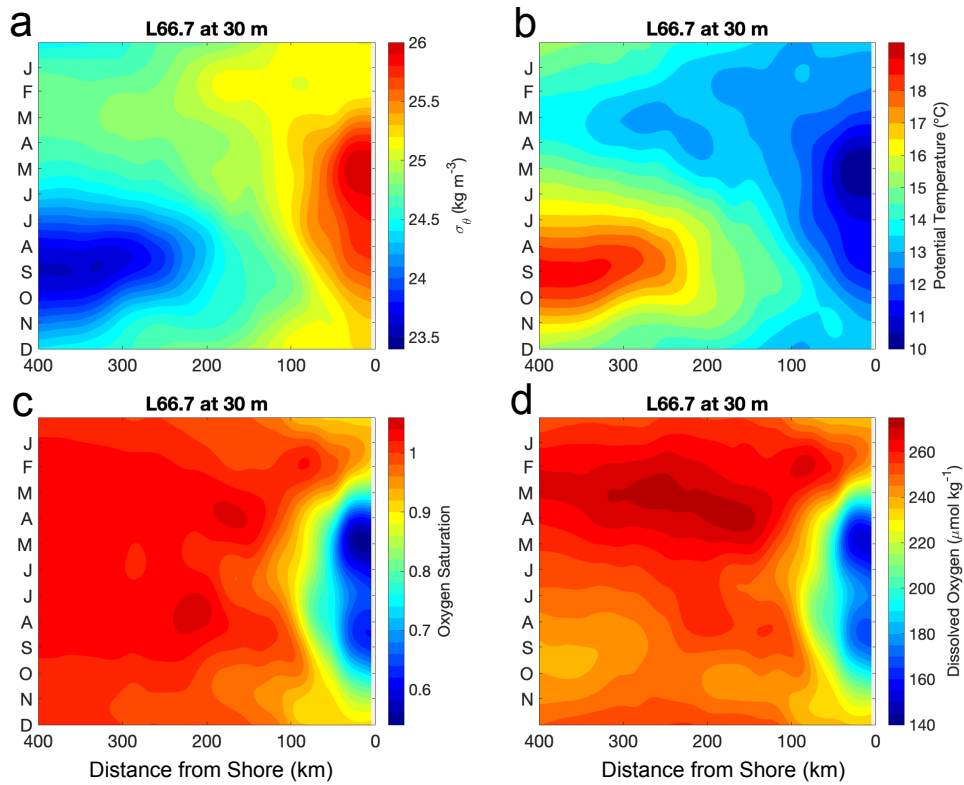


Figure 3.6 The annual cycle at 30 m depth on Line 66.7. (a) potential density σ_θ (kg m^{-3}) (b) potential temperature ($^\circ\text{C}$) (c) oxygen saturation (d) dissolved oxygen ($\mu\text{mol kg}^{-1}$).

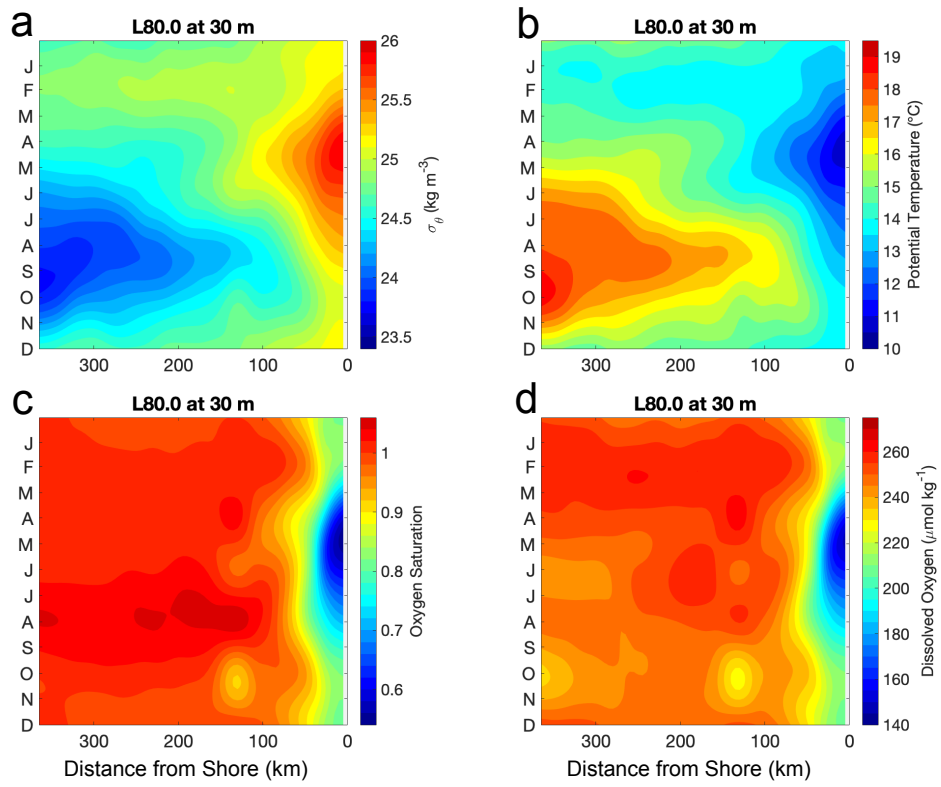


Figure 3.7 The annual cycle at 30 m depth on Line 80.0. (a) potential density σ_θ (kg m^{-3}) (b) potential temperature ($^\circ\text{C}$) (c) oxygen saturation (d) dissolved oxygen ($\mu\text{mol kg}^{-1}$).

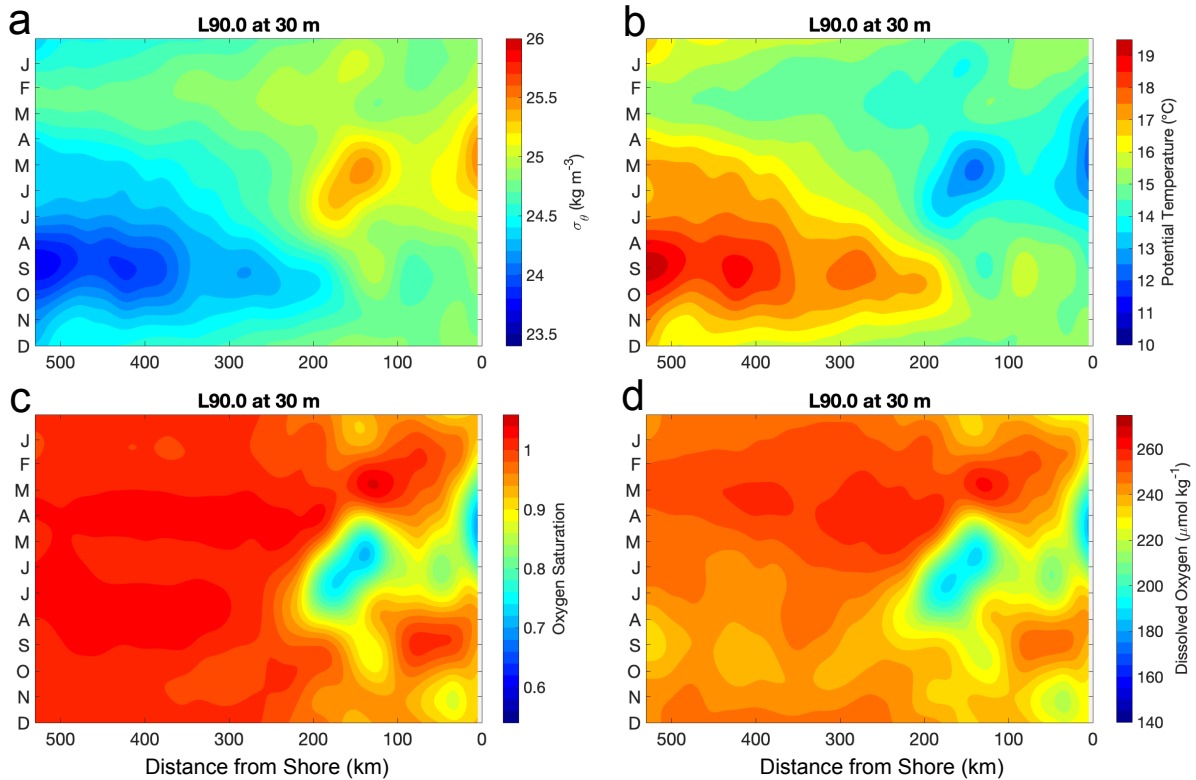


Figure 3.8 The annual cycle at 30 m depth on Line 90.0. (a) potential density σ_{θ} (kg m^{-3}) (b) potential temperature ($^{\circ}\text{C}$) (c) oxygen saturation (d) dissolved oxygen ($\mu\text{mol kg}^{-1}$).

While the greatest seasonal change in dissolved oxygen is predominantly explained by heaving of isopycnals, mixing also occurs. Along-isopycnal changes in potential temperature and dissolved oxygen saturation and concentration are found on shoaling and outcropping isopycnals. The potential temperature is generally higher on the isopycnal after it has shoaled and as it deepens in the water column (Figs. 3.9b-3.11b), suggesting that the water is being heated at the ocean surface. The depth of the isopycnal is important for dissolved oxygen concentration, with higher dissolved oxygen found along the isopycnal when it is closer to the surface. There is high dissolved oxygen found on an isopycnal before it outcrops and after it reappears (Figs. 3.9d-3.11d), suggesting that vertical, diabatic mixing occurs. The isopycnal chosen for Lines 66.7 and 80.0 is 25.4 kg m^{-3} which shoals and outcrops as part of seasonal upwelling (Figs. 3.9c-3.10c). The largest changes in temperature and dissolved oxygen on the isopycnal 25.4 kg m^{-3} occur from the coast to 100 km as the isopycnal becomes shallower than 50 m, and the magnitude of the change in oxygen concentration is around $50 \mu\text{mol kg}^{-1}$, corresponding to around a 20%

increase in dissolved oxygen saturation. On Line 90.0, the isopycnal that demonstrates outcropping is 24.8 kg m^{-3} , which does not exist in winter and early spring likely due to cooling and vertical mixing. On Line 90.0, the upwelling at the coast and near the Santa Rosa Ridge does not cause isopycnals to outcrop, though they do shoal (Fig. 3.8a). Extremely light waters of less than 24.5 kg m^{-3} are formed in the summer and early fall months from the coast to over 500 km from shore likely due to solar heating. On line 90.0, supersaturated waters of dissolved oxygen are found near the surface and associated with the outcropped isopycnal (Fig. 3.11c). The difference between dissolved oxygen concentration on potential density 24.8 kg m^{-3} at the surface and deeper in the water column on Line 90.0 is around $50 \text{ } \mu\text{mol kg}^{-1}$, similar to what is found on outcropping isopycnals on Lines 66.7 and 80.0. The supersaturation of dissolved oxygen could be due to primary production.

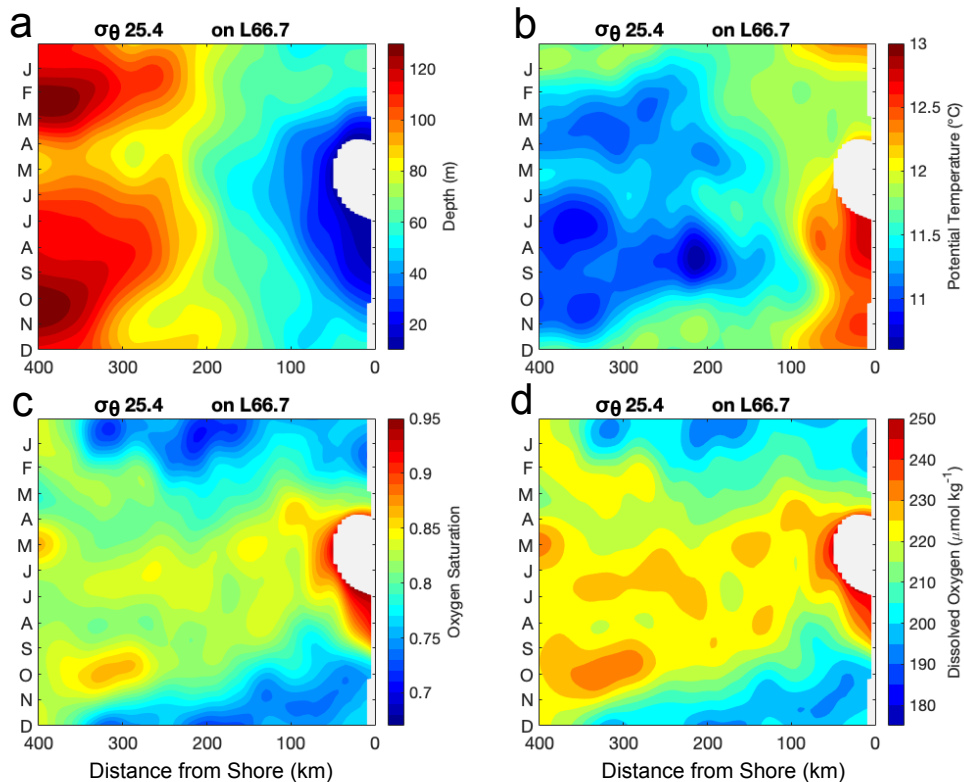


Figure 3.9 The annual cycle of properties on potential density $\sigma_{\theta} 25.4 \text{ kg m}^{-3}$ on Line 66.7. (a) Depth (m) (b) potential temperature ($^{\circ}\text{C}$) (c) oxygen saturation and (d) change in dissolved oxygen ($\mu\text{mol kg}^{-1}$) on the potential density surface.

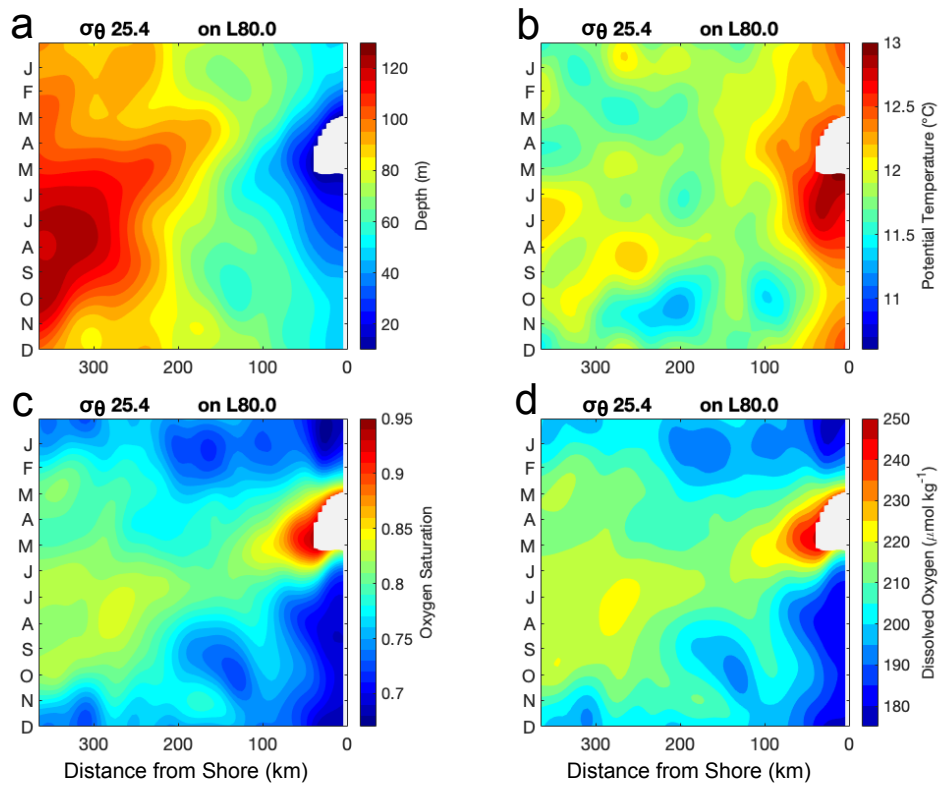


Figure 3.10 The annual cycle of properties on potential density σ_{θ} 25.4 kg m^{-3} on Line 80.0. (a) Depth (m) (b) potential temperature ($^{\circ}\text{C}$) (c) oxygen saturation and (d) dissolved oxygen ($\mu\text{mol kg}^{-1}$) on the potential density surface.

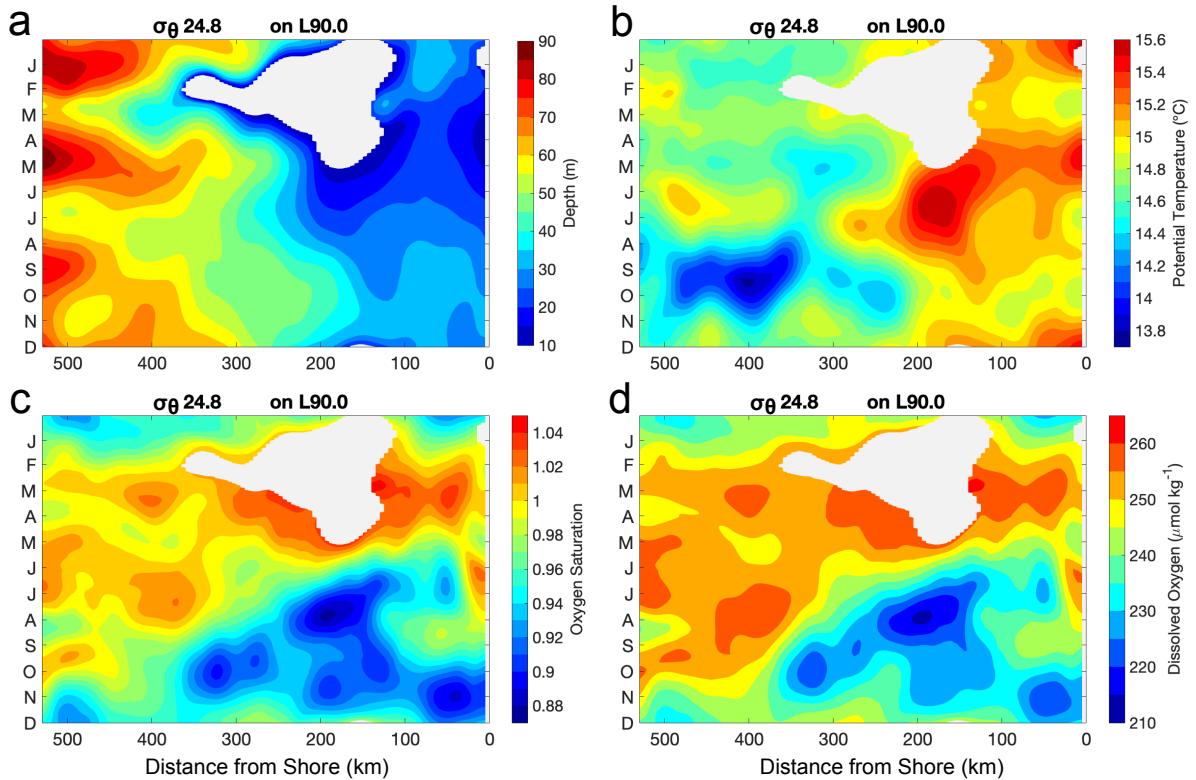


Figure 3.11 The annual cycle of properties on potential density $\sigma_{\theta} 24.8 \text{ kg m}^{-3}$ on Line 90.0. (a) Depth (m) (b) potential temperature ($^{\circ}\text{C}$) (c) oxygen saturation and (d) dissolved oxygen ($\mu\text{mol kg}^{-1}$) on the potential density surface.

Away from the ocean surface along outcropping isopycnals, there is elevated dissolved oxygen saturation and dissolved oxygen concentration, which suggests that along-isopycnal mixing may be occurring. On lines 66.7, 80.0, and 90.0, a roughly $10\text{-}20 \mu\text{mol kg}^{-1}$ elevated dissolved oxygen pattern is found, and the elevated oxygen pattern appears to move offshore from the outcropping site at the coast (Figs. 3.9d-3.11d), moving across 300 km in 3-6 months. On Lines 66.7 and 80.0, the concentration of dissolved oxygen on the isopycnal is higher near the outcropping region within 100 km of the coast and lower in the propagating signal, suggesting that the high dissolved oxygen could be mixing offshore along the isopycnal. Plots of the anomaly of dissolved oxygen from the annual mean on Lines 66.7, 80.0, and 90.0 on the isopycnals 25.4 kg m^{-3} and 24.8 kg m^{-3} (Fig. 3.12a,c,e) demonstrate that the maximum in oxygen anomaly is near the surface, and a particularly good example that suggests mixing is Line 80.0 on 25.4 kg m^{-3} (Fig. 3.12c). The elevated dissolved oxygen appears not to be due to a wave, such as a

Rossby wave, which hypothetically could heave the isopycnal to a shallower depth where mixing with oxygenated water could occur. Although there is a Rossby wave signature in isopycnal depth anomaly (Fig. 3.12b,d,f), the oxygen anomaly signal travels faster than the wave. On Line 80.0 (Fig. 3.12c-d), the negative (blue) anomaly in depth travels at a different speed than the positive (red) anomaly in dissolved oxygen. Finally, the chl-*a* anomaly from the annual mean along isopycnals 25.4 and 24.8 kg m⁻³ (Fig. 3.13b,d,f) does not show a pattern of growth that moves offshore with time, suggesting that primary production is not a source of the elevated dissolved oxygen signal on the isopycnal. The chl-*a* pattern suggests that there are better growing conditions for phytoplankton in summer and early fall along the entire 400 km from the coast on Lines 66.7 and 80.0, and one possible explanation is that there is more available light in the summer.

Overall, isopycnal heaving is the dominant process in terms of causing low dissolved-oxygen water to appear at the coast. The change at 30 m depth of dissolved oxygen is on the order of 100 $\mu\text{mol kg}^{-1}$ due to heaving. Mixing increases the dissolved oxygen concentration of the upwelled waters found at 30 m, and the increase in dissolved oxygen on an isopycnal is around 50 $\mu\text{mol kg}^{-1}$. The signal of elevated dissolved oxygen brought down into the interior of the ocean and offshore has a signal of around 10 $\mu\text{mol kg}^{-1}$. The along-isopycnal movement of oxygenated waters is evidence of ventilation of the isopycnal, one of the ways that properties of water found beneath the surface can be modified. Though relatively small in magnitude, the elevated dissolved oxygen due to ventilation may be important with respect to dynamics of the interior ocean, where the range of dissolved oxygen variability may not be as large as at the surface.

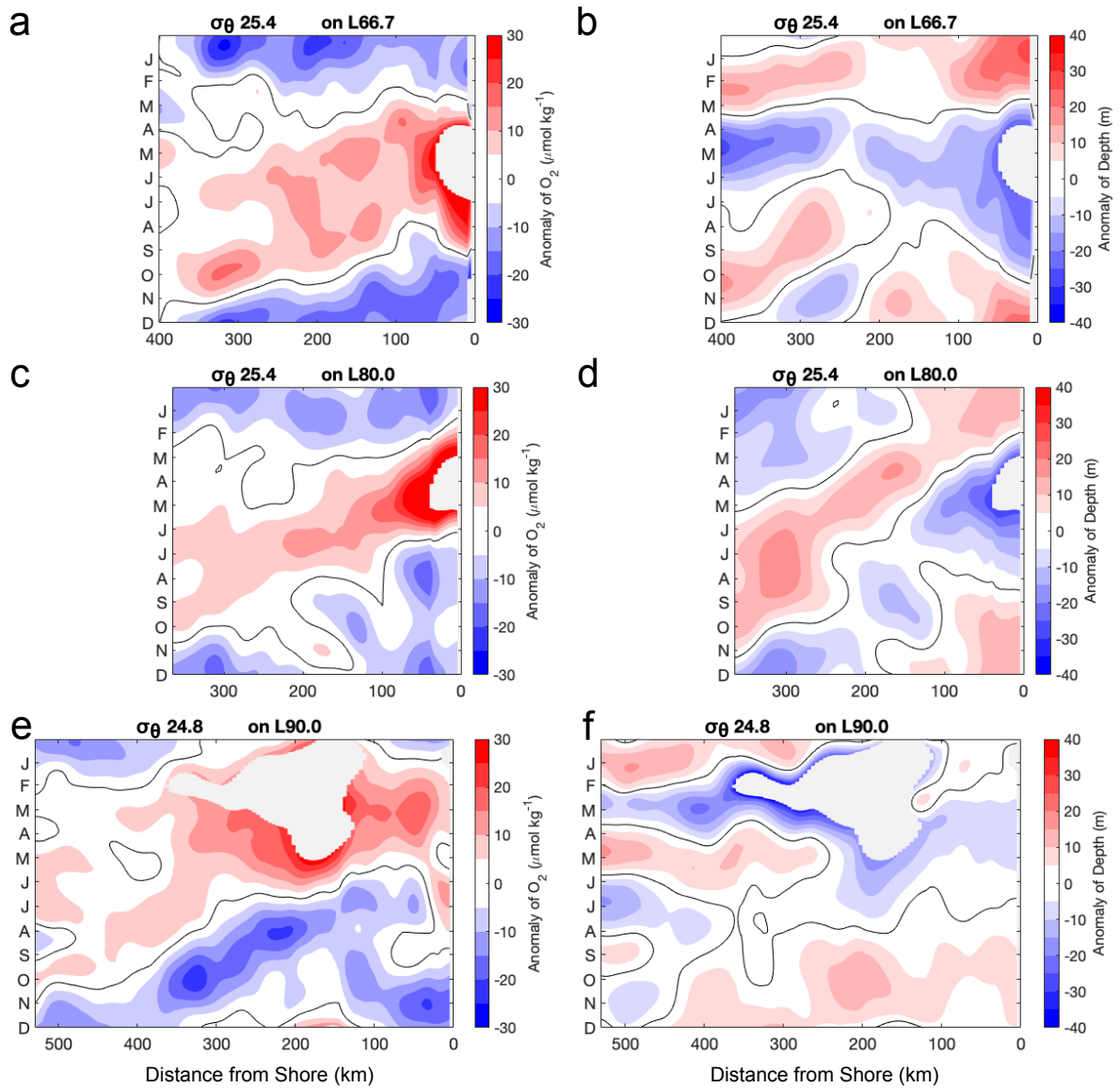


Figure 3.12 Anomalies from the annual mean on isopycnals of dissolved oxygen concentration ($\mu\text{mol kg}^{-1}$) and depth (m). (a) anomaly of dissolved oxygen concentration on 25.4 kg m^{-3} on Line 66.7 (b) anomaly of depth on 25.4 kg m^{-3} on Line 66.7 (c) anomaly of dissolved oxygen concentration on 25.4 kg m^{-3} on Line 80.0 (d) anomaly of depth on 25.4 kg m^{-3} on Line 80.0 (e) anomaly of dissolved oxygen concentration on 24.8 kg m^{-3} on Line 90.0 and (f) anomaly of depth on 24.8 kg m^{-3} on Line 90.0.

Biological sources of dissolved oxygen exist in the upwelling region because measurements of chl-*a* demonstrate that there are phytoplankton blooms (Fig. 3.13a,c,e). The blooms occur during and after the shoaling of isopycnals due to upwelling, with the strongest chl-*a* concentrations occurring in summer and fall on Lines 66.7 and 80.0 (Fig. 3.13a,c). There is a semi-annual increase in chl-*a* on Line 90.0 near the Santa Rosa Ridge, with blooms in the late spring through summer, and winter (Fig. 3.13e).

There is isopycnal shoaling in winter near the Santa Rosa Ridge, which affects depths of 40 m and below (not shown) which suggests that the winter bloom is influenced by upwelling, though the upwelling is of weaker strength than in summer. Quantification of the surface phytoplankton bloom contribution to dissolved oxygen concentration is difficult; the blooms occur in water undersaturated in dissolved oxygen. The 10 m dissolved oxygen saturation deviation from 100 percent on Lines 66.7 and 80.0 (Fig. 3.14a-b) shows that when upwelling occurs, the waters are undersaturated even during phytoplankton blooms. On Line 90.0, the dissolved oxygen at 10 m is supersaturated during the summer bloom but not during parts of the winter bloom (not shown), and the dissolved oxygen at 20 m is undersaturated during both summer and winter blooms (Fig. 3.14c). Net community production is not calculated from the glider data in the upwelling region due to the need to first quantify atmospheric sources and sinks of dissolved oxygen and quantify mixing.

One piece of evidence that suggests that primary production is important is that much of the top 100 m of the ocean on the three lines is found to be supersaturated in dissolved oxygen (Fig. 3.14 and Figs. 3.6c-3.8c). Causes of supersaturation of dissolved oxygen include heating of water faster than the equilibration of dissolved oxygen to the new temperature, vigorous mixing at the air-sea interface that injects bubbles into the subsurface ocean, and primary production due to phytoplankton. Seasonally, there may be undersaturation in winter as the water cools and can hold more dissolved oxygen and supersaturation in summer as the water warms and must release dissolved oxygen. The supersaturation signal at 100 m suggests a very well mixed upper 100 m or the presence of primary production.

In addition, the supersaturated waters at 10 m on Lines 66.7 and 80.0 and 20 m on Line 90.0 (Fig. 3.14) are adjacent to undersaturated waters due to upwelling, suggesting that horizontal mixing of dissolved oxygen may be important. If there is surface Ekman transport from the coast offshore on Lines 66.7 and 80.0, there must be horizontal mixing of the undersaturated water with the supersaturated water. The horizontal mixing would be another mechanism on top of vertical mixing, exchange with the atmosphere, and primary production that could affect the dissolved oxygen saturation at 10 m.

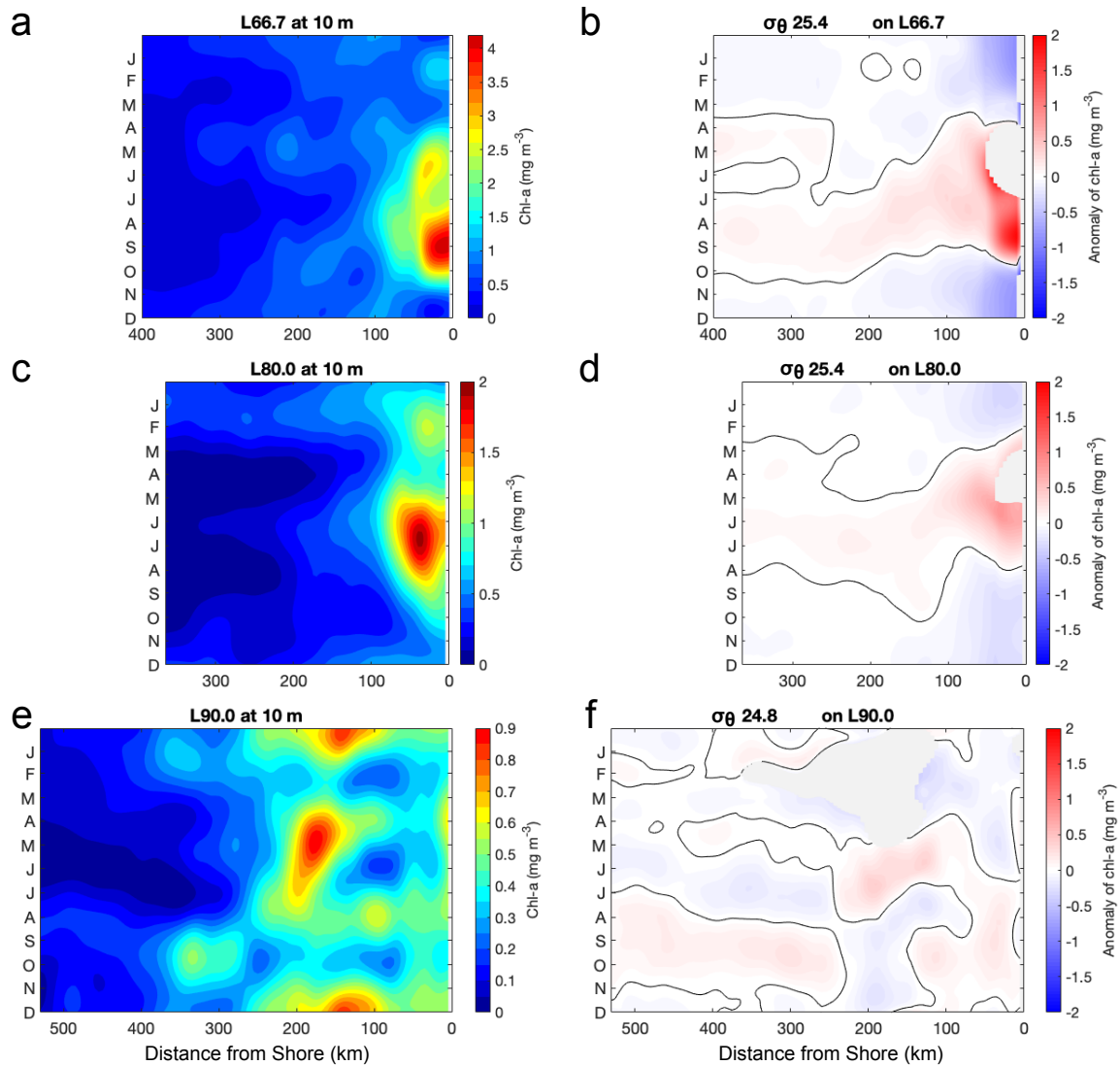


Figure 3.13 The annual cycle of chl-*a* concentration (mg m^{-3}) at 10 m and the chl-*a* anomaly (mg m^{-3}) from the annual mean on potential density surfaces. Chl-*a* at 10 m on (a) Line 66.7 (c) Line 80.0 and (e) Line 90.0. Chl-*a* anomaly on (b) Line 66.7 on 25.4 kg m^{-3} (d) Line 80.0 on 25.4 kg m^{-3} and (f) Line 90.0 on 24.8 kg m^{-3} .

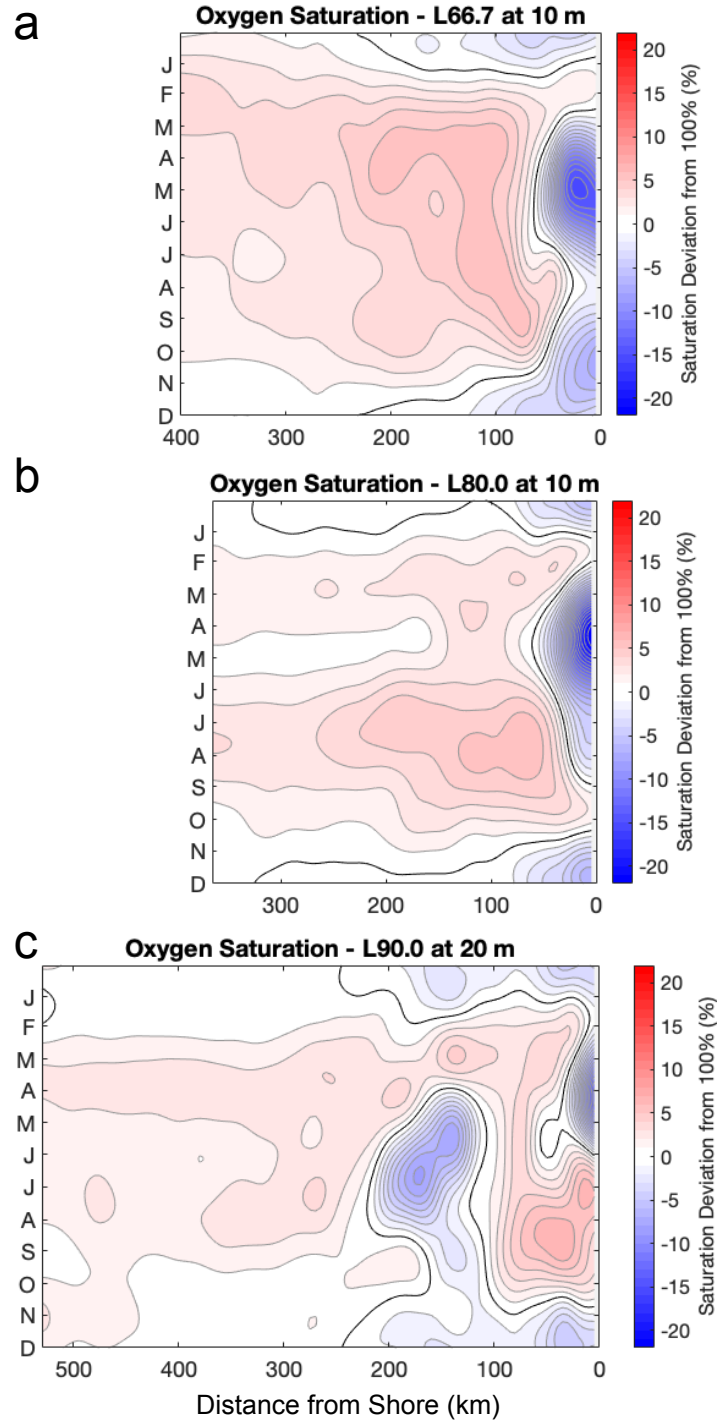


Figure 3.14 The annual cycle of oxygen saturation on (a) Line 66.7 at 10 m (b) Line 80.0 at 10 m and (c) Line 90.0 at 20 m. The oxygen saturation is reported as the deviation from 100 percent or full saturation, with positive (red) anomalies contouring supersaturation. Individual contours are 1 percent. Full saturation is outlined with a black contour.

The offshore dissolved oxygen annual cycle in the upper 200 m: Mixing, stratification, and primary production

The annual cycle of dissolved oxygen offshore of the coastal transition zone is different from the annual cycle inshore due to the presence of a subsurface dissolved oxygen maximum in the summer. Panels of the top 200 m of the ocean of potential temperature, dissolved oxygen, and chl-*a* show that there is increased solar heating and a deepening of the chl-*a* maximum in summer along with the formation of the subsurface dissolved oxygen maximum (Fig. 3.15). The solar heating causes increased surface stratification, indicated by the increased number of potential density surfaces in the upper 50 m from July through the end of October.

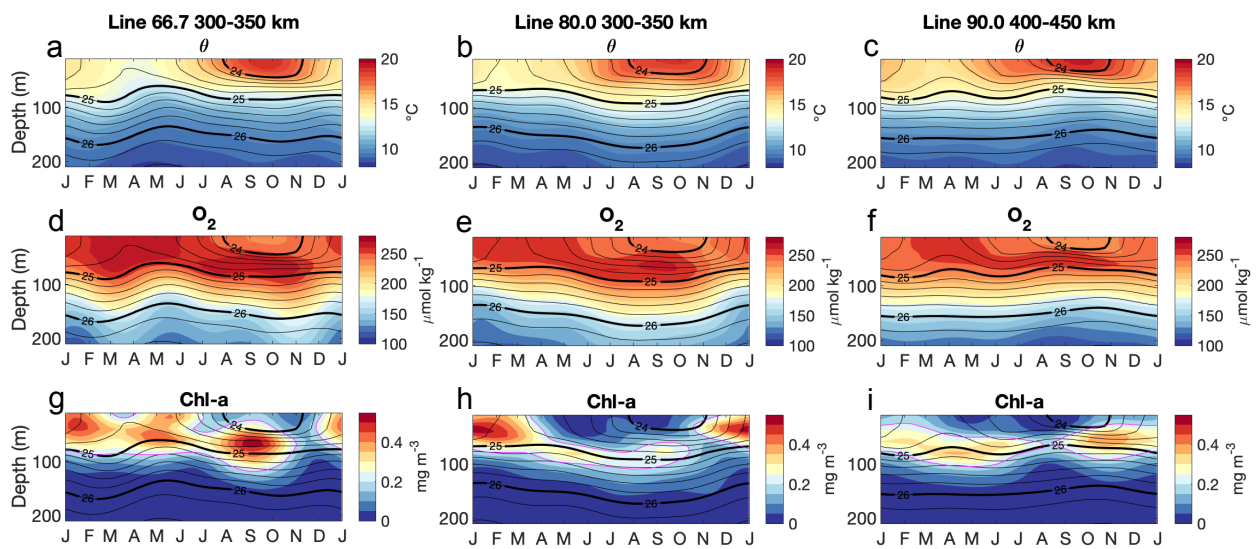


Figure 3.15 Plots of the upper 200 meters of the ocean showing the evolution of the summer subsurface dissolved oxygen maximum. (a-c) potential temperature ($^{\circ}\text{C}$) on Lines 66.7, 80.0, and 90.0 (d-f) dissolved oxygen concentration ($\mu\text{mol kg}^{-1}$) on Lines 66.7, 80.0, and 90.0 (g-i) chl-*a* concentration (mg m^{-3}) on Lines 66.7, 80.0, and 90.0. The annual cycle is averaged over the horizontal distance of 300-350 km from shore on Lines 66.7 and 80.0 and 400-450 km from shore on Line 90.0. A thin magenta line marks the 0.2 mg m^{-3} chl-*a* contour. Black lines mark potential density surfaces at 0.2 kg m^{-3} increments. Thick black lines mark σ_{θ} 24 kg m^{-3} , 25 kg m^{-3} , and 26 kg m^{-3} .

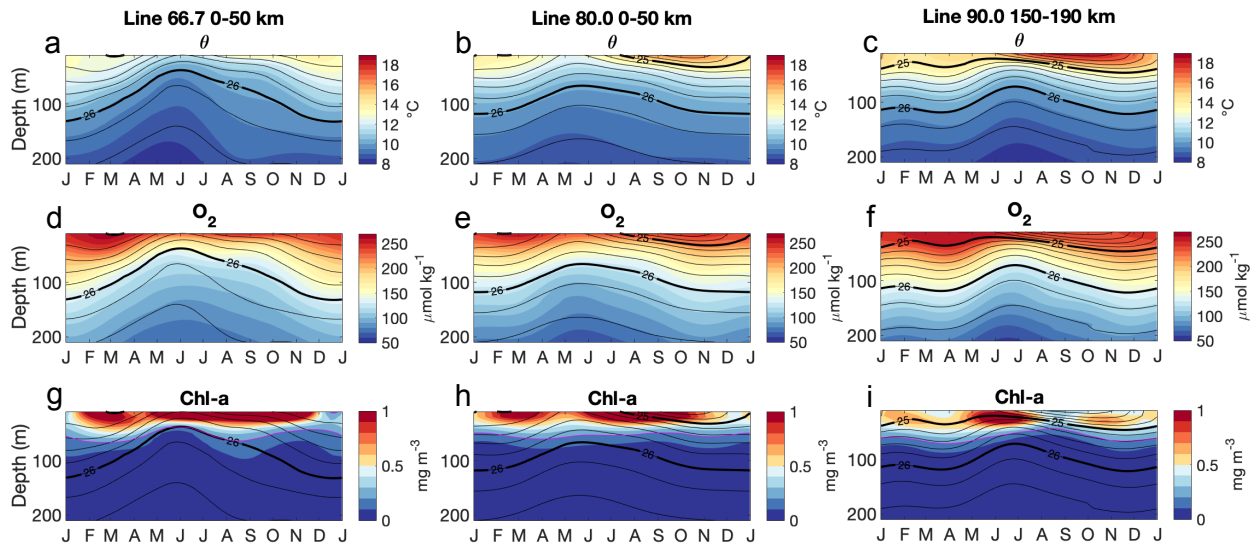


Figure 3.16 Plots of the upper 200 meters of the ocean in regions of strong seasonal upwelling. (a-c) potential temperature ($^{\circ}\text{C}$) on Lines 66.7, 80.0, and 90.0 (d-f) dissolved oxygen concentration ($\mu\text{mol kg}^{-1}$) on Lines 66.7, 80.0, and 90.0 (g-i) chl-*a* concentration (mg m^{-3}) on Lines 66.7, 80.0, and 90.0. The annual cycle is averaged over the horizontal distance of 0-50 km from shore on Lines 66.7 and 80.0 and 150-190 km on Line 90.0. A thin magenta line marks the 0.2 mg m^{-3} chl-*a* contour. Black lines mark potential density surfaces at 0.2 kg m^{-3} increments. Thick black lines mark σ_{θ} 25 kg m^{-3} , and 26 kg m^{-3} .

One hypothesis for the formation of the subsurface oxygen maximum is that a deep oxygenated mixed layer in the winter months is capped off by warmer surface waters that have lower full saturation dissolved oxygen concentrations in the summer (Reid, 1962). The increased stratification and lower dissolved oxygen concentration at the surface in summer and fall support this hypothesis. Within the subsurface dissolved oxygen maximum, the concentration of oxygen increases in July and August while the water is not in contact with the atmosphere. A hypothesis for the summer subsurface oxygen concentration increase is primary productivity of phytoplankton at the depth of the oxygen maximum, which has been observed in oligotrophic oceans (Riser & Johnson, 2008). The deepening of the chl-*a* maximum in summer so that its location corresponds to the depth of the subsurface dissolved oxygen maximum supports the hypothesis of primary productivity contributing to the subsurface oxygen concentration.

In regions of strong seasonal upwelling the dissolved oxygen and chl-*a* maximum are found at the surface year-round (Fig. 3.16). During periods of upwelling, isopycnals shoal towards the surface and bring lower potential temperature water and lower dissolved oxygen water to higher depths. The mechanisms of vertical advection and vertical mixing are examined with a 1-D vertical advection-diffusion numerical model to determine physical properties that account for the onshore-offshore difference in subsurface dissolved oxygen maximum formation. It is found that mixing from below easily erodes the subsurface dissolved oxygen maximum. In the 1-D idealized model, values of vertical diffusivity near molecular diffusion values of $1 \times 10^{-7} \text{ m}^2 \text{ s}^{-1}$ are prescribed beneath a moderately mixed ($K = 4 \times 10^{-3} \text{ m}^2 \text{ s}^{-1}$) surface layer to create conditions for the subsurface dissolved oxygen maximum to exist (Fig. 3.17). The model setup mimics having a mixed layer model with no vertical mixing between the surface layer and below. The dissolved oxygen annual cycles demonstrate that vertical mixing occurs inshore as isopycnals shoal due to upwelling (Figs. 3.9-3.11). Thus, while solar heating (Reid, 1962) is in effect both inshore and offshore, a difference in vertical mixing is one mechanism that determines whether a subsurface dissolved oxygen maximum in summer is formed.

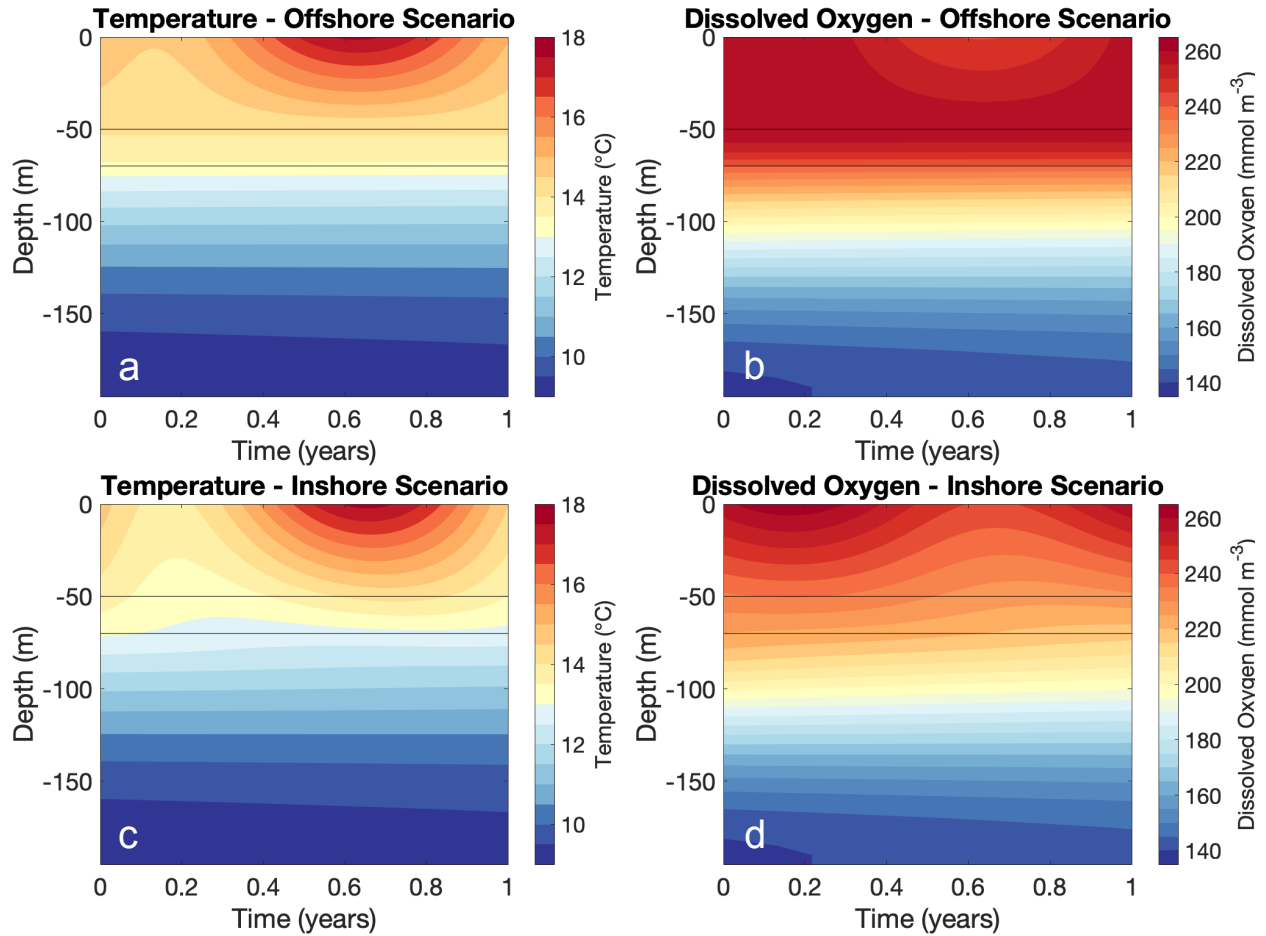


Figure 3.17 Modeled evolution of a year of temperature ($^{\circ}\text{C}$) and dissolved oxygen (mmol m^{-3}). The surface is forced with an annual cycle of heat flux. The vertical advection, w , and vertical diffusivity, κ , are constant through the year. The difference between offshore scenarios (a-b) and inshore scenarios (c-d) is the value of κ between 50 and 70 m. The offshore scenario is $w=0 \text{ m s}^{-1}$ and $\kappa=10^{-7} \text{ m}^2 \text{ s}^{-1}$, while the inshore scenario is $w=0 \text{ m s}^{-1}$ and $\kappa=10^{-4} \text{ m}^2 \text{ s}^{-1}$. From 0-50 m $w=0 \text{ m s}^{-1}$, and below 70 m $w=4 \text{ m year}^{-1}$ in both cases. From 0-50 m $\kappa=4 \times 10^{-3} \text{ m}^2 \text{ s}^{-1}$, and below 70 m $\kappa=1 \times 10^{-5} \text{ m}^2 \text{ s}^{-1}$ in both cases. Horizontal black lines mark 50 m and 70 m depth. A subsurface dissolved oxygen maximum is formed in the offshore scenario.

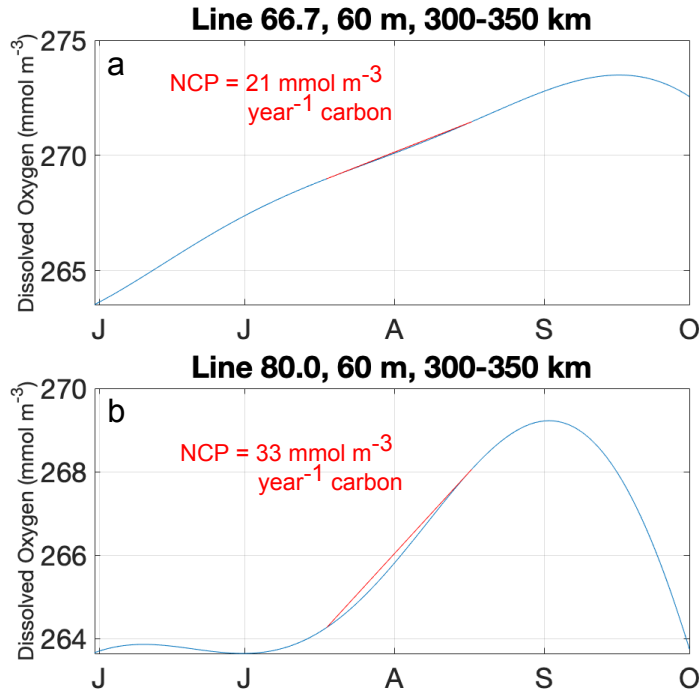


Figure 3.18 Summer dissolved oxygen increases within the subsurface oxygen maximum. The dissolved oxygen annual cycle at 60 m is plotted from June through September for (a) Line 66.7 and (b) Line 80.0. The annual cycle is averaged over 300-350 km from shore. The rate of change of dissolved oxygen is calculated over the red line. Net community production over the period in red is calculated using the ratio of 150 mol O₂ to 106 mol C.

On Lines 66.7 and 80.0, the concentration of dissolved oxygen in the subsurface dissolved oxygen maximum increases around potential density 24.5 kg m^{-3} (Fig. 3.15). The isopycnal 24.5 kg m^{-3} is isolated from the surface during the summer, which means the local maximum comes from a source of dissolved oxygen in the interior, and here the amount of net community production, the total primary productivity minus the community respiration, is quantified. Calculated from the increase in dissolved oxygen concentration at 60 m, the summer net community production rate is $21 \text{ mmol m}^{-3} \text{ year}^{-1} \text{ carbon}$ on Line 66.7 and $33 \text{ mmol m}^{-3} \text{ year}^{-1} \text{ carbon}$ on Line 80.0 (Fig. 3.18). The positive rate indicates that more primary production is occurring than community respiration, such that net carbon is being incorporated into marine biomass. The rate is calculated between mid-July and mid-August and represents the dissolved oxygen evolution in late summer. The net community production is not easily calculated over the offshore region in the other months due to physical processes such as vertical mixing

and interaction with the atmosphere at the ocean surface boundary likely being important. On Line 90.0, the increase in dissolved oxygen in the subsurface maximum in summer is not significant. The potential densities on which the subsurface dissolved oxygen maximum is found are lighter than the isopycnals that outcrop at the coast during upwelling. On isopycnals 24.5 kg m^{-3} and lighter on Lines 66.7 and 80.0, the subsurface maximum in concentration is found on isopycnal surfaces, which suggests that the maximum is not brought down from the surface, but forms in the subsurface.

The inshore dissolved oxygen annual cycle below 200 m: the upwelling cell, the California Undercurrent, and respiration

The hypoxic boundary shoals inshore in the annual mean, and the shallowest hypoxic waters are found near the coast on Lines 66.7 and 80.0 and near the Santa Rosa Ridge on Line 90.0 (Fig. 3.2). In addition, the hypoxic boundary has a seasonal evolution and is shallowest in spring on Lines 66.7 and 80.0 and in summer on Line 90.0 (Figs. 3.3-3.5). The depth of the hypoxic boundary is found beneath 200 m, so primary production should not be a factor. However, seasonal upwelling, seasonal variation of the California Undercurrent, and the upwelling cell circulation are physical mechanisms that could be important. Respiration is the biological mechanism that could significantly affect dissolved oxygen concentration. On isopycnal coordinates, the salinity anomaly from the annual mean is compared to the dissolved oxygen anomaly from the annual mean to determine if water masses can explain anomalies in dissolved oxygen. The depth anomaly from the annual mean of each isopycnal is also plotted to show the annual cycle of heave. The alongshore geostrophic velocity is compared to the dissolved oxygen anomaly to consider the effect of the California Undercurrent.

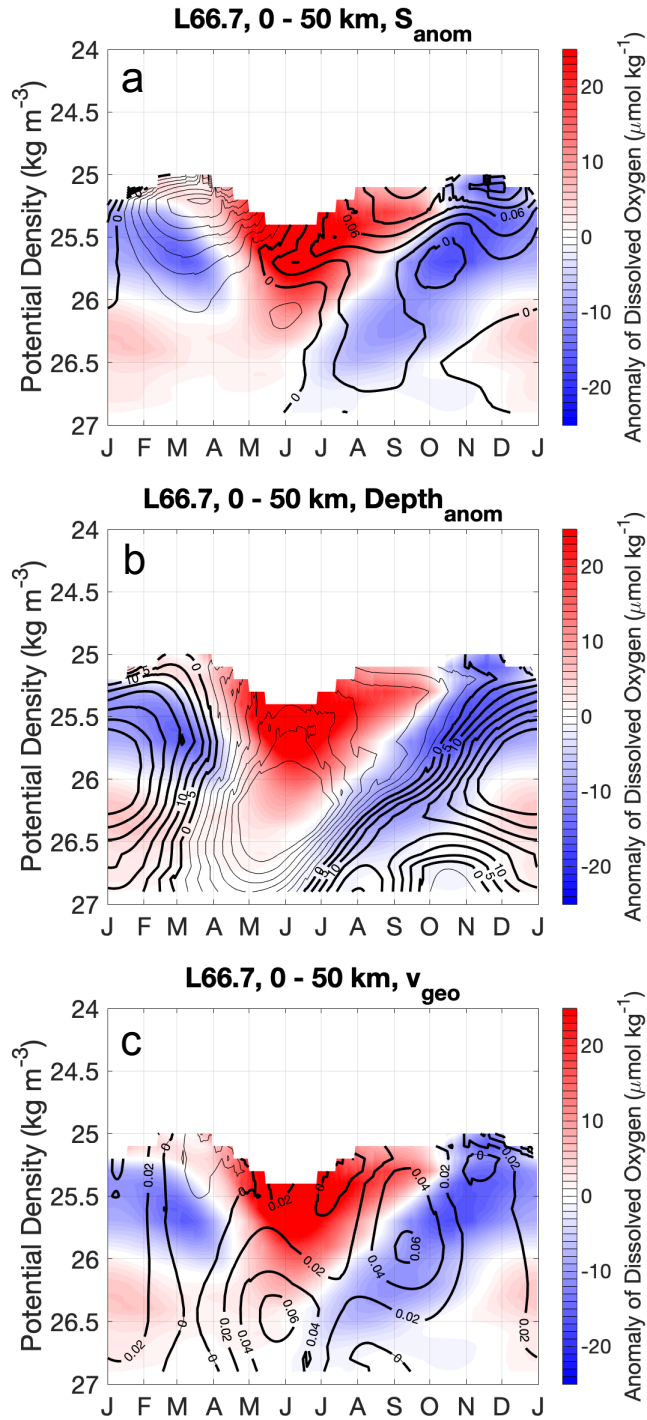


Figure 3.19 Anomaly of dissolved oxygen concentration (kg m^{-3}) from the annual mean in isopycnal coordinates on Line 66.7 with (a) contours of salinity anomaly from the annual mean (b) contours of depth anomaly (m) from the annual mean and (c) contours of alongshore geostrophic velocity (m s^{-1}) overlain. Data are averaged in the across-shore direction over 0-50 km. Dissolved oxygen is color-contoured and salinity anomaly, depth anomaly, and geostrophic velocity are contoured in black. Positive contours are drawn with a thick black line and labeled.

The pattern of dissolved oxygen anomaly on Line 66.7 appears to agree well with the pattern of depth anomaly (Fig. 3.19b). Shoaling isopycnals, indicated by negative depth anomalies, cause the surface isopycnals to become more oxygenated. During the peak shoaling in May and June, the salinity anomaly shows a two-layer pattern, with saltier water than the mean above 26 kg m^{-3} and fresher water than the mean below (Fig. 3.19a). This pattern has been hypothesized to indicate the upwelling cell, pulling offshore waters inshore below and inshore waters offshore above (Rudnick et al., 2017). Because the inshore water mass is saltier and lower in dissolved oxygen, the salinity anomaly and dissolved oxygen anomaly signal above 26 kg m^{-3} is not expected to result from the upwelling cell. Below 26 kg m^{-3} , fresher and more oxygenated water is found together. Depth of the isopycnal is the most important factor for the dissolved oxygen anomaly above 26 kg m^{-3} , while below 26 kg m^{-3} , water mass relationships hold. From June through October, while isopycnals are still higher in the water column than the mean, the dissolved oxygen anomaly on isopycnals switches from positive to negative, and this phenomenon is found throughout the water column. The decreasing dissolved oxygen on isopycnals may be due to respiration, vertical mixing, or increased influence from the California Undercurrent. The undercurrent velocity (Fig. 3.19c) shows a deeper core during upwelling and a shallower core in the late summer and early fall on Line 66.7, with a possible relationship to lower dissolved oxygen after the strongest poleward flow. The shoaling of the hypoxic boundary in spring during upwelling appears to be most strongly influenced by the shoaling of deep isopycnals, as along-isopycnal dissolved oxygen anomalies around 26.5 kg m^{-3} at that time are neutral or slightly positive.

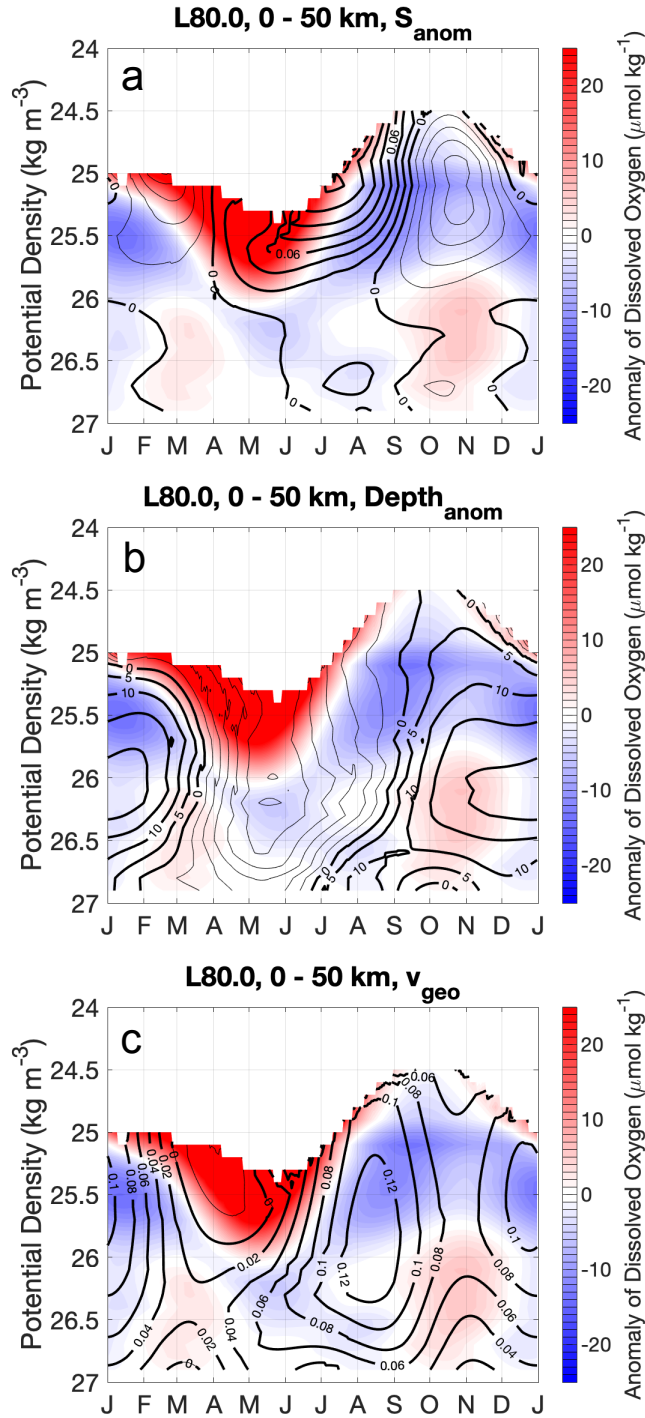


Figure 3.20 Anomaly of dissolved oxygen concentration (kg m^{-3}) from the annual mean in isopycnal coordinates on Line 80.0 with (a) contours of salinity anomaly from the annual mean (b) contours of depth anomaly (m) from the annual mean and (c) contours of alongshore geostrophic velocity (m s^{-1}) overlain. Data are averaged in the across-shore direction over 0-50 km. Dissolved oxygen is color-contoured and salinity anomaly, depth anomaly, and geostrophic velocity are contoured in black. Positive contours are drawn with a thick black line and labeled.

On Line 80.0, the sign of the anomaly of dissolved oxygen is different during upwelling above and below 26 kg m^{-3} , with a negative dissolved oxygen anomaly below 26 kg m^{-3} (Fig. 3.20). The isopycnals throughout the water column between April-June are higher in the water column than the annual mean (Fig. 3.20b). The salinity anomaly shows the signature of an upwelling cell. As on Line 66.7, the positive oxygen anomaly and positive salinity anomaly on near surface isopycnals is opposite to that expected from an inshore, saltier water mass. Unlike on Line 66.7, below 26 kg m^{-3} the higher dissolved oxygen and fresh anomaly is found only in March while from April-May lower dissolved oxygen is associated with a fresh anomaly, opposite to what is expected from an offshore, fresher more oxygenated water mass. Overall, the shoaling in spring (March-May) of the hypoxic boundary is dominated by isopycnal heave, as the along-isopycnal changes around 26.5 kg m^{-3} are less than $3 \mu\text{mol kg}^{-1}$, while the difference in dissolved oxygen concentration between 26.5 and 26.6 kg m^{-3} in the mean is over $10 \mu\text{mol kg}^{-1}$. In the summer months, the pattern of low dissolved oxygen anomaly on isopycnals is very pronounced (Fig. 3.20b) and occurs while isopycnals are still shallower than their annual mean depth, suggesting that respiration may be important. Other mechanisms include increased vertical mixing and horizontal advection of low-oxygen waters. Because the negative oxygen anomaly occurs in light isopycnals formed in the summer, it is likely that stratification is high. Looking at the alongshore geostrophic velocity on Line 80.0, poleward flow dominates year-round with only surface equatorward flow in the months of March and April (Fig. 3.20c). The cores of strongest poleward flow are in summer and winter, concurrent with the lowest anomalies in dissolved oxygen. The undercurrent and respiration may be more important on Line 80.0 than Line 66.7.

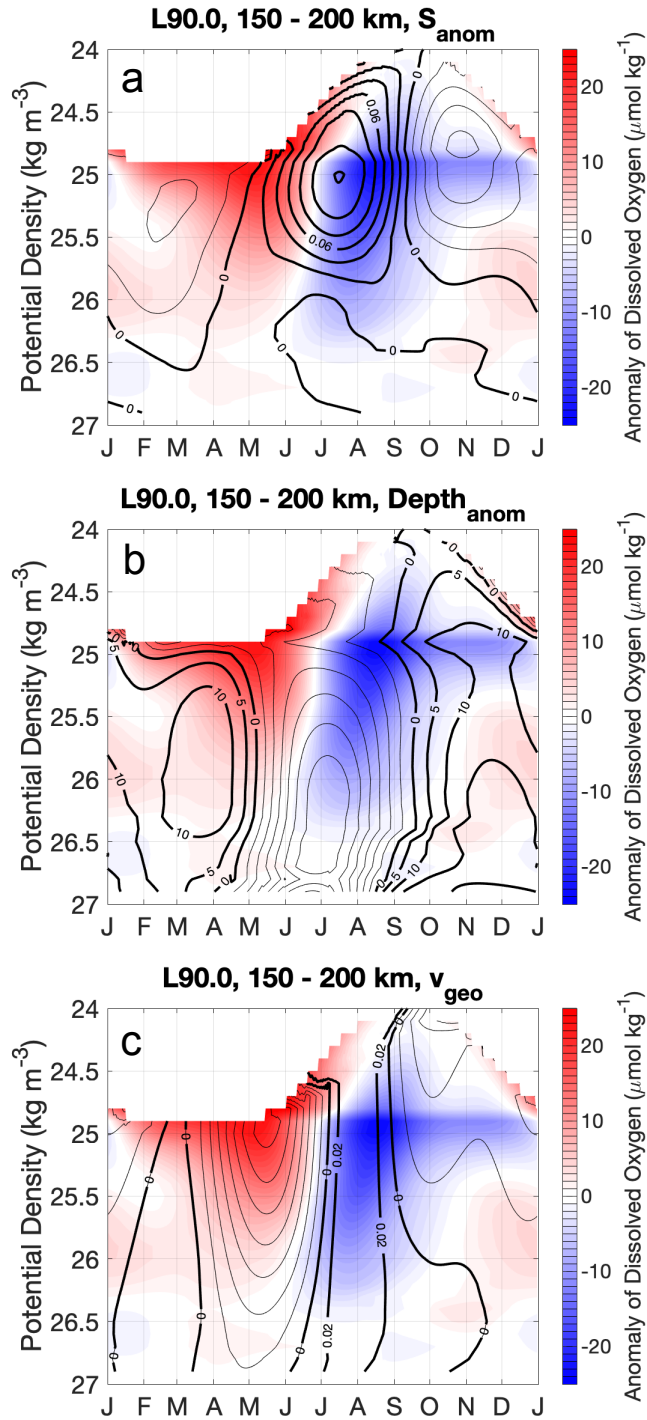


Figure 3.21 Anomaly of dissolved oxygen concentration (kg m^{-3}) from the annual mean in isopycnal coordinates on Line 90.0 with (a) contours of salinity anomaly from the annual mean (b) contours of depth anomaly (m) from the annual mean and (c) contours of alongshore geostrophic velocity (m s^{-1}) overlain. Data are averaged in the across-shore direction over 150-200 km. Dissolved oxygen is color-contoured and salinity anomaly, depth anomaly, and geostrophic velocity are contoured in black. Positive contours are drawn with a thick black line and labeled.

On Line 90.0, the region between 150-200 km from shore near the Santa Rosa Ridge is investigated because of the strong isopycnal shoaling that occurs there. In June and July, the strongest shoaling of isopycnals is found (Fig. 3.21b). At 26.5 kg m^{-3} and below, where the hypoxic boundary lies, the main contribution to the shoaling of the hypoxic boundary is shoaling of isopycnals. A high salinity anomaly occurs near the surface (Fig. 3.21a), which could be related to summer heating and evaporation as well as poleward flow that occurs throughout the water column in July (Fig. 3.21c). An upwelling cell pattern in salinity is not well defined over the Santa Rosa Ridge on Line 90.0. On isopycnals lighter than 26.5 kg m^{-3} in July and August, negative isopycnal dissolved oxygen anomalies are found on isopycnals that are higher than their annual mean depth. The negative dissolved oxygen anomalies on isopycnals in the summer are likely due to respiration or poleward flow advecting lower dissolved oxygen and saltier water to the area. Increased vertical mixing could also be an important mechanism, but because negative oxygen anomalies occur in stratified conditions in the summer, it is likely that respiration is important.

Discussion and Conclusions

The annual cycle of dissolved oxygen in the CCS presented describes the detailed evolution of dissolved oxygen in the top 500 m of the ocean and across horizontal gradients covering hundreds of kilometers. Upwelling is important to dissolved oxygen, causing low concentrations at the coast as isopycnals shoal and outcrop. The change in dissolved oxygen that occurs annually as part of the seasonal cycle due to upwelling is over $100 \text{ } \mu\text{mol kg}^{-1}$ at some depths and locations. Upwelling changes the concentration of dissolved oxygen near the surface and causes isopycnals below 200 m to shoal, which seasonally raises the $60 \text{ } \mu\text{mol kg}^{-1}$ dissolved oxygen contour, defined in this study as the hypoxic boundary. The seasonal change of the hypoxic boundary at the onset of upwelling is 40 m, and this is consistent across Lines 66.7, 80.0, and 90.0. Ventilation occurs along isopycnals that outcrop or approach the surface. Hundreds of kilometers away from the site of upwelling and beneath the mixed layer, a roughly $10 \text{ } \mu\text{mol kg}^{-1}$ positive anomaly in dissolved oxygen is found. Mixing occurs near the surface, and isopycnals that shoal seasonally due to upwelling are oxygenated by roughly $50 \text{ } \mu\text{mol kg}^{-1}$ when they are

within the top 50 m of the ocean surface. Primary production is likely important at the ocean surface, as the top 100 m of the ocean is found to be supersaturated in dissolved oxygen in the regions not affected by upwelling. However, net community production is difficult to quantify due to the importance of mixing and the atmospheric source and sink term near the surface. The region in which net community production is quantified here is the subsurface dissolved oxygen maximum that occurs offshore in the summer and fall. The near surface maximum is isolated from the atmosphere, and as suggested from a 1-D idealized model, vertical mixing from below is small. Low positive values of net community production are found on Lines 66.7 and 80.0 in the late summer and early fall, proving that there is primary production in those locations during that time.

Previous work in the CCS has focused on interannual variability with a focus on decreases in dissolved oxygen on the decadal timescale (Bograd et al., 2015; Bograd et al., 2008; Chavez et al., 2017; McClatchie et al., 2010; Ren et al., 2018). In the Pacific Ocean, the annual cycle of dissolved oxygen in the upper 500 m from WOA data found two different annual cycle patterns in the latitudinal band between 30N-42N; the annual cycle above 50 m had the greatest concentration in the spring and summer while the annual cycle at and below 125 m had the greatest concentration in late winter and early spring (Najjar & Keeling, 1997). The difference was attributed to deeper vertical mixing in the winter and greater respiration in the summer at and below 125 m and primary production being important in the spring and summer months in the upper 50 m (Najjar & Keeling, 1997). Here, upwelling near the coast impacts the dissolved oxygen annual cycle so that the lowest dissolved oxygen concentration is found in spring and summer in the regions with shoaling isopycnals (Fig. 3.22). In the coastal transition zone, the dissolved oxygen concentration at 10 m does have a maximum between late winter and summer, but in the offshore regions, the minimum in dissolved oxygen concentration is found in the summer and fall suggesting that the surface temperature seasonal cycle matters. Dissolved oxygen concentration at 10 m from WOA18 matches the annual cycle of the offshore region at 10 m (Fig. 3.23), but at grid points near the coast the WOA18 annual cycle differs from the CUGN observations in different ways depending on

the location along the coastline (not shown). The differences in the annual cycle calculations are likely due to the global calculation from WOA having fewer observations near the coast.

The high-resolution CCS annual cycle of dissolved oxygen resolves certain processes in more detail than previous studies, including the effects of vertical mixing and along-isopycnal property changes. Dissolved oxygen is a good tracer for vertical processes, as the vertical gradient of dissolved oxygen is high and as the surface dissolved oxygen concentration is forced towards its saturation concentration. As upwelling occurs, shoaling isopycnals are observed to increase in oxygen concentration and oxygen saturation, which suggests vertical mixing. Ventilation is also observed along isopycnals, with elevated dissolved oxygen on an isopycnal after it has ceased to outcrop. With respect to offshore of the upwelling dominated region, the subsurface dissolved oxygen maximum evolution is well observed on Lines 66.7 and 80.0, and its existence suggests that there is lower vertical mixing in that region during that time. Lower vertical mixing offshore and higher vertical mixing inshore agrees with general concepts of more nutrient availability found in upwelling-dominated regions and less nutrient availability found in oligotrophic regions, where nutrients are a tracer for water below the mixed layer. The oxygen observations suggest the presence or absence of mixing but are unable to quantify rates of mixing due to unknown quantities of source and sink terms.

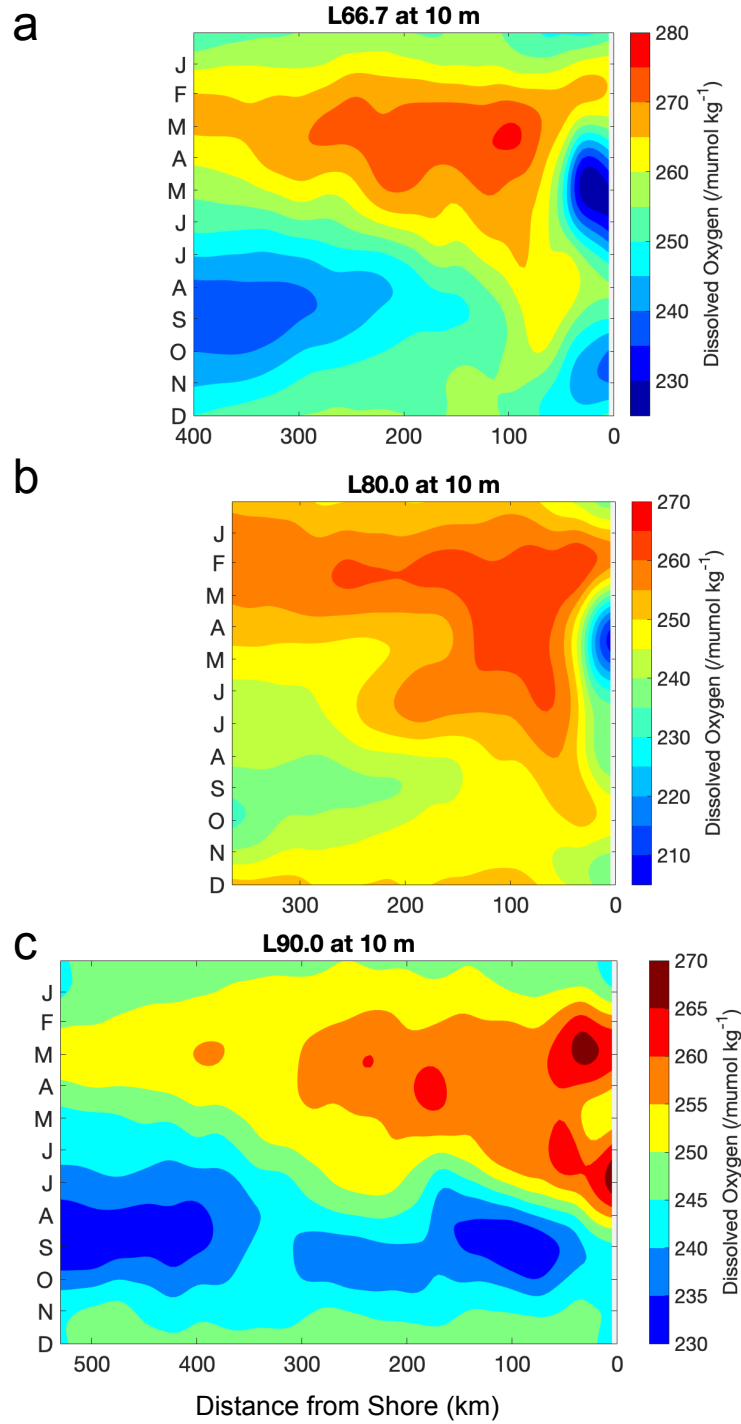


Figure 3.22 Dissolved oxygen concentration ($\mu\text{mol kg}^{-1}$) annual cycle at 10 m depth. (a) Line 66.7 (b) Line 80.0 and (c) Line 90.0.

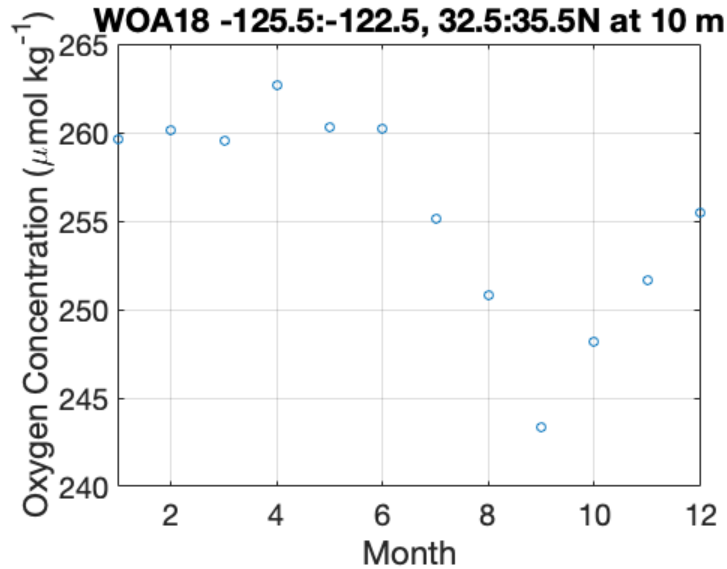


Figure 3.23 The annual cycle of dissolved oxygen concentration from World Ocean Atlas 2018 (WOA18) at 10 m. Values were averaged over 125.5-122.5 W and 32.5-35.5 N. WOA18 monthly values are calculated from objective analysis on a $1^\circ \times 1^\circ$ grid.

The annual cycle suggests important mechanisms for large signals such as the change in dissolved oxygen concentration during upwelling, which is mainly due to heaving isopycnals. However, other more subtle features of the dissolved oxygen annual cycle will need further investigation, and numerical modeling may be able to quantify the combination of mechanisms at work to produce a feature of the annual cycle. For example, along-isopycnal changes from 0-50 km in dissolved oxygen are difficult to explain and may be due to biological sources and sinks, mixing, and horizontal advection by the California Undercurrent. The annual cycle presented may also serve as a benchmark for numerical models to reproduce a realistic ocean. The annual cycle of dissolved oxygen here includes the annual cycle of horizontal and vertical gradients in dissolved oxygen, which provide important information for tuning a regional numerical model. The path forward may be evaluation of observations and realistic or assimilating numerical models to calculate budgets of dissolved oxygen concentration.

The annual cycle is the first step towards understanding interannual changes in dissolved oxygen. Mechanistically, there are a few phenomena that are somewhat surprising with respect to predicted changes in the CCS due to global warming. The first considers the prediction of increased stratification in

the oceans. In the offshore regions, the subsurface dissolved oxygen maximum in summer and fall relies on strong stratification, so increased stratification in summer and fall could capture more dissolved oxygen in the subsurface layer and oxygenate the upper ocean. Second, it has been hypothesized that global warming will cause stronger winds and thus stronger upwelling. While hypoxic levels of oxygen would be found at shallower depths due to increased isopycnal heave, increased numbers of deep isopycnals will also outcrop at the surface. As observed here, water that approaches the ocean surface is oxygenated, which suggests that deeper isopycnals will be ventilated in the stronger upwelling scenario, oxygenating the upper ocean. Both scenarios oxygenate a portion of the ocean water column, while much of the modeling research on global warming has focused on deoxygenation. These and other mechanisms remain to be evaluated as the interannual variability of dissolved oxygen in the CCS is studied.

Chapter 3, in full, is being prepared for submission for publication of the material as it currently appears in: Ren, A.S. and Rudnick, D.L. The annual cycle of dissolved oxygen from high-resolution glider observations in the California Current System. *Progress in Oceanography*. The dissertation author was the primary investigator and author of this paper.

References

- Anderson, L. A. (1995). On the hydrogen and oxygen content of marine phytoplankton. *Deep Sea Research Part I: Oceanographic Research Papers*, 42(9), 1675-1680. [https://doi.org/https://doi.org/10.1016/0967-0637\(95\)00072-E](https://doi.org/https://doi.org/10.1016/0967-0637(95)00072-E)
- Bograd, S. J., Buil, M. P., Lorenzo, E. D., Castro, C. G., Schroeder, I. D., Goericke, R., Anderson, C. R., Benitez-Nelson, C., & Whitney, F. A. (2015). Changes in source waters to the Southern California Bight. *Deep Sea Research Part II: Topical Studies in Oceanography*, 112, 42-52. <https://doi.org/https://doi.org/10.1016/j.dsr2.2014.04.009>
- Bograd, S. J., Castro, C. G., Di Lorenzo, E., Palacios, D. M., Bailey, H., Gilly, W., & Chavez, F. P. (2008). Oxygen declines and the shoaling of the hypoxic boundary in the California Current. *Geophysical Research Letters*, 35(12). <https://doi.org/https://doi.org/10.1029/2008GL034185>
- Bograd, S. J., Chereskin, T. K., & Roemmich, D. (2001). Transport of mass, heat, salt, and nutrients in the southern California Current System: Annual cycle and interannual variability. *Journal of Geophysical Research: Oceans*, 106(C5), 9255-9275. <https://doi.org/https://doi.org/10.1029/1999JC000165>
- Brink, K. H., & Cowles, T. J. (1991). The Coastal Transition Zone program. *Journal of Geophysical Research: Oceans*, 96(C8), 14637-14647. <https://doi.org/https://doi.org/10.1029/91JC01206>
- Carpenter, W. L. (1873). Appendix A - Summary of the Results of the Examination of Samples of Seawater taken at the Surface and at various Depths. In C. W. Thomson (Ed.), *The Depths of the Sea: An Account of the General Results of the Dredging Cruises of H.M.S.S. 'Porcupine' and 'Lightning' during the summers of 1868, 1869, and 1870*. Macmillan and Co.
- Chavez, F. P., Pennington, J. T., Castro, C. G., Ryan, J. P., Michisaki, R. P., Schlining, B., Walz, P., Buck, K. R., McFadyen, A., & Collins, C. A. (2002). Biological and chemical consequences of the 1997–1998 El Niño in central California waters. *Progress in Oceanography*, 54(1), 205-232. [https://doi.org/10.1016/S0079-6611\(02\)00050-2](https://doi.org/10.1016/S0079-6611(02)00050-2)
- Chavez, F. P., Pennington, J. T., Michisaki, R. P., Blum, M., Chavez, G. M., Friederich, J., Jones, B., Herlien, R., Kieft, B., Hobson, B., Ren, A. S., Ryan, J., Sevdjian, J. C., Wahl, C., Walz, K. R., Yamahara, K., Friederich, G. E., & Messié, M. (2017). Climate Variability and Change: Response of a Coastal Ocean Ecosystem. *Oceanography*, 30(4), 128-145. <http://www.jstor.org/stable/26367631>
- Cushman-Roisin, B., & Beckers, J.-M. (2011). *Introduction to geophysical fluid dynamics: physical and numerical aspects* (Vol. 101). Academic Press.
- Davis, J. C. (1975). Minimal Dissolved Oxygen Requirements of Aquatic Life with Emphasis on Canadian Species: a Review. *Journal of the Fisheries Research Board of Canada*, 32(12), 2295-2332. <https://doi.org/10.1139/f75-268>
- Dittmar, W. (1884). Report on Researches into the Composition of Ocean-Water, collected by H.M.H. Challenger, during the years 1873-1876. In J. Murray & C. W. Thomson (Eds.), *Report on the Scientific Results of the Voyage of H.M.S. Challenger during the years 1873-76, Physics and Chemistry* (Vol. 1).

- Garcia, H. E., Boyer, T. P., Baranova, O. K., Locarnini, R. A., Mishonov, A. V., Grodsky, A., Paver, C. R., Weathers, K. W., Smolyar, I. V., Reagan, J. R., Seidov, D., & Zweng, M. M. (2019). *World Ocean Atlas 2018: Product Documentation*.
- Garcia, H. E., Weathers, K. W., Paver, C. R., Smolyar, I. V., Boyer, T. P., Locarnini, R. A., Zweng, M. M., Mishonov, A. V., Baranova, O. K., Seidov, D., & Reagan, J. R. (2019). World Ocean Atlas 2018, Volume 3: Dissolved Oxygen, Apparent Oxygen Utilization, and Dissolved Oxygen Saturation. In A. Mishonov (Ed.), *NOAA Atlas NESDIS* (Vol. 83, pp. 38).
- Johnston, T. M. S., & Rudnick, D. L. (2015). Trapped diurnal internal tides, propagating semidiurnal internal tides, and mixing estimates in the California Current System from sustained glider observations, 2006–2012. *Deep Sea Research Part II: Topical Studies in Oceanography*, 112, 61-78. <https://doi.org/https://doi.org/10.1016/j.dsr2.2014.03.009>
- McClatchie, S. (2014). The CalCOFI Sampling Domain. In *Regional Fisheries Oceanography of the California Current System: The CalCOFI program* (pp. 8-11). Springer Netherlands.
- McClatchie, S., Goericke, R., Cosgrove, R., Auad, G., & Vetter, R. (2010). Oxygen in the Southern California Bight: Multidecadal trends and implications for demersal fisheries. *Geophysical Research Letters*, 37(19). <https://doi.org/https://doi.org/10.1029/2010GL044497>
- Munk, W. H. (1966). Abyssal recipes. *Deep Sea Research and Oceanographic Abstracts*, 13(4), 707-730. [https://doi.org/https://doi.org/10.1016/0011-7471\(66\)90602-4](https://doi.org/https://doi.org/10.1016/0011-7471(66)90602-4)
- Najjar, R. G., & Keeling, R. F. (1997). Analysis of the mean annual cycle of the dissolved oxygen anomaly in the World Ocean. *Journal of Marine Research*, 55(1), 117-151. <https://doi.org/10.1357/0022240973224481>
- Ohman, M. D., Barbeau, K., Franks, P. J., Goericke, R., Landry, M. R., & Miller, A. J. (2013). Ecological transitions in a coastal upwelling ecosystem. *Oceanography*, 26(3), 210-219.
- Reid, J. L. (1962). Distribution of Dissolved Oxygen in the Summer Thermocline. *Journal of Marine Research*, 20(2), 138-148.
- Ren, A. S., Chai, F., Xue, H., Anderson, D. M., & Chavez, F. P. (2018). A Sixteen-year Decline in Dissolved Oxygen in the Central California Current. *Scientific Reports*, 8(1), 7290. <https://doi.org/10.1038/s41598-018-25341-8>
- Riser, S. C., & Johnson, K. S. (2008). Net production of oxygen in the subtropical ocean. *Nature*, 451(7176), 323-325.
- Rudnick, D. L., Davis, R. E., Eriksen, C. C., Fratantoni, D. M., & Perry, M. J. (2004). Underwater Gliders for Ocean Research. *Marine Technology Society Journal*, 38(2), 73-84. <https://doi.org/10.4031/002533204787522703>
- Rudnick, D. L., Sherman, J. T., & Wu, A. P. (2018). Depth-Average Velocity from Spray Underwater Gliders. *Journal of Atmospheric and Oceanic Technology*, 35(8), 1665-1673. <https://doi.org/10.1175/JTECH-D-17-0200.1>

Rudnick, D. L., Zaba, K. D., Todd, R. E., & Davis, R. E. (2017). A climatology of the California Current System from a network of underwater gliders. *Progress in Oceanography*, 154, 64-106.
<https://doi.org/10.1016/j.pocean.2017.03.002>

Vaquer-Sunyer, R., & Duarte, C. M. (2008). Thresholds of hypoxia for marine biodiversity. *Proceedings of the National Academy of Sciences*, 105(40), 15452-15457.
<https://doi.org/doi:10.1073/pnas.0803833105>

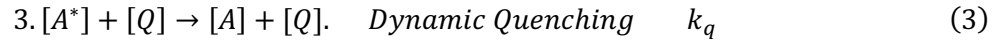
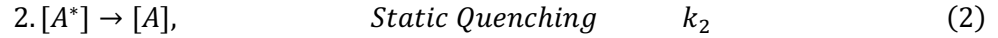
CHAPTER 4: Drift characteristics of Sea-Bird dissolved oxygen optode sensors

Introduction

The California Underwater Glider Network (CUGN) is a long-term monitoring glider network started in 2007 with currently over 14 years of temperature, salinity, and velocity data on regularly sampled transects in the California Current System (CCS). Since 2017, gliders have carried a Seabird 63 optode dissolved oxygen sensor as part of their payload. Since dissolved oxygen sensors are known to drift after calibration, it is desirable to have a correction or calibration procedure in place while collecting observations. We present a two-point correction procedure and measurements of instrument drift over 5 years on 14 Sea-Bird SBE63 optode sensors used on gliders. The novelty of this study is having many measurements of drift during 3-4 month deployments and during 3-4 months of dry storage. Our record of calibrations of SBE63 sensors adds to a growing literature of assessments of oxygen sensors including Aanderaa optodes (Bittig & Körtzinger, 2015; Bittig, Körtzinger, Neill, et al., 2018; Bushinsky et al., 2016; Johnson et al., 2015; Körtzinger et al., 2005). The suggested correction procedure provides dissolved oxygen data with accuracy of the larger of 0.6% or $0.5 \mu\text{mol kg}^{-1}$ and is necessary for any dissolved oxygen sensor in use more than 6 months after calibration. Uncorrected sensors read increasingly lower oxygen values over time, requiring an upward adjustment in gain to yield the best measurements.

The SBE63 uses the same principle as the Aanderaa optode, and the two brands of sensors use the organo-metallic molecule platinum porphyrin as the luminophore and the same material for the sensor membrane (Bittig, Körtzinger, Neill, et al., 2018), though details in the engineering or manufacturing process may differ. The sensor luminophore is excited after exposure to light and releases energy through fluorescence. An excited molecule can return to its original energy state in one of three ways: 1) it can emit a photon in a radiative process of fluorescence or phosphorescence 2) it can release energy through non-radiative means collectively termed static quenching and 3) it can collide with other molecules and transfer energy in a non-radiative process called dynamic quenching. Dynamic quenching occurs for

platinum porphyrin in the presence of oxygen. Given excited molecules $[A^*]$, lowered energy state molecules $[A]$, photons of light $h\nu$, and quenching molecules $[Q]$, processes 1-3 occur at rates k_1 , k_2 , and k_q assumed to be constants (Demas et al., 1999):



In this paper, the $[Q]$ is the concentration of oxygen, and k_q is the bimolecular quenching constant for oxygen. For natural rate of decay without dynamic quenching, the rate of change is

$$\frac{d[A^*]}{dt} = -k_1[A^*] - k_2[A^*] = -(k_1 + k_2)[A^*]. \quad (4)$$

With dynamic quenching, the rate of change is

$$\frac{d[A^*]}{dt} = -(k_1 + k_2 + k_q[Q])[A^*], \quad (5)$$

where quenching increases as the concentration of the quenching molecule increases. The timescale of decay, or the fluorescence lifetime for natural decay L_0 is

$$L_0 = \frac{1}{k_1 + k_2}, \quad (6)$$

and with quenching the fluorescence lifetime L_q is

$$L_q = \frac{1}{k_1 + k_2 + k_q[Q]}. \quad (7)$$

The ratio of the original decay timescale to the decay timescale with quenching is

$$\frac{L_0}{L_q} = 1 + k_q L_0 [Q]. \quad (8)$$

Equation 8 is also known as the Stern-Volmer equation when written with the constant k_{sv} :

$$\frac{L_0}{L_q} = 1 + k_{sv}[Q]. \quad (9)$$

The concentration of oxygen, $[Q] = [O_2]$, causes a decreased fluorescence lifetime of the platinum porphyrin molecule in the SBE63 optode theoretically at the rate proportional to k_{sv} . Thus, deviations in

fluorescence from an oxygenated to non-oxygenated environment can be measured and converted into the concentration of dissolved oxygen present.

Given the bimolecular quenching constant, k_q , at a given temperature the Stern-Volmer equation should be linear. However in optodes k_{sv} changes its value for high $[O_2]$, which suggests that some of the luminophore in the membrane is inaccessible to oxygen in high $[O_2]$ environments (Johnson et al., 2015), so in optodes an empirical model is used. Calibration coefficients are developed for each sensor that span a range of conditions in temperature and dissolved oxygen concentration. The relationship between phase delay of a sinusoidally modulated excitation and $[O_2]$ is more reliable than measurements of the fluorescence lifetime, and the phase delay relationship is used. Phase delay and fluorescence lifetime are related by

$$\tan \phi = 2\pi f * L \quad (10)$$

where f is the modulated frequency of the excitation light source in Hz, ϕ is the phase delay, and L is a general decay timescale or fluorescence lifetime (Demas et al., 1999). The SBE63 empirical model is based on work by Uchida et al. (2008) and relates oxygen concentration to phase delay:

$$[O_2] = \left[\frac{\frac{(a_0 + a_1 T + a_2 V^2)}{(b_0 + b_1 V)} - 1}{K_{sv}} \right] [S_{corr}] [P_{corr}]. \quad (10)$$

V is the phase delay in volts, T is temperature in °C, and a_0 , a_1 , a_2 , b_0 , b_1 , and K_{sv} are calibration coefficients or are determined by calibration coefficients (Sea-Bird, 2017). The dissolved oxygen concentration, $[O_2]$, is reported in ml l⁻¹. Corrections to account for the salinity of seawater, S_{corr} , and the pressure, P_{corr} , are also included (Sea-Bird, 2017).

The concern in this paper is the time drift of the coefficients in the model relating $[O_2]$ and the phase delay ϕ , which has been documented (Bittig & Körtzinger, 2015; Bittig, Körtzinger, Neill, et al., 2018) to change the measured oxygen concentration on the order of 10% on the timescale of years. The time drift can be periodically recorded and corrected with a gain and offset correction calculated from a

two-point calibration with an $[O_2]$ observation at full saturation and zero saturation (Bittig, Körtzinger, Neill, et al., 2018),

$$[O_2]_{corr} = G * [O_2]_{raw} + Z, \quad (11)$$

where G is the gain, Z is the offset, and the subscripts indicate the raw or corrected (*corr*) dissolved oxygen concentration values. The recommended best practice is to use a 2-point correction (Bittig, Körtzinger, Neill, et al., 2018) in between periodic full sensor calibrations that span a range of temperatures and dissolved oxygen concentrations.

While optodes have been used on gliders before (Alkire et al., 2014; Damerell et al., 2016; Haskell II et al., 2019; Howatt et al., 2018; Hull et al., 2021; Nicholson et al., 2008; Nicholson & Feen, 2017; Nicholson et al., 2015; Pelland et al., 2018; Pietri & Karstensen, 2018; Pizarro et al., 2016; Schütte et al., 2016), this study presents data from optodes used regularly as part of a monitoring program for the CCS. The SBE63s are evaluated roughly every 4 months. The intervals between evaluations are either while the glider is deployed in the ocean or when the glider is on land in the lab being prepared for the next deployment. Based on the literature, it is unclear whether there is a difference in the drift rate of optodes while stored or while deployed in the ocean, though studies suggest that the drift that occurs during deployment is smaller than the drift during storage (Bittig, Körtzinger, Neill, et al., 2018). One goal for this study is to compare drift rates while deployed and while in dry storage, and the novelty of the study is that sensors are corrected repeatedly after short deployments and short periods of storage.

Because of the glider deployment schedule in CUGN and because any calibration and correction protocol implemented would be performed with high repetition, a few relatively simple ways to undertake the measurements needed for the correction are assessed. By focusing on a relatively simple procedure, it enables engineers, technicians, and general oceanographers to do the correction with accuracy. The full saturation reading of the optode is undertaken with an in-air method and an in-water method. The results from both methods are compared for precision. The reading of the optode at zero is generally difficult to obtain because an environment with zero oxygen is challenging to set up. We choose to evaluate a chemical means of creating a zero-oxygen environment with a sodium sulfite solution. We focus on the

laboratory procedures, but dissolved oxygen can be corrected by comparison with hydrographic bottle samples. To evaluate, comparison to California Cooperative Fisheries Investigations (CalCOFI) hydrographic bottle samples of dissolved oxygen is performed, and the benefits and costs of the various methods are discussed. We conclude that laboratory measurements may be more precise and accurate than many ocean comparisons.

Overall, the drift of the SBE63s over 5 years is described, whether stored in air or deployed in the ocean, and suggestions for procedures to periodically correct for dissolved oxygen drift are provided.

Materials & Methods

The SBE63 optodes are deployed on gliders. Gliders are autonomous underwater vehicles that profile vertically using changes in buoyancy and move horizontally using wings and through internally shifting their center of mass (Rudnick, 2016). The gliders used in this study are Spray gliders (Sherman et al., 2001) operating as part of the California Underwater Glider Network (CUGN) in the central and southern California Current System (CCS). The gliders provide continuous coverage on 300-500 km onshore-offshore transects; a single glider mission is around 100 days at which point the glider is recovered and another glider is deployed in its place (Rudnick et al., 2017). Glider dives are to 500 m depth and individual dives are 3 hours and 3 km apart. A pumped flow system ensures reliable flow over sensors on the glider which include a conductivity-temperature-depth (CTD) sensor, a fluorometer, and a dissolved oxygen SBE63 optode sensor.

The routine operation of gliders in CUGN involves a roughly 100-day mission followed by a roughly 100-day storage period during which the glider is serviced. Sensor drift is measured before and after glider missions. Evidence suggests that glider drift can be detected within weeks of calibration (Bittig, Körtzinger, Neill, et al., 2018; Bushinsky et al., 2016), so drift observations were collected within one month of glider deployment or recovery, with the vast majority of measurements occurring within two weeks. Readings outside the one-month period are treated as “test” drift observations and included in some of the subsequent analysis. The reading before deployment is the “pre” deployment observation, and the reading after deployment is the “post” deployment observation.

Measurements of Optodes at Full Saturation

The two-point correction is determined with two assessments of the optode dissolved oxygen concentration against a known standard, and one of the assessments is at full saturation, or the amount of dissolved oxygen found in water at equilibrium with the atmosphere. The full saturation concentration of dissolved oxygen is calculated using the formula of Garcia and Gordon (1992) equation 8 using coefficients fit to data from Benson and Krause Jr. (1984). The equation 8 in Garcia and Gordon (1992) is well-known to have a typo, and the corrected equation is reproduced here for clarity:

$$[O_2^*(T, S)] = e^{A_0 + A_1 T_s + A_2 T_s^2 + A_3 T_s^3 + A_4 T_s^4 + A_5 T_s^5 + B_0 S + S*(B_1 T_s + B_2 T_s^2 + B_3 T_s^3) + C_0 S^2} \quad (12)$$

where $[O_2^*(T, S)]$ is the full saturation concentration of dissolved oxygen at 1 atm in ml l^{-1} , T_s is a scaled temperature defined in Garcia and Gordon (1992), S is the salinity, and the remaining variables are constants defined in Garcia and Gordon (1992). In addition, the equation is corrected to account for differences in atmospheric pressure using a slightly modified version of the pressure correction term suggested in Benson and Krause Jr. (1984) equation 24:

$$P_f = \frac{(P - p_{H_2O} * R) * (1 - \theta_o P)}{(1 - p_{H_2O} * R) * (1 - \theta_o)} \quad (13)$$

where P_f is the correction term, P is the measured atmospheric pressure in atm, p_{H_2O} is the water vapor pressure in atm, and θ_o is the 2nd virial coefficient of oxygen gas. R is the relative humidity of the atmosphere. R is 1 when the optode is used in water but can be less than 1 when the optode is making a measurement in air. The water vapor pressure is calculated using equation 10 in Weiss and Price (1980). The 2nd virial coefficient is calculated using the empirical relationship in Benson and Krause Jr. (1984) Table 2. Neglecting the terms containing the 2nd virial coefficient which describe the non-ideal behavior of gas, the P_f becomes very similar to the pressure correction suggested for oxygen measured on biogeochemical Argo floats (Bittig, Körtzinger, Johnson, et al., 2018). The concentration at full saturation of dissolved oxygen including the atmospheric pressure correction is

$$[O_2^*(T, S, P)] = [O_2^*(T, S)] * P_f . \quad (14)$$

The full saturation concentration is compared to the concentration of dissolved oxygen measured by the SBE63, $[O_2]$, to calculate the saturation of dissolved oxygen.

$$\text{sat}(O_2) = \frac{[O_2]}{[O_2^*(T, S, P)]}, \quad (15)$$

where $\text{sat}(O_2)$ is the oxygen saturation described as a ratio where a value of 1 is full or 100% saturation.

Full saturation conditions are achieved in water by using an air bubbler in a beaker of fresh water. 700 mL of water are used which covers the SBE63 while in a 2000 mL glass beaker. The air bubbler is a type that can be found for sale for use in fish tanks and an aquarium stone is attached to the pump to generate small air bubbles. The measurement at full saturation is performed at room temperature. A room with stable temperature is needed to ensure that the water is at room temperature and that the water is not changing temperature during the readings for the full saturation endpoint. A beaker of 700 mL of water will usually equilibrate to room temperature within a few hours. The average of dissolved oxygen concentrations taken every 10 seconds for a 5-minute period is used as one full saturation endpoint measurement. Full saturation conditions always exist in air, and the second method of a full saturation endpoint determination is to read the optode while exposed to air. The average of dissolved oxygen concentrations taken every 10 seconds for a 5-minute period is used as one full saturation endpoint measurement.

The parameters recorded from both in-water and in-air full saturation readings include the atmospheric pressure, the temperature of the water or air, and the relative humidity. The atmospheric pressure is taken from a local weather station or a sensor at Scripps pier. The pressure reading from the sensor at Scripps pier is adjusted for the height of the glider laboratory from sea level, roughly 67 meters. The temperature of the water or air is recorded by the SBE63. The relative humidity is estimated from a local weather station or a humidity sensor in the glider laboratory. The relative humidity is set to 1 for the in-water saturation reading. The salinity is zero in both full saturation methods.

Measurements of Optodes at Zero Saturation

The second endpoint for the two-point calibration is an assessment of the optode at zero dissolved oxygen. Borrowing from a procedure outlined in an Aanderaa product manual (Aanderaa, 2015), a solution of with sodium sulfite was created, using 20-30 g of sodium sulfite (Na_2SO_3) and 700-800 mL of water in a 2000 mL glass beaker. The chemical reaction that strips the solution of dissolved oxygen is



where the sulfur is oxidized from 4+ to 6+ and the oxygen gas is reduced. The reaction is performed at room temperature, and a stable temperature is necessary to prevent fluxes of dissolved oxygen due to changing temperature. In practice, the water is left at room temperature for a few hours to equilibrate its temperature. The sensor is left in the sodium sulfite solution for at least an hour before taking a reading at zero, which we hypothesize gives enough time for any oxygen gas introduced by the process of submerging the sensor to be stripped from the solution. The average dissolved oxygen concentration taken every 10 seconds for a 5-minute period is used as a zero-endpoint measurement. Following being submerged in the sodium sulfite solution, the optode is rinsed in fresh water before being allowed to dry and being put back in storage.

The temperature, atmospheric pressure, and relative humidity are also recorded for the zero-oxygen endpoint, but only the concentration of dissolved oxygen is needed to calculate the gain and offset coefficients. As the zero-oxygen method is in water, the relative humidity is set to 1.

Gain and Offset Calculation

Simple algebra transforms the measurements of oxygen saturation and oxygen concentration at the full saturation endpoint and oxygen concentration at the zero-oxygen endpoint into the gain and offset coefficients. The measured value at zero, $[\text{O}_2]_z$, the measured value at full saturation, $[\text{O}_2]_f$, and the theoretical full saturation value are used, $[\text{O}_2^*(T,S,P)]$:

$$G = \frac{[\text{O}_2^*(T, S, P)]}{[\text{O}_2]_f - [\text{O}_2]_z}, \quad (17)$$

$$Z = -G * [\text{O}_2]_z. \quad (18)$$

The offset is negative because it compensates for any readings of positive dissolved oxygen concentration in the zero-oxygen environment.

The gain and offset laboratory coefficients were calculated beginning in November 2018, after some sensors had already been deployed since December 2016. For many sensors, the first measurement of the gain and offset coefficients are one or two years after calibration.

Comparison of laboratory measurements to correction via opportunistic hydrographic measurements

CalCOFI bottle samples of dissolved oxygen where the oxygen concentration was determined by Winkler titration are used to obtain a gain correction for sensors on selected glider deployments. The glider transects in CUGN run along CalCOFI hydrographic lines, Lines 66.7, 80.0, and 90.0. Lines 80.0 and 90.0 are sampled quarterly by CalCOFI ships. Dissolved oxygen from Winkler titrations of bottle samples from CalCOFI are compared to the nearest glider dive in time, horizontal distance, and isopycnal surface. Using isopycnals as the z-coordinate minimizes the effect of heave. The comparison is limited to oxygen concentration above 1 ml l^{-1} . The precision of Winkler measurements is $0.005\text{-}0.010 \text{ ml l}^{-1}$ (Culbertson et al., 1991; Langdon, 2010), so comparison of dissolved oxygen values close to zero is ineffective. Due to the oxygen minimum zone in the CCS, often values between 340-500 m deep are excluded. A weighted-least-squares fit between the CalCOFI cast and the glider profile is performed to determine a gain. Only a gain correction is applied since the fit emphasizes surface values and ignores values near zero oxygen concentration. The fit is weighted by $1/V$ where V is the variance of dissolved oxygen from nearby glider dives to account for horizontal variability of dissolved oxygen in the environment. For each glider dive and CalCOFI cast pair, half of the horizontal distance between the glider dive and CalCOFI cast is the radius within which glider dives are used to compute the variance in dissolved oxygen. The distance between adjacent CalCOFI stations is up to 74 km, which sets the maximum distance between the comparison dive and cast at 37 km.

Hydrographic comparison of casts and glider dives are attempted for glider deployments between December 2016 and December 2019. In the case where there is no cast within 37 km of a dive, or when

the comparison is in shallow, nearshore waters or in a region of extremely high horizontal variability, the gain is not reported. Effectively, gain values of 1.1 or higher are discarded as unreliable estimates.

Results

Gain values over time

The evolution of the gain coefficient shows a non-linear increase over time that is consistent among almost all the 14 SBE63 oxygen sensors. The gain coefficient as computed from the in-water saturation technique shows the clearest pattern of change over time (Fig. 4.1). Eleven out of the fourteen sensors appear to evolve similarly. At 2000 days or roughly five and a half years after calibration at Sea-Bird or factory calibration, five sensors have a gain of roughly 1.07. Six additional sensors lie on the curve from 0-2000 days. For the majority of sensors, in the first 1000 days the gain increases from 1 to 1.05, while in the second 1000 days, the gain increases from 1.05 to 1.07, demonstrating the non-linearity of the drift over time. Sensors 632494 and 632495 are outliers with greater gain values than expected while sensor 630754 has a noticeably lower gain over time compared to the others. The gain is more precisely measured using the in-water method than the in-air method (Fig. 4.2), which can be seen in the comparison of gain over time plots.

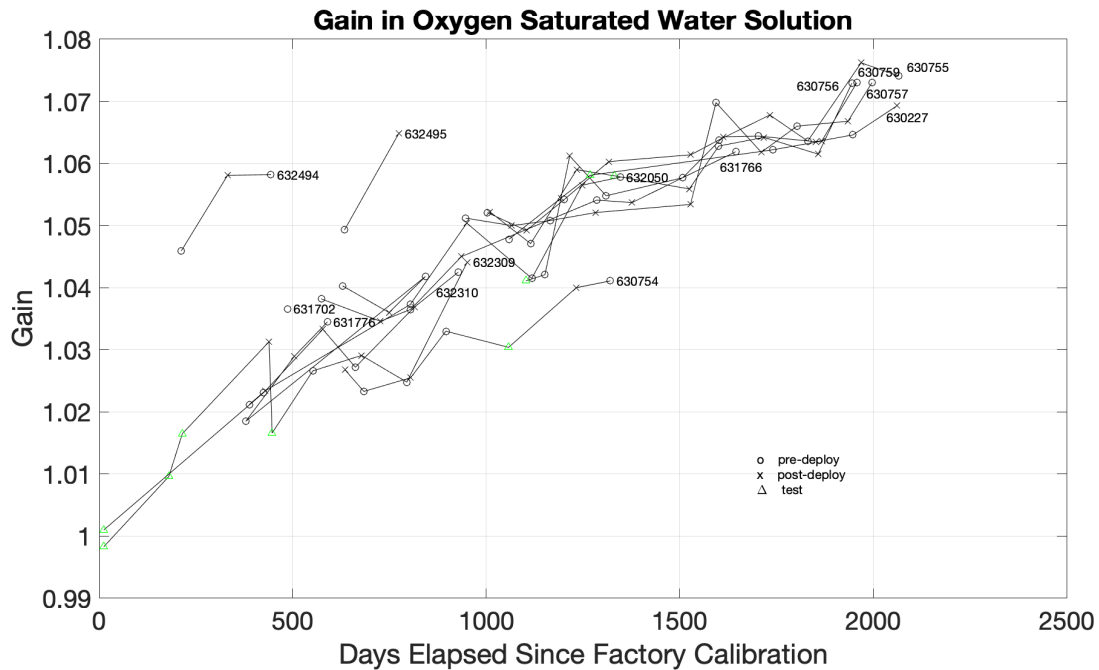


Figure 4.1 Gain over time using the in-water method. The x-axis is the number of days since the calibration at Sea-Bird, which calculates the full set of model coefficients for a range of temperature and oxygen concentrations. Gain values greater than one indicate that the SBE63 reads a lower concentration than present in the environment. The individual sensor gain values are plotted and labeled with the sensor serial number. Each gain value is marked by whether it was taken before a glider deployment, “pre-deploy” (o), after a glider deployment, “post-deploy” (x), or at any other time, “test” (Δ).

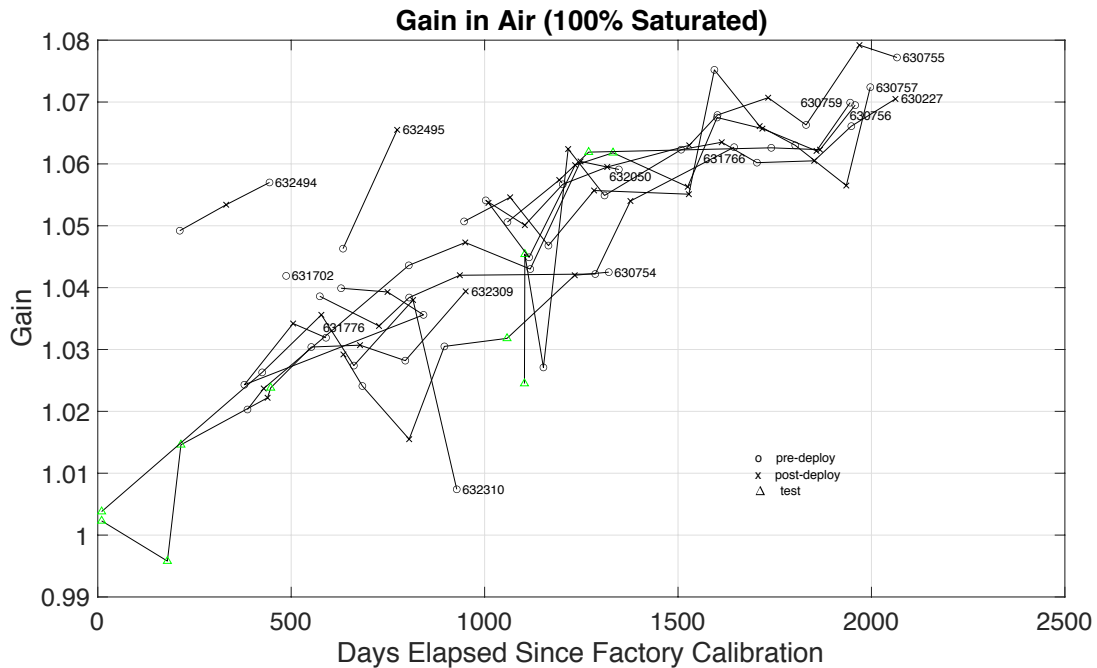


Figure 4.2 Gain over time using the in-air method. The x-axis is the number of days since the calibration at Sea-Bird, which calculates the full set of model coefficients for a range of temperature and oxygen concentrations. Gain values greater than one indicate that the SBE63 reads a lower concentration than present in the environment. The individual sensor gain values are plotted and labeled with the sensor serial number. Each gain value is marked by whether it was taken before a glider deployment, “pre-deploy” (o), after a glider deployment, “post-deploy” (x), or at any other time, “test” (Δ).

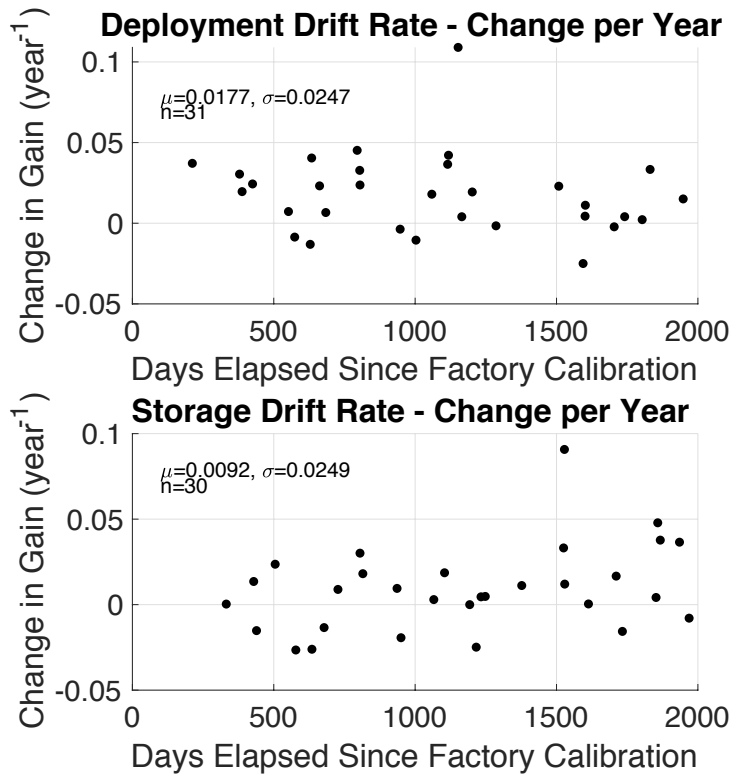


Figure 4.3 Rates of change of the gain coefficient during storage and deployment (year^{-1}) from the in-water full saturation method. The x-coordinate of each data point is the days elapsed since calibration of the first of the pair of measurements used to calculate the rate of change. Mean values, μ , standard deviations, σ , and the number of data points, n , are displayed on the plots.

The rate of change during deployment and after deployment is found to be comparable. Rates of change of the gain calculated from the in-water method during deployment or during dry storage have mean values of 0.0177 ± 0.0044 and 0.0092 ± 0.0046 per year respectively (Fig. 4.3). While the mean value of the rate of change during deployment is higher than that during storage, the errors (standard error of the mean) are high compared to the mean values and cast doubt on the significance of the difference between the two rates. For this reason, we report that the gain over time evolves similarly whether over deployment or during dry storage. There is some deviation in the rate of change from 1500-2000 days compared to from 0-1500 days, but because the standard deviation of the storage and deployment drifts is over 0.02 year^{-1} , trends in the measurements of storage drift and deployment drift over time are not reported. Error in the full saturation reading can be amplified when calculating the change in gain over

short time periods such as 60 days. The better representation of the drift over time is the assessment of 93 calculations of gain from the in-water full saturation method presented in Fig. 4.1.

Offset values over time

The measurements in zero-oxygen (Fig. 4.4) were found to be consistently small over time. Sensors 630757, 630227, 630755, 630756, 630759, 632050, and 632309 appear not to read increasingly higher dissolved oxygen over time with values consistently around 0.05-0.06 ml l⁻¹. Six of the remaining sensors appear to have slightly increasing measurements at zero, increasing in value by 0.01-0.03 ml l⁻¹. Bittig and Körtzinger (2015) found increasing values at zero over time of 2 µmol kg⁻¹ or 0.04 ml l⁻¹ over 3 years. Because two different behaviors of the sensors at zero are observed and because the values of the oxygen concentration are small, it is possible that small differences in the experimental setup caused some of the differences in the measurements. Alternatively, certain batches of sensors may behave differently over time. All values at zero, [O₂]_z, were 0.1 ml l⁻¹ or less, so long-term changes in the values of the 2-point corrections over time for most of the SBE63s in this study are due to steady changes in the gain, rather than changes in the concentration measured at zero oxygen. The standard deviation, σ , of the measurements at zero is 0.011 ml l⁻¹ or 0.49 µmol kg⁻¹ and contributes to the error in the offset parameter. The mean offset is -0.064 and the standard deviation of the offset is 0.011 ml l⁻¹, which we take as the error in the offset procedure. The uncertainty of 0.011 ml l⁻¹ or 0.49 µmol kg⁻¹ in freshwater is 0.2% of full saturation at 10 °C, salinity of 32, and 1 atm.

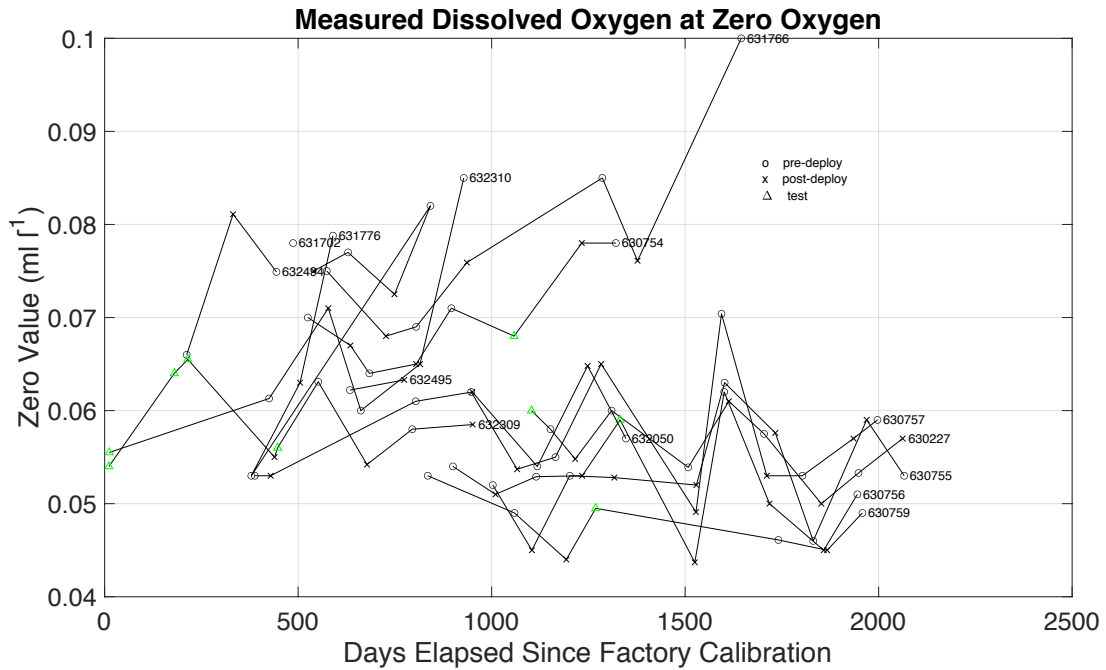


Figure 4.4 Measured dissolved oxygen concentration in the zero-oxygen environment. The x-axis is the number of days since the calibration at Sea-Bird, which calculates the full set of model coefficients for a range of temperature and oxygen concentrations. The individual measurements are plotted and labeled with the sensor serial number. Each measurement is marked by whether it was taken before a glider deployment, “pre-deploy” (o), after a glider deployment, “post-deploy” (x), or any other time, “test” (Δ).

Gain from hydrographic comparisons

For applications of optode sensors without laboratory calibrations, comparison with hydrographic profiles is often used to correct the dissolved oxygen data. Gain derived from comparison of CalCOFI casts and glider dives has high variability and is often larger than that derived from laboratory measurement (Fig. 4.5). In addition, the change in drift over time does not show a clear trend.

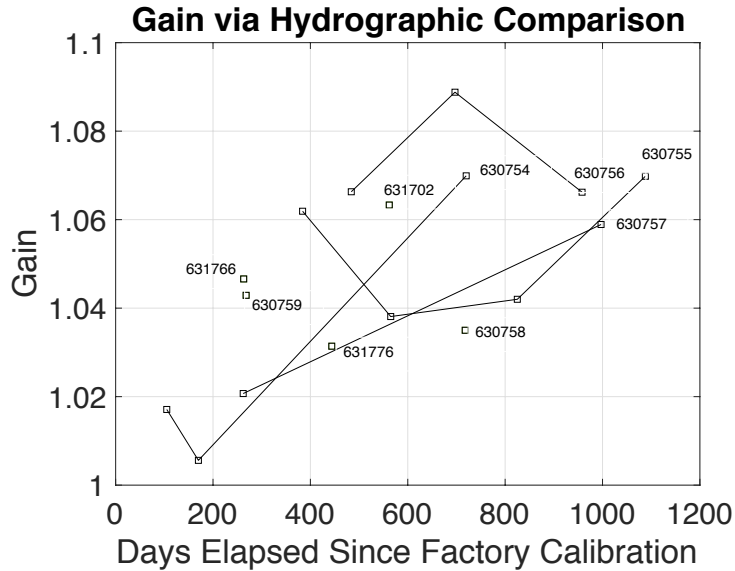


Figure 4.5 Gain over time from comparison with CalCOFI dissolved oxygen samples. The individual sensor gain values are plotted and labeled with the sensor serial number. The x-axis is the number of days since the calibration at Sea-Bird, which calculates the full set of model coefficients for a range of temperature and oxygen concentrations.

Characterizing the drift over time

A quadratic equation is fit to the gain evolution over time derived from the in-water full saturation method, and coefficients are found relating x , the days since calibration, and y , the gain value minus 1. The outliers of sensors 632494 and 632495 are not included in the fit. The residuals of the fit have a root mean square error of 0.0056, which is a measure of the error of the in-water saturation procedure and is taken as the error in the gain coefficient. The error of 0.6% of the gain coefficient is small enough to be able to describe variations of oxygen saturation states in the upper ocean of 5-10%. The 0.6% error applies the most to oxygen concentrations of 2 ml l^{-1} or greater when the gain error is larger than the offset error of 0.011 ml l^{-1} .

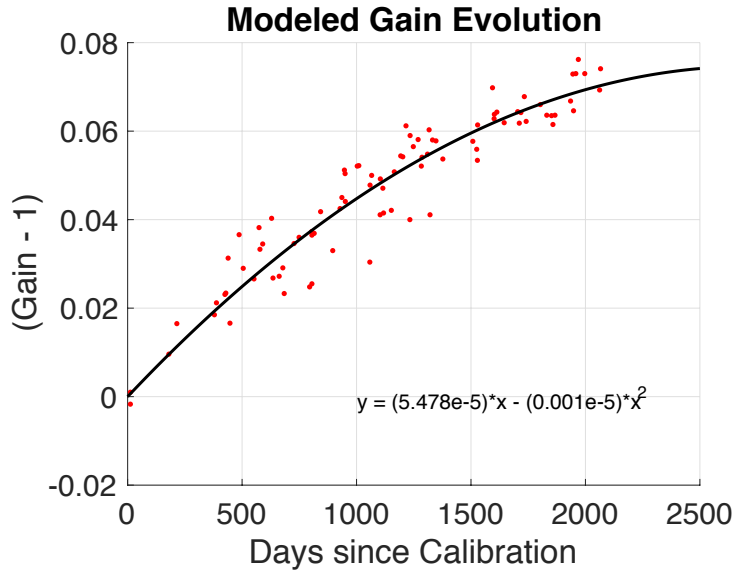


Figure 4.6 Modeled gain evolution with time. The model (black line) is a quadratic equation in x , the days since calibration and determines y , the gain minus 1. The data contributing to the model are plotted in red dots and come from twelve SBE63 sensors (632494 and 632495 are excluded).

Discussion

The stated goals are to characterize the drift of SBE63s over 5 years, whether stored in air or deployed in the ocean, and to suggest procedures to periodically correct for dissolved oxygen sensor drift, and the results suggest that for the SBE63s on gliders, there is a mathematical model that can predict drift over time and the best correction procedure includes an in-water full saturation measurement. The mathematical model describing the drift is a quadratic equation that relates the number of days since sensor calibration with the gain coefficient. Previous studies also found the drift evolution to be non-linear (Bittig, Körtzinger, Neill, et al., 2018), though they fit the data using an exponential with a time constant of around 2 years. In the results here, after 2 years since calibration, the gain is still found to increase at a significant rate.

With regards to the procedure, the in-air full saturation method is found to be inferior to the in-water full saturation method, and the opportunistic comparison with hydrographic casts is found to be the least effective method. The reasons for the in-air method to be unreliable are likely related to sensor design. The Aanderaa user manual and Sea-Bird recommendations (personal communication) suggest

that the sensor membrane and luminophore are in a different state when completely dry and can have inaccurate dissolved oxygen readings. The sensor takes hours to become completely wet or dry, and spot measurements of a dry sensor in a wet environment have errors of 2% (Aanderaa, 2015). Full humidity is not equivalent to a wet environment; keeping a sensor humid for 12 hours is equivalent to having a wet sensor (Aanderaa, 2015). The chemistry of the sensor membrane which holds the luminophore causes the differences. A procedure that could produce a reliable in-air measurement may be to submerge a sensor in freshwater for 3 or more hours and then perform a measurement in air, noting the relative humidity and using equation 13. This procedure eliminates the need to set up an aquarium pump and aquarium stone, but aquarium pumps and aquarium stones are generally cheap, widely available, and easy to set up. One criticism of the pump method is that the introduction of bubbles can cause an environment oversaturated with dissolved oxygen. Performing the reading in air after the sensor is wet could eliminate the possibility of oversaturation. The in-water procedure here has a low probability of oversaturation because the bubbles are created inches from the surface within the glass beaker. Further the SBE63 membrane is protected from interacting with bubbles directly as it is designed for a pumped system and is enclosed other than for its inflow and outflow holes.

The comparison with hydrographic casts produces the worst gain estimates due to the natural variability in the ocean on small scales and practical issues with matching casts with dives. In many instances, casts and dives are not found close enough in distance or time. When there is a matching dive and cast, often the horizontal variability in dissolved oxygen plays a part in an imprecise and inaccurate gain estimate. In the CCS, there is an oxygen minimum zone, which also impacts the accuracy of gain estimates using hydrography. The precision of Winkler titrations causes titrations near zero concentration to be less accurate. The least-squares comparison relies on observations in higher dissolved oxygen concentrations which have more variability. This problem is avoided if the casts are performed in a region without an oxygen minimum zone or if the observations extend to deeper depths. Performing corrections using laboratory procedures before deployment also allows for real-time corrected glider

dissolved oxygen data. The combination of factors means that for the CUGN gliders, laboratory corrections are better than the gain estimated from comparison with hydrography.

The measurements of the SBE63 at zero oxygen are of the same magnitude as in Bittig, Körtzinger, Neill, et al. (2018), which lends support to their accuracy. However, we are not able to confidently describe trends over time in the concentration of dissolved oxygen measured at zero, while Bittig, Körtzinger, Neill, et al. (2018) suggest a small increase over time. The data appear to have two clusters, with one set not showing any change over time and the other set showing slight increases. The coefficients of the Sea-Bird model are fit for a range of oxygen concentrations starting at near 1 ml l^{-1} , so it may be that the sensor model is not well fit to concentrations at or near zero concentration. Overall, the result from the zero-measurements is that we consistently measured a small non-zero concentration of dissolved oxygen on the SBE63s around 0.07 ml/l or $3 \text{ } \mu\text{mol kg}^{-1}$. It is worth noting that the initial accuracy of SBE63 sensors is $\pm 3 \text{ } \mu\text{mol kg}^{-1}$ or $\pm 2\%$, whichever is larger depending on the oxygen concentration value (Sea-Bird, 2017).

The drift during storage and the drift during deployment were comparable in this study of 14 SBE63s that spent time on the schedule of 100 days at sea, 100 days on land. We hypothesize that drift that occurs during storage is related to prolonged storage of optodes in dry conditions and that 100 days is not a long enough period for an accelerated rate of drift to occur. Most SBE63 sensors are stored installed on a Spray glider, which means that the optode sensor is connected to the flow-through tubing that when deployed, runs pumped water through the installed sensors including the CTD and fluorometer. The tubing may provide a more humid environment than the air in the laboratory. There are instances where the SBE63 would get wet, because the Spray glider may be submerged in a bath to test other sensors or aspects of the glider. If an SBE63 sensor installed on a glider that is part of the routine 100-day deployment schedule, it will get wet during its storage especially since the correction of the SBE63 is performed in water. There are sensors that are kept as spare in the laboratory, and these sensors are stored

alone or on spare gliders. Spending 12 months or more in a dry environment may be related to the increased gain coefficient at shorter times since calibration found on 632495.

Conclusions

Through tracking 14 SBE63 dissolved oxygen optode sensors used on Spray gliders in the CCS, the drift over 5 years since calibration is quantified. The drift can be predicted well with a quadratic model. The storage and deployment drift are found to be comparable, suggesting that 3-4 months of dry storage does not induce large changes in sensor accuracy. The suggested procedure for 2-point calibrations of the optode sensors is an in-water calibration at full saturation and a measurement at zero-oxygen using a sodium sulfite solution. Gain coefficients after 5 years approached 8%, highlighting the need for periodic corrections. The error of the oxygen data after correction is the larger of 0.6% or $0.5 \mu\text{mol kg}^{-1}$ (0.011 ml l), depending on oxygen concentration. As global ocean deoxygenation is of concern as an impact of climate change, calibrated dissolved oxygen optode sensors are of utmost importance to observing changes in the oceans with accuracy.

Chapter 4, in full, is being prepared for submission of the material as it currently appears in: Ren, A.S., and Rudnick, D.L. (2022) Drift characteristics of Sea-Bird dissolved oxygen optode sensors. *Journal of Atmospheric and Oceanic Technology*. The dissertation author was the primary investigator and author of this paper.

References

- Aanderaa. (2015). *TD 269 Operating Manual Oxygen Optode 4330, 4831, 4835*.
- Alkire, M. B., Lee, C., D'Asaro, E., Perry, M. J., Briggs, N., Cetinić, I., & Gray, A. (2014). Net community production and export from Seaglider measurements in the North Atlantic after the spring bloom. *Journal of Geophysical Research: Oceans*, *119*(9), 6121-6139. <https://doi.org/https://doi.org/10.1002/2014JC010105>
- Benson, B. B., & Krause Jr., D. (1984). The concentration and isotopic fractionation of oxygen dissolved in freshwater and seawater in equilibrium with the atmosphere1. *Limnology and Oceanography*, *29*(3), 620-632. <https://doi.org/https://doi.org/10.4319/lo.1984.29.3.0620>
- Bittig, H. C., & Körtzinger, A. (2015). Tackling Oxygen Optode Drift: Near-Surface and In-Air Oxygen Optode Measurements on a Float Provide an Accurate in Situ Reference. *Journal of Atmospheric and Oceanic Technology*, *32*(8), 1536-1543. <https://doi.org/10.1175/jtech-d-14-00162.1>
- Bittig, H. C., Körtzinger, A., Johnson, K., Claustre, H., Emerson, S., Fennel, K., Garcia, H., Gilbert, D., Gruber, N., Kang, D.-J., Naqvi, W., Prakash, S., Riser, S., Thierry, V., Tilbrook, B., Uchida, H., Ulloa, O., & Xing, X. (2018). *SCOR WG 142: Quality Control Procedures for Oxygen and Other Biogeochemical Sensors on Floats and Gliders. Recommendations on the conversion between oxygen quantities for Bio-Argo floats and other autonomous sensor platforms*. <https://doi.org/10.13155/45915>
- Bittig, H. C., Körtzinger, A., Neill, C., van Ooijen, E., Plant, J. N., Hahn, J., Johnson, K. S., Yang, B., & Emerson, S. R. (2018). Oxygen Optode Sensors: Principle, Characterization, Calibration, and Application in the Ocean [Original Research]. *Frontiers in Marine Science*, *4*(429). <https://doi.org/10.3389/fmars.2017.00429>
- Bushinsky, S. M., Emerson, S. R., Riser, S. C., & Swift, D. D. (2016). Accurate oxygen measurements on modified Argo floats using in situ air calibrations. *Limnology and Oceanography: Methods*, *14*(8), 491-505. <https://doi.org/10.1002/lom3.10107>
- Culberson, C. H., Knapp, G. P., Stalcup, M. C., Williams, R. T., & Zemlyak, F. (1991). A comparison of methods for the determination of dissolved oxygen in seawater. *WOCE Report 73/91, WHPO Publication*, *91*(2).
- Damerell, G. M., Heywood, K. J., Thompson, A. F., Binetti, U., & Kaiser, J. (2016). The vertical structure of upper ocean variability at the Porcupine Abyssal Plain during 2012–2013. *Journal of Geophysical Research: Oceans*, *121*(5), 3075-3089. <https://doi.org/https://doi.org/10.1002/2015JC011423>
- Demas, J., DeGraff, B., & Coleman, P. (1999). Oxygen sensors based on luminescence quenching. *Analytical chemistry*, *71*(23), 793A-800A.
- Garcia, H. E., & Gordon, L. I. (1992). Oxygen solubility in seawater: Better fitting equations. *Limnology and Oceanography*, *37*(6), 1307-1312. <https://doi.org/https://doi.org/10.4319/lo.1992.37.6.1307>
- Haskell II, W. Z., Hammond, D. E., Prokopenko, M. G., Teel, E. N., Seegers, B. N., Ragan, M. A., Rollins, N., & Jones, B. H. (2019). Net Community Production in a Productive Coastal Ocean

- From an Autonomous Buoyancy-Driven Glider. *Journal of Geophysical Research: Oceans*, 124(6), 4188-4207. <https://doi.org/https://doi.org/10.1029/2019JC015048>
- Howatt, T., Palter, J. B., Robin Matthews, J. B., Brad deYoung, Bachmayer, R., & Claus, B. (2018). Ekman and Eddy Exchange of Freshwater and Oxygen across the Labrador Shelf Break. *Journal of Physical Oceanography*, 48(5), 1015-1031. <https://doi.org/10.1175/jpo-d-17-0148.1>
- Hull, T., Greenwood, N., Birchill, A., Beaton, A., Palmer, M., & Kaiser, J. (2021). Simultaneous assessment of oxygen- and nitrate-based net community production in a temperate shelf sea from a single ocean glider. *Biogeosciences*, 18(23), 6167-6180. <https://doi.org/10.5194/bg-18-6167-2021>
- Johnson, K. S., Plant, J. N., Riser, S. C., & Gilbert, D. (2015). Air Oxygen Calibration of Oxygen Optodes on a Profiling Float Array. *Journal of Atmospheric and Oceanic Technology*, 32(11), 2160-2172. <https://doi.org/10.1175/jtech-d-15-0101.1>
- Körtzinger, A., Schimanski, J., & Send, U. (2005). High Quality Oxygen Measurements from Profiling Floats: A Promising New Technique. *Journal of Atmospheric and Oceanic Technology*, 22(3), 302-308. <https://doi.org/10.1175/jtech1701.1>
- Langdon, C. (2010). Determination of Dissolved Oxygen in Seawater by Winkler Titration Using the Amperometric Technique. In E. M. Hood, C. L. Sabine, & B. M. Sloyan (Eds.), *The GO-SHIP Repeat Hydrography Manual: A Collection of Expert Reports and Guidelines*. IOCCP Report Number 14, ICPO Publication Series Number 134.
- Nicholson, D., Emerson, S., & Eriksen, C. C. (2008). Net community production in the deep euphotic zone of the subtropical North Pacific gyre from glider surveys. *Limnology and Oceanography*, 53(5part2), 2226-2236. https://doi.org/https://doi.org/10.4319/lo.2008.53.5_part_2.2226
- Nicholson, D. P., & Feen, M. L. (2017). Air calibration of an oxygen optode on an underwater glider. *Limnology and Oceanography: Methods*, 15(5), 495-502. <https://doi.org/https://doi.org/10.1002/lom3.10177>
- Nicholson, D. P., Wilson, S. T., Doney, S. C., & Karl, D. M. (2015). Quantifying subtropical North Pacific gyre mixed layer primary productivity from Seaglider observations of diel oxygen cycles. *Geophysical Research Letters*, 42(10), 4032-4039. <https://doi.org/https://doi.org/10.1002/2015GL063065>
- Pelland, N. A., Eriksen, C. C., Emerson, S. R., & Cronin, M. F. (2018). Seaglider Surveys at Ocean Station Papa: Oxygen Kinematics and Upper-Ocean Metabolism. *Journal of Geophysical Research: Oceans*, 123(9), 6408-6427. <https://doi.org/https://doi.org/10.1029/2018JC014091>
- Pietri, A., & Karstensen, J. (2018). Dynamical Characterization of a Low Oxygen Submesoscale Coherent Vortex in the Eastern North Atlantic Ocean. *Journal of Geophysical Research: Oceans*, 123(3), 2049-2065. <https://doi.org/10.1002/2017jc013177>
- Pizarro, O., Ramírez, N., Castillo, M. I., Cifuentes, U., Rojas, W., & Pizarro-Koch, M. (2016). Underwater Glider Observations in the Oxygen Minimum Zone off Central Chile. *Bulletin of the American Meteorological Society*, 97(10), 1783-1789. <https://doi.org/10.1175/bams-d-14-00040.1>

- Rudnick, D. L. (2016). Ocean Research Enabled by Underwater Gliders. *Annual Review of Marine Science*, 8(1), 519-541. <https://doi.org/10.1146/annurev-marine-122414-033913>
- Rudnick, D. L., Zaba, K. D., Todd, R. E., & Davis, R. E. (2017). A climatology of the California Current System from a network of underwater gliders. *Progress in Oceanography*, 154, 64-106. <https://doi.org/10.1016/j.pocean.2017.03.002>
- Schütte, F., Karstensen, J., Krahnemann, G., Hauss, H., Fiedler, B., Brandt, P., Visbeck, M., & Körtzinger, A. (2016). Characterization of “dead-zone” eddies in the eastern tropical North Atlantic. *Biogeosciences*, 13(20), 5865-5881. <https://doi.org/10.5194/bg-13-5865-2016>
- Sea-Bird. (2017). *User Manual: SBE 63 Optical Dissolved Oxygen Sensor*.
- Sherman, J., Davis, R. E., Owens, W. B., & Valdes, J. (2001). The autonomous underwater glider "Spray". *IEEE Journal of Oceanic Engineering*, 26(4), 437-446. <https://doi.org/10.1109/48.972076>
- Uchida, H., Kawano, T., Kaneko, I., & Fukasawa, M. (2008). In Situ Calibration of Optode-Based Oxygen Sensors. *Journal of Atmospheric and Oceanic Technology*, 25(12), 2271-2281. <https://doi.org/10.1175/2008JTECHO549.1>
- Weiss, R. F., & Price, B. A. (1980). Nitrous oxide solubility in water and seawater. *Marine Chemistry*, 8(4), 347-359. [https://doi.org/https://doi.org/10.1016/0304-4203\(80\)90024-9](https://doi.org/https://doi.org/10.1016/0304-4203(80)90024-9)

CONCLUSION

The CCS is investigated using a network of gliders collecting high-resolution observations that allow for the study of mesoscale to large-scale processes. The thesis describes 1) an interannual salinity anomaly in the CCS, 2) the across-shore propagation speed of subthermocline eddies, and 3) the annual cycle of dissolved oxygen in the upper 500 m in a coastal region with seasonal upwelling. In addition, characteristics of drift of Sea-Bird 63 optode dissolved oxygen sensors are described, based on sensor usage on gliders in CUGN.

The observational technique used in the four chapters of the thesis is the same. By measuring profiles once every 3 km and 3 hours and sustaining the observational program continuously for years, the CUGN spray glider observations capture the mean annual cycle of temperature and salinity along the Lines 66.7, 80.0, and 90.0. Having a good mean annual cycle then allows for the type of analysis in chapters 1 and 2 of salinity anomalies. The temperature and salinity anomalies are described in chapter 1 for the period 2007-2019, long enough to capture climate variability. In addition, mesoscale features that are persistent and slow-moving are captured in the temperature and salinity dataset of 2007-2019, and chapter 2 takes advantage of multi-year salinity anomaly observations to describe the movement across-shore of salinity anomalies. CUGN observations can describe movement of mesoscale anomalies or the presence of interannual anomalies via hovmoller diagrams down to 500 m. The subsurface description of mesoscale and large-scale phenomena over hundreds of kilometers in the coastal 500 km of ocean is a novel contribution.

The successful measurement of temperature and salinity leads to programs to measure additional oceanic variables on the Spray gliders. Dissolved oxygen is demonstrated to be a variable where long-term observation of the mean is possible. The first hurdle is measurement without sensor drift, which is described in chapter 4. The next step is characterization of the mean annual cycle of dissolved oxygen, which is accomplished in chapter 3. In the future, the mean annual cycle could be described with more than 4 years of observations, and anomalies in dissolved oxygen from the mean annual cycle may be analyzed. There are many scientific questions related to the interannual variability of dissolved oxygen

including long-term trends of deoxygenation and year-to-year changes in net community production. The important work of having a procedure to make consistent observations on climate time scales and understanding the mean behavior of dissolved oxygen are presented in the thesis, with the understanding that because the first two steps have been completed, future work will be able to look at oxygen anomalies.

In the thesis, some terms are measured observationally, and the importance of other terms is evaluated based on results from the observations. In chapter 1, the advection of salt, su , across a line of longitude changes over time. Thus, changing surface buoyancy (evaporation and precipitation), changes in the position of the mean currents, or changing vertical mixing (entrainment) are important to the model of the ocean in chapter 1. In chapter 2, the eddy terms of the equations are found to be important. In chapter 3, the annual cycle in the offshore region is modeled, and low vertical mixing between the upper and lower ocean layers leads to the formation of a summer subsurface dissolved oxygen maximum. The buoyancy forcing at the surface and vertical mixing are crucial to reproduce the features of the CUGN observations. Vertical advection (heave of isopycnals) and vertical mixing are both observed during seasonal upwelling at the coast. Finally, chapter 1 describes interannual variability which may be a result of natural climate variability. The salinity anomaly of 2017-2019 is not related to El-Nino or the NPGO, and future work may determine if the high salinity is part of a long-term trend, a climate oscillation, or a chance occurrence.

Future work based on the PhD may include a better understanding subthermocline eddies and work on dissolved oxygen anomalies in the CCS. Work with theory and numerical modeling may be able to determine why subthermocline eddies are observed to propagate offshore at around the 1st baroclinic Rossby wave speed. With respect to dissolved oxygen anomalies, global climate models have a difficult time predicting the sign of dissolved oxygen changes in the future, so observation of dissolved oxygen anomalies may help to determine the correct balance of terms needed in an accurate numerical model. The CUGN observations could be used for parameter estimation of key coefficients that govern the rates

of oxygen source and sink processes, and mixing. For example, assimilative numerical models may be able to extract information available in the CUGN dissolved oxygen observations.

The Spray glider observations can describe ocean processes from the mesoscale to the large-scale and are a valuable tool for understanding ocean subsurface variability and dynamics. The thesis demonstrates that observations can study the anomalies in salinity and the mean cycle in dissolved oxygen. Many scientific questions remain open and may be tackled with CUGN or coordinated Spray glider operations in the future.